AGU100 ADVANCING EARTH AND SPACE SCIENCE

Journal of Advances in Modeling Earth Systems

RESEARCH ARTICLE
10.1029/2018MS001372

Improved Simulations of Tropical Pacific Annual-Mean Climate in the GFDL FLOR and HiFLOR Coupled GCMs

Andrew T. Wittenberg[1], Gabriel A. Vecchi[2,3,4], Thomas L. Delworth[1], Anthony Rosati[1], Whit G. Anderson[1], William F. Cooke[5], Seth Underwood[1], Fanrong Zeng[1], Stephen M. Griffies[1], and Sulagna Ray[4]

[1]NOAA Geophysical Fluid Dynamics Laboratory, Princeton, NJ, USA, [2]Department of Geosciences, Princeton University, Princeton, NJ, USA, [3]Princeton Environmental Institute, Princeton University, Princeton, NJ, USA, [4]Program in Atmospheric and Oceanic Sciences, Princeton University, Princeton, NJ, USA, [5]Cooperative Programs for the Advancement of Earth System Science, University Corporation for Atmospheric Research, Boulder, CO, USA

Key Points:
- New global models show greatly improved tropical Pacific annual-mean climate
- Both physics improvements and refined atmospheric grids aid the new models
- Off-equatorial surface fluxes strongly affect the equatorial Pacific climatology

Correspondence to:
A. T. Wittenberg,
andrew.wittenberg@noaa.gov

Citation:
Wittenberg, A. T., Vecchi, G., Delworth, T. L., Rosati, A., Anderson, W. G., Cooke, W. F., et al. (2018). Improved simulations of tropical Pacific annual-mean climate in the GFDL FLOR and HiFLOR coupled GCMs. *Journal of Advances in Modeling Earth Systems*, *10*, 3176–3220. https://doi.org/10.1029/2018MS001372

Received 10 MAY 2018
Accepted 5 NOV 2018
Accepted article online 9 NOV 2018
Published online 25 DEC 2018

Abstract The National Oceanic and Atmospheric Administration's Geophysical Fluid Dynamics Laboratory has recently developed two global coupled general circulation models, the Forecast-oriented Low Ocean Resolution (FLOR) model and the High atmospheric resolution Forecast-oriented Low Ocean Resolution (HiFLOR) model, which are now being utilized for climate research and seasonal predictions. Compared to their predecessor Coupled Model version 2.1 (CM2.1), the new versions have improved ocean/atmosphere physics and numerics and refinement of the atmospheric horizontal grid from 220 km (CM2.1) to 55 km (FLOR) and 26 km (HiFLOR). Both FLOR and HiFLOR demonstrate greatly improved simulations of the tropical Pacific annual-mean climatology, with FLOR practically eliminating any equatorial cold bias in sea surface temperature. An additional model experiment (Low Ocean Atmosphere Resolution version 1) using FLOR's ocean/atmosphere physics, but with the atmospheric grid coarsened toward that of CM2.1, is used to further isolate the impacts of the refined atmospheric grid versus the improved physics and numerics. The improved ocean/atmosphere formulations are found to produce more realistic tropical Pacific patterns of sea surface temperature and rainfall, surface heat fluxes, ocean mixed layer depths, surface currents, and tropical instability wave activity; enhance the near-surface equatorial upwelling; and reduce the intercentennial warm drift of the tropical Pacific upper ocean. The atmospheric grid refinement further improves these features and also improves the tropical Pacific surface wind stress, implied Ekman and Sverdrup transports, subsurface temperature and salinity structure, and heat advection in the equatorial upper ocean. The results highlight the importance of nonlocal air-sea interactions in the tropical Pacific climate system, including the influence of off-equatorial surface fluxes on the equatorial annual-mean state. Implications are discussed for improving future simulations, observations, and predictions of tropical Pacific climate.

1. Introduction

Tropical Pacific ocean-atmosphere interactions drive much of the intraseasonal-to-decadal variability of Earth's climate. For example, the El Niño/Southern Oscillation (ENSO) has enormous impacts on ecosystems and economies worldwide (Cai et al., 2015; Christensen et al., 2014; Collins et al., 2010; Vecchi & Wittenberg, 2010). This variability is in turn sensitive to the tropical Pacific background climate, as well as changes in the climate arising from external radiative forcings and/or physical biases in coupled general circulation models (CGCMs; Capotondi, Ham, et al., 2015; Capotondi, Wittenberg, et al., 2015; Choi et al., 2015; DiNezio et al., 2012; Graham et al., 2017; Guilyardi et al., 2016; Tian, 2015; Wittenberg, 2002). It is therefore essential for global CGCMs to accurately simulate the climatology of the tropical Pacific, to lend confidence in their ability to predict and project future climate risks.

In recent years, improved observational constraints have emerged due to enhanced instrumentation, denser sampling, longer historical and proxy records, and more sophisticated reconstruction methods (McGregor et al., 2013; McPhaden et al., 2015; Sun et al., 2007). Simulations of tropical Pacific climate have also improved, as advances in numerical models and computer power have enabled more of the relevant physical processes

to be explicitly resolved or more accurately parameterized (Bellenger et al., 2014; Capotondi, Ham, et al., 2015; Capotondi, Wittenberg, et al., 2015; Guilyardi et al., 2009, 2012; Wittenberg, 2015).

Yet CGCMs still struggle to simulate key aspects of tropical Pacific climate. With today's computers, global models cannot yet resolve important small-scale processes — in particular convection and clouds in the atmosphere and mixing and stirring in the ocean. Imperfect parameterizations of those processes give rise to errors, which are then amplified and redistributed by atmosphere-ocean feedbacks — causing the simulated tropical climatology to depart from observations (Li & Xie, 2014; Li et al., 2015; Richter, 2015; Richter et al., 2012; Wang et al., 2014, Wittenberg et al., 2006).

Longstanding tropical Pacific climatological time-mean biases that are widespread among today's CGCMs include (1) an overly strong equatorial Pacific cold tongue that extends too far west; (2) warm sea surface temperature (SST) biases along the coast of South America; (3) biases in the intensities and positions of large-scale atmospheric convergence zones, including an overly zonal South Pacific Convergence Zone (SPCZ) and an overly strong Intertropical Convergence Zone (ITCZ) in the southeast tropical Pacific (i.e., a "seasonally-alternating" or "double" ITCZ); (4) biases in the strength and spatial pattern of the easterly trade winds, including their peak longitude along the equator and their pattern of wind stress curl near the equator; (5) biases refers to the pattern cloud cover, cloud types, and cloud optical thickness, especially for high clouds in the atmospheric convergence zones and low clouds near the South American coast; (6) deficiencies in the depth, intensity, sharpness, and zonal slope of the equatorial thermocline and the equatorial undercurrent (EUC); and (7) insufficient subseasonal stirring of the near-equatorial ocean associated with weak simulated tropical instability waves (TIWs).

This paper describes progress toward understanding and addressing these climatological biases, using recent model experiments conducted at the National Oceanic and Atmospheric Administration's Geophysical Fluid Dynamics Laboratory (GFDL). Beginning with the widely used GFDL Coupled Model version 2.1 (CM2.1) global coupled GCM, we first examine the impacts of improved physical and numerical formulations of the atmospheric and oceanic components, followed by refinement of the atmosphere's horizontal grid by a factor of four (in the Forecast-oriented Low Ocean Resolution [FLOR] model) or eight (in the High Forecast-oriented Low Ocean Resolution [HiFLOR] model). The results demonstrate remarkable improvements in the simulations, reveal complex nonlocal interdependencies among the model biases, and illuminate a number of paths toward improving future models.

2. Observational and Model Data Sets

Tables 1 – 3 list the observational products, model simulations, and external forcings used in this study, along with their abbreviations as used in this paper. Monthly mean data serve as the basis for all analyses, except where otherwise noted. Appendix A describes the model initializations and forcings used, and Appendix B describes the generation of the comparison figures and evaluation metrics.

2.1. CM2.1 Model

The GFDL CM2.1 is a CGCM with global atmospheric, oceanic, land, and sea ice components (Delworth et al., 2006), whose simulations of tropical Pacific climate and ENSO are described in Wittenberg et al. (2006). Simulations and projections from CM2.1 have been widely used by the research community, including via the Coupled Model Intercomparison Project phases 3 and 5 and research summarized in the Intergovernmental Panel on Climate Change Fourth and Fifth Assessment Reports. CM2.1 has been used for global coupled ocean-atmosphere data assimilation (Sun et al., 2007; Zhang et al., 2005, 2007), seasonal-to-interannual simulations and predictability studies (Chen et al., 2011; Choi et al., 2013; Karamperidou et al., 2014; Kug et al., 2010; Richter et al., 2012; Wittenberg et al., 2006; Wittenberg, 2009; Wittenberg et al., 2014; Yang et al., 2013), and decadal-to-centennial simulations, projections, and paleo studies (Emile-Geay et al., 2013a, 2013b; Erb et al., 2015; McGregor et al., 2013; Msadek et al., 2014; Ogata et al., 2013; Stenchikov et al., 2009; Vecchi et al., 2006, 2013; Xie et al., 2010). CM2.1 is also used for real-time global seasonal predictions, including monthly forecasts contributed to the International Research Institute, the Asia-Pacific Economic Cooperation Climate Center, and the North American MultiModel Ensemble (NMME; Kirtman et al., 2014).

The formulation of CM2.1 as outlined in Sec. 2a of Wittenberg et al. (2006) is repeated here for the convenience of the reader. CM2.1's atmosphere component is the Atmosphere Model version 2.1 (AM2.1) model (Delworth et al., 2006; Global Atmospheric Model Development Team GFDL, 2004), which consists of a finite-volume

Table 1
Observational Data Sets Used in this Study

Abbreviation	Data set name References URL	Δx	Δy	Frequency	Epoch
CERES.Ed2.8	Clouds and the Earth's Radiant Energy System Energy Balanced And Filled Surface fluxes, version 2.8 Kato et al. (2013) http://ceres.larc.nasa.gov/cmip5_data.php	1°	1°	Monthly	2001–2015
DEEP-C.v3	Diagnosing Earth's Energy Pathways in the Climate system, version 3 C. Liu et al. (2017) http://researchdata.reading.ac.uk/111	0.7°	0.7°	Monthly	1985–2015
GPCP.v2.3	Global Precipitation Climatology Project, version 2.3 Adler et al. (2003, 2016) http://www.esrl.noaa.gov/psd/data/gridded/data.gpcp.html	2.5°	2.5°	Monthly	1979–2016
ISCCP-FD	International Satellite Cloud Climatology Project radiative Flux Data (interpolated to OAFlux.v3 grid) Y. Zhang et al. (2004) ftp://ftp.whoi.edu/pub/science/oaflux/data_v3/monthly	2.5°	2.5°	Monthly	1984–2009
OAFlux.v3	Objectively Analyzed air-sea Fluxes, version 3 Yu et al. (2008) ftp://ftp.whoi.edu/pub/science/oaflux/data_v3/monthly	1°	1°	Monthly	1984–2015
OISST.v2	NOAA Optimum Interpolation SST, version 2 Reynolds et al. (2002) http://iridl.ldeo.columbia.edu/SOURCES/.IGOSS/.nmc/.Reyn_SmithOIv2/.monthly	1°	1°	Monthly	1982–2016
OISST.hi.v2	NOAA Optimum Interpolation SST (AVHRR-only), version 2 Banzon et al. (2016) http://www.ncdc.noaa.gov/oisst	0.25°	0.25°	Daily	1982–2016
OSCAR	Ocean Surface Current Analyses Real-time Bonjean and Lagerloef (2002) https://doi.org/10.5067/OSCAR-03D01	0.33°	0.33°	Monthly	1993–2016
SeaFlux.v1	SeaFlux Turbulent Fluxes, version 1 Curry et al. (2004) http://seaflux.org/seaflux_data/SEAFLUXV1/MONTHLY_AVERAGES	1°	1°	Monthly	1998–2007
TAO	Tropical Atmosphere Ocean mooring Acoustic Doppler Current Profiler and mechanical current meter McPhaden et al. (1998) http://www.pmel.noaa.gov/tao/drupal/disdel	—	Equator	Daily	1980–2017

Note. Δx and Δy indicate the zonal and meridional grid spacing, respectively. SST = sea surface temperature.

dynamical core (Lin, 2004) with 2.5° longitude by 2° latitude grid spacing, 24 vertical levels, a *K*-profile planetary boundary layer scheme (Lock et al., 2000), relaxed Arakawa-Schubert convection (Moorthi & Suarez, 1992), and a local parameterization of the vertical momentum transport by cumulus convection. The atmospheric component uses a 3-hr time step for atmospheric radiation and a 30-min step for all other atmospheric physics.

CM2.1's ocean component is the Ocean Model version 3.1 (OM3.1) model (Gnanadesikan et al., 2006; Griffies et al., 2005), configured from Modular Ocean Model version 4.0d (MOM4p0d) source code. The ocean model is configured on a tripolar horizontal B-grid, nominally 1° × 1° with meridional spacing that narrows to 1/3° near the equator. The tripolar grid of the ocean and sea ice models is everywhere oriented along longitude/latitude

Table 2
Observation-Based Reanalysis Data Dets Used in this Study

Abbreviation	Data set name References URL	Δx	Δy	Frequency	Epoch
ECDA.v3.1	GFDL Ensemble Coupled Data Assimilation, version 3.1 Chang et al. (2013) http://www.gfdl.noaa.gov/ocean-data-assimilation-model-output	1°	0.33–1°	Monthly	1979–2017
ERA-I	ECMWF Interim Reanalysis Dee et al. (2011) http://apps.ecmwf.int/datasets/data/interim-full-moda	0.75°	0.75°	Monthly	1979–2014/2016
ORA-S4	Ocean ReAnalysis System 4 Balmaseda et al. (2013) ftp://ftp.icdc.zmaw.de/EASYInit/ORA-S4	1°	0.33–0.95°	Monthly	1979–2014
SODA.v3.4.1	Simple Ocean Data Assimilation, version 3.4.1 (regridded by averaging from 0.25° grid) Carton et al. (2000) and Carton, Chepurin and Chen (2018) http://dsrs.atmos.umd.edu/DATA/soda3.4.1/monthly_netcdf	1°	0.5–1°	Monthly	1980–2015
TropFlux.v1	TropFlux heat fluxes, version 1 Praveen Kumar et al. (2012) http://www.incois.gov.in/tropflux_datasets/data/monthly	1°	1°	Monthly	1979–2016

Note. These products assimilate climate observations into comprehensive physical models of the ocean and/or atmosphere. Δx and Δy indicate the zonal and meridional grid spacing, respectively.

lines, except north of 65°N where the grid is curvilinear; the three poles of the grid lie over Canada, Siberia, and the South Pole. The ocean model has 50 vertical levels, spaced 10 m apart over the top 220 m of the ocean. Subgridscale parameterizations include vertical mixing from a *K*-profile parameterization scheme (Large et al., 1994), lateral mixing along neutral directions (Gent & McWilliams, 1990; Griffies, 1998; Griffies et al., 1998), and a spatially dependent anisotropic Laplacian viscosity (Large et al., 2001). The ocean model has an explicit free surface, with freshwater fluxes exchanged between the atmosphere and ocean (Griffies et al., 2001).

Air-sea fluxes are exchanged on the ocean model's time step of 2 hr. Insolation varies diurnally, with shortwave radiation penetrating downward through the water column according to the optical model of Morel and Antoine (1994). The solar penetration depends on a prescribed horizontally and seasonally varying chlorophyll climatology computed from 1997 to 2004 SeaWIFS data (Sweeney et al., 2005). For computational efficiency, the relatively small amount of solar radiation penetrating past 100 m is deposited entirely at 100-m depth. The calculation of the surface wind stress accounts for the velocity of the surface winds relative to the surface currents (Pacanowski, 1987).

2.2. FLOR Model

The GFDL FLOR model is a global CGCM, whose formulation corresponds to configuration FLOR-B01 of Vecchi et al. (2014). FLOR's ocean and sea ice components have the same grid spacing and land-sea mask as in CM2.1, but the ocean physics and numerics are updated as described by Delworth et al. (2012) and Vecchi et al. (2014) to include a more sophisticated ocean model (MOM5; Griffies, 2012) with a spatially and temporally varying z^* vertical coordinate that undulates in tandem with the sea surface; a biharmonic viscosity scheme, which results in much lower frictional dissipation for all but the smallest spatial scales (Griffies & Hallberg, 2000); a more accurate and less dissipative advection scheme based on the piecewise parabolic method (Colella & Woodward, 1984); an updated parameterization for mesoscale eddies (Ferrari et al., 2010); and a parameterization for submesoscale mixed layer eddies (Fox-Kemper et al., 2011). The ocean component also has an updated formulation for solar penetration—including an updated optical model (Manizza et al., 2005), an updated chlorophyll climatology based on 1997–2007 SeaWIFS data, and a deepening of the maximum shortwave penetration depth from 100 (CM2.1) to 300 m (FLOR). The ocean model time step is shortened from 2 hr (CM2.1) to 30 min (FLOR), to enable the coupled model to run stably in the presence of the stronger atmospheric variability associated with FLOR's higher atmospheric horizontal resolution.

Table 3
Global Coupled General Circulation Model Simulations Used in this Study

Coupled model	Simulation name	Ocean codebase	Atmospheric horizontal grid	Atmos levels	r_{thresh} (μm)	$\langle \overline{Q}_{TOA} \rangle$ (W/m^2)
CM2.1	CM2.1U_Control-1990_E1	MOM4p0d	2.5°lon × 2°lat	24	8.0	1.01
LOAR1	LOAR1_Control_1990_A15	MOM5	C48 (208 km)	32	9.0	0.87
FLOR	CM2.5_A_Control-1990_FLOR_B01	MOM5	C180 (55 km)	32	8.0	0.64
HiFLOR	CM2.5_A_Control-1990_hiFLOR_A07	MOM5	C384 (26 km)	32	8.0	0.53

Note. All share the same ocean grid (1° × 1° spacing telescoping to 0.33° meridional spacing near the equator, with 50 vertical levels). All have fixed year-1990 values of atmospheric trace gases, insolation, aerosols, and land cover. $\langle \overline{Q}_{TOA} \rangle$ is the global-mean top-of-atmosphere net radiative heating of the planet, averaged over the first 100 years of simulation. The cloud parameter r_{thresh} is the liquid drop radius threshold for removal by autoconversion; increasing r_{thresh} increases stratus cloudiness, which raises the planetary albedo and reduces $\langle \overline{Q}_{TOA} \rangle$. Based on ocean observations over the past several decades, recent estimates put the Earth's $\langle \overline{Q}_{TOA} \rangle$ at 0.7±0.1W/m^2 (Johnson et al., 2016) or 0.6±0.4W/m^2 (Wild, 2017; Wild et al., 2015). CM2.1 = Coupled Model version 2.1; LOAR1 = Low Ocean Atmosphere Resolution version 1; FLOR = Forecast-oriented Low Ocean Resolution; HiFLOR = High Forecast-oriented Low Ocean Resolution; MOM = Modular Ocean Model.

The atmosphere and land components of FLOR are identical to those in Coupled Model version 2.5 (Delworth et al., 2012) and have refined grid spacing compared to CM2.1. The atmosphere component has a finite volume dynamical core, formulated on a cubed sphere grid (Putman & Lin, 2007), with 180 grid points along each edge of the cube (denoted "C180"), giving approximately 55 km × 55 km (0.5° × 0.5°) horizontal cells. The atmospheric GCM (AGCM) has 32 vertical levels, with the eight extra levels relative to CM2.1 concentrated near the tropopause. The atmospheric physics parameterizations in FLOR are unchanged from CM2.1, apart from a retuning of the liquid cloud droplet radius threshold for removal by autoconversion (which primarily affects the brightness of low stratus clouds) to bring the global-mean top-of-atmosphere net radiative heating averaged over the first century of simulation ($\langle \overline{Q}_{TOA} \rangle$ in Table 3) into accord with the 0.6–0.7 W/m^2 estimates based on ocean observations over the past several decades (Johnson et al., 2016; Wild, 2017; Wild et al., 2015). Other changes in FLOR/Coupled Model version 2.5 include an improved land component Land Model version 3 (LM3; Milly et al., 2014) and higher albedos for snow and sea ice that are in better agreement with observations (Delworth et al., 2012). FLOR's AGCM time step is 3 hr for radiation and 20 min for other atmospheric physics. Air-sea fluxes are exchanged with the ocean every 1 hr, that is, every other ocean time step.

FLOR has already contributed to remarkable advances in simulating and predicting ENSO and has been providing real-time global seasonal forecasts to the NMME every month since early 2014. With its excellent representation of tropical rainfall, ENSO patterns, midlatitude storms, and continental topography, FLOR has improved understanding and predictions of ENSO's effects on global weather and climate—including seasonal temperature and rainfall over land (Jia et al., 2015), extratropical storm tracks (Yang et al., 2015), regional hurricane activity (Krishnamurthy et al., 2016; Murakami et al., 2015; Murakami, Vecchi, Delworth, et al., 2017; Vecchi et al., 2014; Zhang et al., 2016), and the Great Plains Low-Level Jet (Krishnamurthy et al., 2015). FLOR has also helped to clarify the links among tropical Pacific climate, North American decadal drought, and global temperature trends (Delworth et al., 2015). As yet however, there has been no comprehensive evaluation of FLOR's tropical Pacific climatology; the present study aims to fill that gap.

2.3. LOAR1 Model

To isolate the role of atmospheric grid refinement in FLOR's performance relative to CM2.1, we also examine a model (Low Ocean Atmosphere Resolution version 1, or LOAR1; van der Wiel et al., 2016) that is identical to FLOR except for two aspects. First, LOAR1's atmosphere/land horizontal resolution is coarsened nearly to that of CM2.1 in the tropics—with a "C48" grid that is coarser than FLOR's by a factor of 3.75, giving approximately 208 km × 208 km (1.875° × 1.875°) spacing. Second, the liquid cloud drop radius threshold for autoconversion removal (r_{thresh}) is increased from 8 to 9 μm, which slightly increases stratus cloudiness and raises the planetary albedo; this reduces LOAR1's $\langle \overline{Q}_{TOA} \rangle$ from 1.3 to 0.9 W/m^2, close to the 1.0 W/m^2 value of CM2.1 (Table 3).

Beyond its utility for the present study, LOAR1 has also contributed to the development of a new GFDL coupled model (Seamless system for Prediction and EArth system Research [SPEAR]) which is optimized for seasonal-to-decadal applications and forecasting. SPEAR leverages the new technology and parameterizations developed for the Coupled Model version 4 CGCM (Zhao et al., 2018a, 2018b) that is GFDL's main model contribution to Coupled Model Intercomparison Project phase 6. SPEAR will be documented in a future study.

2.4. HiFLOR Model

To further explore the impacts of horizontal grid refinements in the atmospheric component, we examine the HiFLOR coupled GCM (Murakami et al., 2015). HiFLOR is very similar to FLOR except for a further doubling of the horizontal resolution of the atmosphere and land components to "C384," with cells approximately 26 km × 26 km (0.23° × 0.23°). The only other changes from FLOR to HiFLOR are the following: (1) HiFLOR's atmospheric dynamics time step is halved relative to FLOR, to ensure numerical stability at HiFLOR's increased atmospheric resolution (the physics time steps for the convection, cloud, and radiation schemes remain unchanged); (2) the ocean surface roughness (used to compute the surface wind stress) is reduced to a constant value for wind speeds above 40 m/s, to improve the simulation of tropical storms; and (3) an improved terrain mapping algorithm is used to compute the land mask and topography.

HiFLOR is the first global model to demonstrate skill in simulating and predicting tropical cyclone categories 4 and 5 and their regional seasonal-to-interannual statistics (Murakami et al., 2015) and has been used for research into regional tropical cyclone responses to ENSO and climate change (Murakami et al., 2016; Murakami, Vecchi, Delworth, et al., 2017; Murakami, Vecchi, & Underwood, 2017; W. Zhang et al., 2016), seasonal snowpack over the western United States (Kapnick et al., 2018), and attributing regional climate extremes (van der Wiel et al., 2016; van der Wiel, Kapnick, van Oldenborgh, et al., 2017; van der Wiel, Kapnick, & Vecchi, 2017).

Throughout this paper, we shall use the LOAR1 → FLOR → HiFLOR progression to assess impacts of increasing atmospheric resolution on the simulation of the tropical Pacific climatology. However, it is important to note that we have made only minimal attempts to optimize the tuning of the atmospheric parameterizations (e.g., clouds and convection) at these various resolutions. Further attention to either optimizing these parameters or revisiting the underlying structure of the parameterizations in the context of increased resolution could well yield additional gains in simulation.

3. Sea Surface Temperature

Figure 1 shows the annual-mean tropical Pacific SST from observations, along with the simulation biases and intermodel differences. The spatial mean (μ) and spatial standard deviation (σ) for each map are indicated above each panel. The observations (Figure 1a) show a warm pool in the west and an equatorial cold tongue in the east which connects to the South American coast. East of 130°W, there is strong meridional asymmetry about the equator, with warm SST along 5–10°N and near the Central American coast, cold SST south of the equator, and very cold SST along the South American coast.

As described in Wittenberg et al. (2006), the CM2.1 simulation (Figure 1b) has a strong warm bias along the South American coast, an overly strong equatorial cold tongue, a west Pacific warm pool that is too meridionally confined, and an excessive eastward extension of the northern lobe of warm pool water into the central Pacific. CM2.1's tropical Pacific root mean square error (δ) of the SST relative to observations in Figure 1b is almost entirely attributable to the bias in spatial pattern; the component μ^2/δ^2 of the mean square error attributable to the spatial-mean bias is only 4%. CM2.1's climatological zonal SST gradient ($\partial_x \overline{T}$) along the equator is too strong west of the dateline, and the meridional SST gradient ($\partial_y \overline{T}$) is too strong on the poleward flanks of the equatorial cold tongue. CM2.1 would thus require stronger-than-observed equatorial warm SST anomalies (SSTAs) in order for atmospheric deep convection, which tends to develop over the warmest total SST, to shift eastward and equatorward during El Niño.

The improved ocean/atmosphere physics and numerics in LOAR1 (Figure 1d) greatly improve its climatological SSTs relative to CM2.1, substantially reducing both the equatorial cold bias and the South American coastal warm bias. LOAR1 slightly worsens the cold biases in the southwestern and northwestern tropical Pacific, but its overall δ is reduced and its μ nearly vanishes.

The atmospheric refinement in FLOR (Figures 1e and 1f) further improves the climatological SST relative to LOAR1 and CM2.1. The equatorial cold SST bias has nearly vanished in FLOR; and both the Peruvian coastal warm bias and the excessive SST contrast between the cold tongue and the warm pool/ITCZ are greatly reduced. The spatial pattern improvements in most other regions result in FLOR having a smaller overall δ than LOAR1. However, FLOR's basin-mean cold bias is slightly greater than in LOAR1 and CM2.1, and FLOR does have stronger cold biases near Fiji (180°W, 20°S) and near Central America (e.g., 90°W, 10°S).

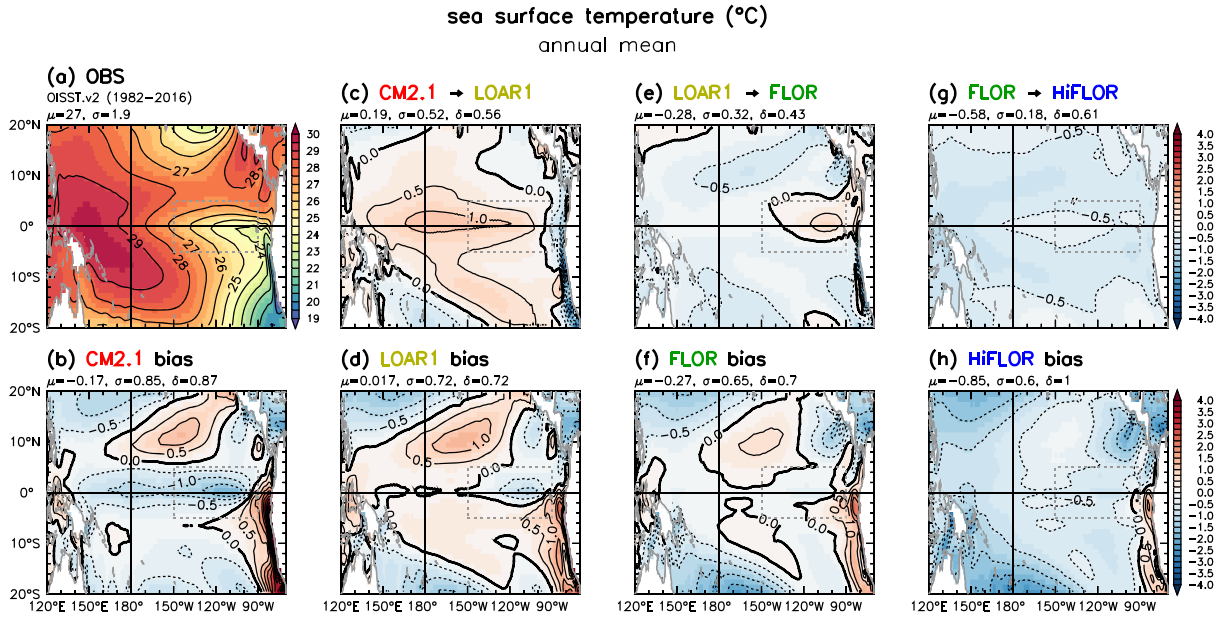

Figure 1. Observed and simulated tropical Pacific climatological annual-mean SST (°C). Shading is incremented every half-contour. See Tables 1–3 for data set abbreviations. (a) OISST.v2 observations, averaged 1982–2016. Bottom row (b, d, f, and h) shows each model's bias relative to (a), for simulated SST averaged over years 1–100 of each control run. Remaining top panels show the stepwise intermodel SST change, due to (c) improved ocean/atmosphere physics, LOAR1 minus CM2.1; (e) atmospheric grid refinement, FLOR minus LOAR1; and (g) further atmospheric grid refinement, HiFLOR minus FLOR. Labels atop each panel indicate the spatial mean μ and standard deviation σ. For the difference plots, an additional label indicates the spatial root-mean-square difference $\delta = (\mu^2 + \sigma^2)^{1/2}$. Dotted gray box is the Niño-3 region (150–90°W, 5°S–5°N) for reference.

The further atmospheric refinement in HiFLOR (Figures 1g and 1h) cools the tropical Pacific SST by 0.6 °C relative to FLOR, which worsens the overall cold SST bias. As discussed in section 5, this basinwide cooling is linked to reduced high cloudiness in HiFLOR, which strengthens the net longwave cooling at the surface. A version of HiFLOR with r_{thresh} reduced from 8.0 to 7.0 μm showed a 35% smaller tropical Pacific basin-mean cold bias, due to reduced low cloud. However, this change also degraded HiFLOR's simulation of ENSO and tropical cyclones, and so subsequent studies thus far have all used the version of HiFLOR described in this paper. Relative to the cooler spatial-mean SST, however, the spatial *pattern* of climatological SST actually slightly *improves* in HiFLOR: σ decreases from 0.65 (FLOR) to 0.6 ° C (HiFLOR), and HiFLOR shows some reduction in the excessive SST contrast between the equator and 10°N.

Thus, proceeding from CM2.1 → LOAR1 → FLOR → HiFLOR results in ever more realistic climatological SST contrasts between the equator and off-equator, between the equatorial eastern and western Pacific, and between the Peruvian coastal waters and the waters farther offshore. The equatorial and coastal SST improvements are mainly attributable to LOAR1's improved ocean/atmosphere physics and numerics, while the meridional SST gradient improvements are attributable to both that reformulation and to the refined atmospheric resolution in FLOR and HiFLOR.

4. Rainfall

Figure 2 shows the observed and simulated annual-mean tropical Pacific rainfall. Impacts of the rainfall on the ocean salinity are discussed in Appendix I.

Observations show heavy rainfall in the ITCZ (4–12°N), SPCZ (4–14°S west of 140°W), and west of 160°W. The southeast tropical Pacific is dry, aside from a weak double ITCZ along 4°S which emerges especially during El Niño years in boreal spring. The strong zonal and meridional asymmetries of the annual-mean rainfall largely mirror those of the SST (Figure 1).

In contrast to SST, the time-mean tropical rainfall is less well constrained by observations. Adler et al. (2012) suggest a 10–20% dry bias in the Global Precipitation Climatology Project (GPCP) product over the tropical Pacific, while other studies suggest a global dry bias of 5–9% in GPCP over the oceans (Behrangi et al., 2014; L'Ecuyer et al., 2015; Rodell et al., 2015). Despite this uncertainty, it is clear that apart from a clear dry bias near

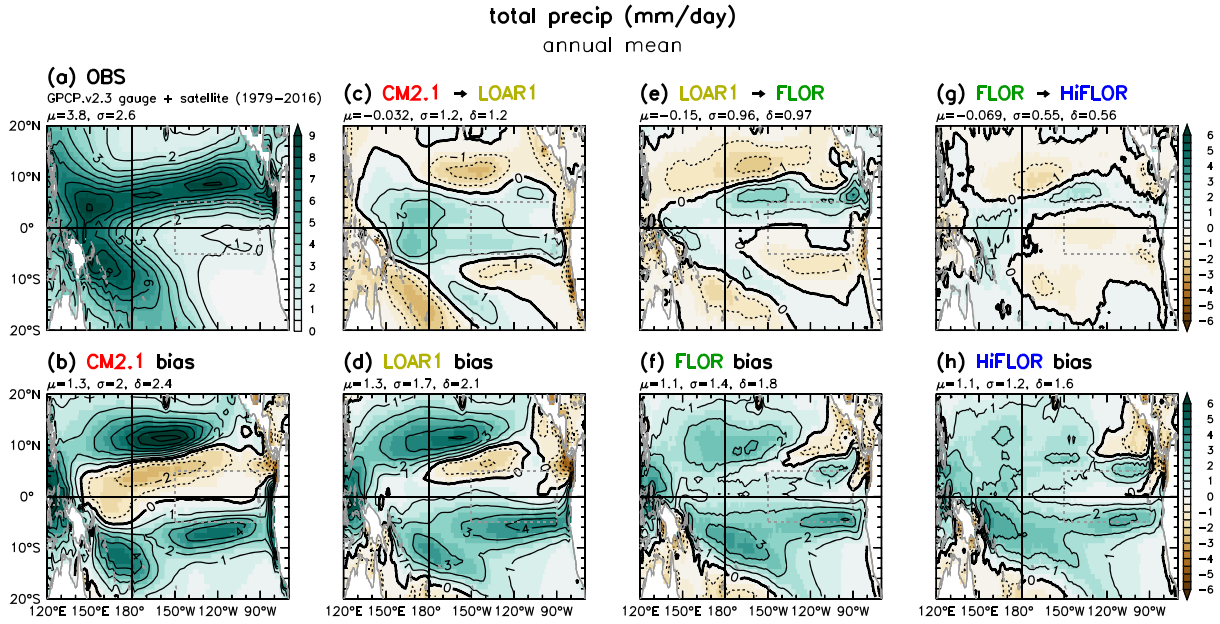

Figure 2. As in Figure 1 but for rainfall (mm/day). Observations (a) are from GPCP.v2.3, averaged 1979–2016.

the equator, CM2.1 generates too much rainfall over the tropical Pacific, especially in the convergence zones. CM2.1 rains too much in the southeast Pacific, especially along the South American coast and along 7°S where an excessive "southern ITCZ" appears in boreal spring. CM2.1's SPCZ and ITCZ are also displaced poleward of their observed positions.

Because the local gross moist instability of the tropical troposphere is partly determined by the difference between the local SST and tropical-mean SST (Xie et al., 2010), CM2.1's rainfall bias patterns (Figure 2b) somewhat resemble its SST bias patterns (Figure 1b)—with wet biases near warm biases in relative SST and dry biases near cold biases in relative SST. However, there are some important differences between the bias patterns of rainfall and SST, which can be understood by looking at the background climatological SST and rainfall patterns in Figures 1a and 2a. CM2.1's rainfall biases tend to be the strongest near the deep convective zones (ITCZ and SPCZ) and over the warm pool, where SSTs are closer to the convective threshold and the rainfall responds more strongly to SST biases. In contrast, CM2.1's rainfall biases are more muted in the dry zone near the equator, where there is so little rainfall to begin with that CM2.1's cold SST biases can only suppress a small additional amount of rainfall.

Compared to CM2.1, LOAR1 has an improved pattern of annual rainfall (Figure 2d), mirroring the improved SST contrasts described in the previous section. LOAR1's ITCZ and SPCZ shift eastward and equatorward, its southeast Pacific (double) ITCZ rainfall weakens, and it produces much less rain along the coast of South America. FLOR and HiFLOR extend these improvements and also reduce the excessive basin-mean rainfall (Figures 2f and 2h).

All four simulations show more rainfall than observed over the tropical Pacific, especially in the atmospheric convergence zones. This is also true for the tropical Indian and Atlantic oceans (not shown), and all four models produce excessive global rainfall relative to GPCP.v2.3. Taking the observations at face value, the models' excessive global rainfall would have to be balanced by excessive global evaporation, presumably over the tropical oceans. The next section will show that the simulations do exhibit excessive evaporation over the tropical Pacific.

5. Surface Heat Fluxes

5.1. Relevance and Constraints

In the absence of strong secular trends, the local time-mean net surface heat flux (i.e., ocean heat uptake) must balance the local time-mean ocean-dynamical cooling (ODC) arising from subsurface advection and diffusion. The pattern of time-mean net surface heat flux can therefore serve as a proxy for the intensity of local ODC.

Despite recent progress toward constraining global-mean estimates of the time-mean surface heat fluxes (Johnson et al., 2016; Wild, 2017), the pattern of net heat flux into the tropical Pacific ocean remains uncertain (Carton, Chepurin, Chen, & Grodsky, 2018), due to difficulties estimating the near-surface specific humidity, wind speed, and exchange coefficients that govern the evaporative cooling (Brown & Kummerow, 2014; Gainusa-Bogdan et al., 2015; Josey et al., 2014; Valdivieso et al., 2017) and the cloud properties, aerosols, surface albedos, and skin temperatures that govern the net shortwave heating and longwave cooling (Raschke et al., 2016; Wild, 2017).

The ERA-Interim (ERA-I) reanalysis agrees well with dynamically constrained observational estimates of the global surface heat flux components (L'Ecuyer et al., 2015; Liu et al., 2015; Stephens & L'Ecuyer, 2015; Wild et al., 2015), and so we shall use it as our main observational reference. However, we note that ERA-I may overestimate evaporation due to overly dry near-surface air (Brown & Kummerow, 2014; Gainusa-Bogdan et al., 2015) and may also underestimate the sensible heat flux (which is a relatively weak term over the tropical Pacific). We shall therefore also consider additional observational estimates for the heat fluxes.

5.2. Zonal Mean

Figure 3a shows the zonal-mean annual-mean surface heat fluxes over the tropical Pacific ocean, from the observational estimates and simulations. Shortwave radiation, which is the strongest heating term at 200–250 W/m^2, peaks near the equator and dims beneath the cloudy ITCZ along 7°N. Latent cooling from evaporation, the strongest cooling term at 80–150 W/m^2, peaks in the warm, windy, dry zones near 14°S and 18°N and weakens in the cold/calm regime near the equator. In contrast to the shortwave heating and evaporative cooling, the 40–60 W/m^2 of longwave cooling and 5–15 W/m^2 of sensible cooling are much weaker and more meridionally uniform.

Figure 3a shows that over the tropical Pacific ocean, both ERA-I and the simulations exhibit stronger evaporation (with less net heat uptake and implied ODC) than do the buoy-calibrated satellite observations. The spread of zonal means is greatest near 10°N, where there is a very large (40–50 W/m^2) disparity in the latent heat flux between SeaFlux.v1 and the simulations. The disparity is larger for the latent heat flux than for the other flux components.

Compared to the large spread among the observational estimates, the differences among the simulations are actually rather small—highlighting the need for improved observational constraints for the surface heat fluxes. All four models appear to give too much shortwave heating between 3° and 10°N. The simulations of the latent and net heat fluxes (for which the observational spread is the greatest) are closer to ERA-I than to the other observational products.

CM2.1 produces too much shortwave heating near the equator, due to its poleward-displaced ITCZ. LOAR1 reduces this bias, resulting in less ocean heat uptake and less implied ODC; this is likely tied to LOAR1's warmer equatorial SST (Figure 1c), which favors greater development of atmospheric deep convection near the equator (Figure 2c).

Compared to LOAR1, the higher-resolution FLOR and HiFLOR show slightly more meridional asymmetry in the surface heat fluxes, with more solar heating and ODC north of 8°N and more evaporation and less ODC south of the equator. This strengthens/improves the ocean heat uptake in FLOR and HiFLOR between 8° and 15°N but weakens (degrades) it between 8° and 15°S. FLOR and HiFLOR also show progressively more off-equatorial longwave cooling than CM2.1, LOAR1, and the observations, contributing to the progressively cooler SST in FLOR and HiFLOR (Figures 1e and 1g).

5.3. Equatorial Zone

Figure 3b compares the Pacific annual-mean surface heat fluxes near the equator. Shortwave heating is strongest under the clear skies of the central Pacific and weakest under the deep convection zones of the west Pacific and the stratocumulus zones of the east Pacific. Evaporation peaks in the warm and windy western/central Pacific and is the weakest in the cool and calm east Pacific. Compared to the shortwave and latent fluxes, the longwave and sensible fluxes have much less zonal structure near the equator and differ less among the observational estimates. The net surface flux strongly heats the equatorial zone (especially in the east), implying a strong compensating local ODC below the surface.

Near the equator in the western/central Pacific (130°E–120°W), there is 20–30 W/m^2 less solar heating in ERA-I than in the satellite estimates from ISCCP and CERES. This is in contrast to the South American coast,

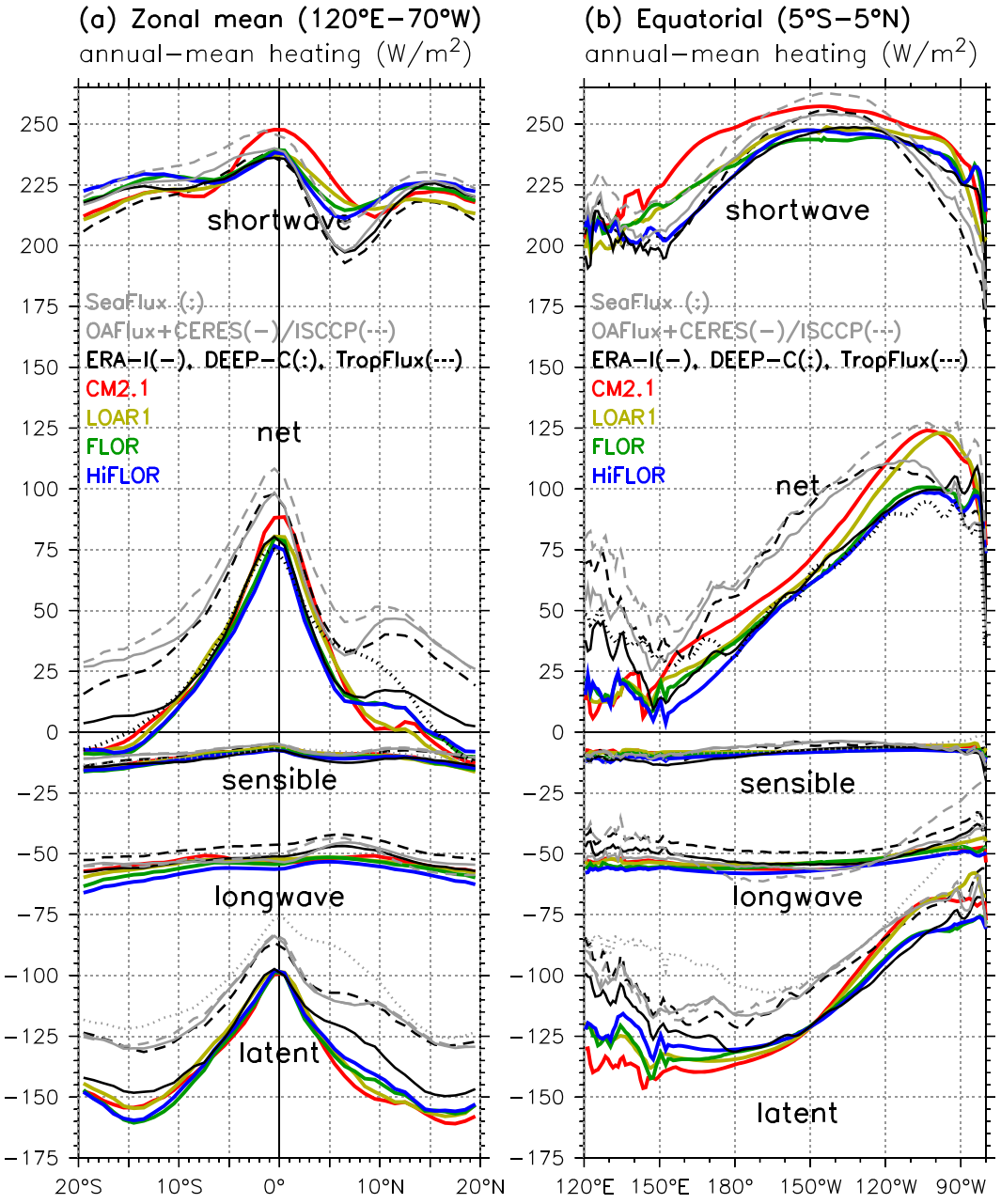

Figure 3. Annual mean surface heat fluxes (W/m^2) into the Pacific ocean (positive values heat the ocean): (a) zonally averaged 120°E–70°W, and (b) meridionally averaged 5°S–5°N. Thick colored lines are for years 1–100 of the simulations from CM2.1 (red), LOAR1 (yellow), FLOR (green), and HiFLOR (blue). Gray lines are satellite- and/or buoy-based estimates from the SeaFlux.v1 turbulent fluxes (1998–2007, dotted); OAFlux.v3 turbulent fluxes + CERES.Ed2.8 radiation (2001–2015, solid); and OAFlux.v3 turbulent fluxes + ISCCP-FD radiation (1984–2009, dashed). Black lines are reanalysis estimates from ERA-I (1979–2016, solid); DEEP-C.v3 (1985–2015, dotted); and TropFlux.v1 (1979–2016, dashed).

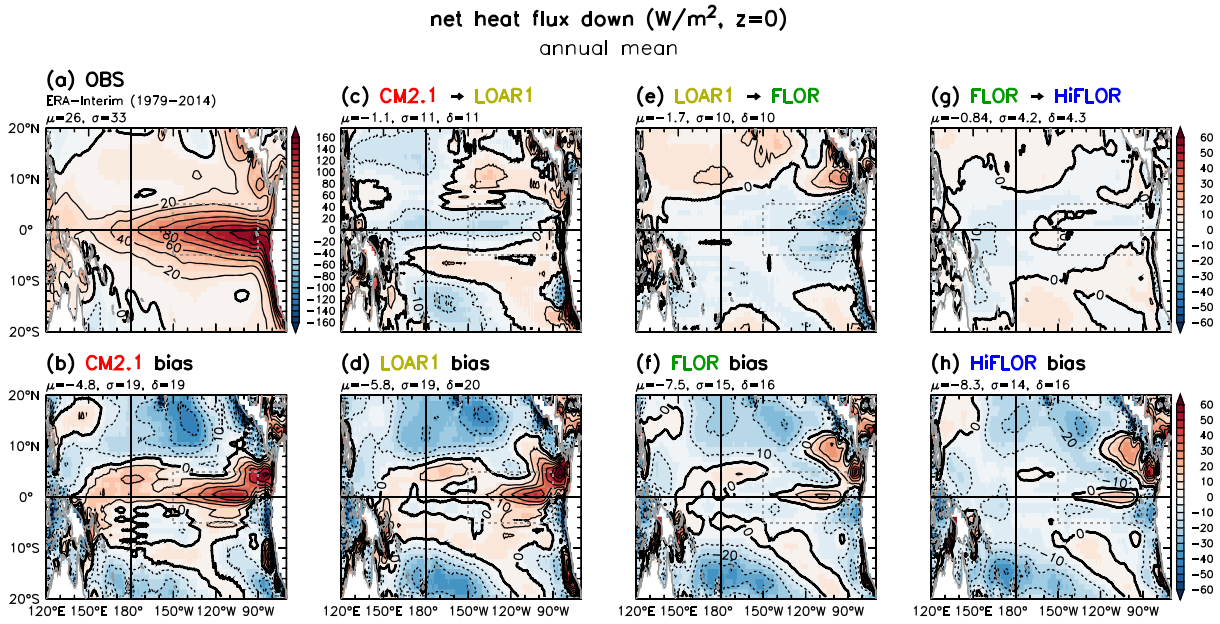

Figure 4. As in Figure 1 but for net surface air-sea heat flux (W/m^2, positive values heat the ocean). Observations (a) are from ERA-Interim, averaged 1979–2014.

where ERA-I has *more* solar heating than ISCCP and CERES. ERA-I also has stronger evaporative cooling near the equator than in the buoy-calibrated SeaFlux.v1, OAFlux, and TropFlux products. With less solar heating and more evaporative cooling, ERA-I thus has a weaker net surface heat flux (and implied ODC) than the other observational products. For the net heat flux, ERA-I agrees well with the DEEP-C estimates near the equator, though ERA-I is weaker in the west and slightly stronger in the east.

Despite the uncertain observational estimates, it is clear that the models overestimate the solar heating at the eastern edge of the warm pool (150°E–180°E) and in the east Pacific (110°W–80°W), giving too little contrast between the cloudy and clear zones near the equator. The models also show too much evaporation near the equator, especially in the west Pacific where the trade winds are too strong. The shortwave and evaporation biases partly cancel, resulting in net surface heat fluxes that are in reasonable agreement with ERA-I and DEEP-C. However, the models do show a stronger east-west contrast of the net surface heat flux near the equator, due mainly to stronger evaporation and weaker implied ODC in the west.

From CM2.1 → LOAR1 → FLOR → HiFLOR, the equatorial solar heating improves (weakens). Compared to CM2.1 and LOAR1, the near-equatorial evaporation in FLOR and HiFLOR is weaker in the west and stronger in the east, reducing the excessive zonal contrast of evaporation. East of 150°E, the near-equatorial net heat uptake weakens from CM2.1 → LOAR1 → FLOR → HiFLOR, due to less shortwave heating and more evaporation and consistent with weaker ODC associated with weakened trade winds and a flatter thermocline along the equator (described below). The net heat fluxes in FLOR and HiFLOR are nearly identical to those in ERA-I and DEEP-C, except in the west where FLOR and HiFLOR show less heat flux entering the ocean than observed.

5.4. Surface Heat Flux Maps

Figure 4 shows the pattern of annual-mean net surface heat flux into the tropical Pacific ocean between 20°S and 20°N. The patterns of the individual shortwave, longwave, latent, and sensible heating components are discussed in Appendix F.

ERA-I indicates an ocean heat uptake of 26 W/m^2 averaged over this region. In the cold upwelling regions near the equator and eastern boundary, with relatively clear skies with weak evaporation, the time-mean ocean heat uptake can exceed 150 W/m^2.

Compared to ERA-I, CM2.1 takes up 5 W/m^2 less heat over the tropical Pacific, with less heat uptake off-equator and near the east/west boundaries, and more heat uptake in the equatorial Pacific. The overly strong ODC contrast between the cold tongue and the rest of the tropical Pacific mirrors CM2.1's overly strong SST contrast (Figure 1b).

LOAR1 takes up even less heat than CM2.1, especially near the equator and in the southwest/northwest corners of the tropical Pacific (Figure 4c). This slightly worsens LOAR1's bias toward weak basin-mean heat uptake but also appropriately reduces the excessive heat uptake near the equator (Figure 4d). Along the equator, LOAR1's *reduced* heat uptake relative to CM2.1 acts to *oppose* LOAR1's warmer SST (Figure 1c). Thus, LOAR1's warmer equatorial SST must be attributable to weaker ODC below the surface. Similarly, LOAR1's cooler SSTs near the Peru coast must be driven by stronger ODC there.

FLOR further weakens the basinwide ocean heat uptake (Figure 4e), especially in the eastern Pacific between 12°S and 8°N due to greater evaporation and cloud shading than in LOAR1. This worsens FLOR's *spatial-mean* bias relative to CM2.1 or LOAR1, but FLOR's *spatial pattern* actually improves due to a reduced heating contrast between the equatorial zone and 10°N. Compared to LOAR1, FLOR's weaker heat uptake and warmer SST in the eastern equatorial Pacific, and stronger heat uptake and cooler SST north of 8°N, are consistent with the ODC changes driving the SST changes. However, in the remainder of the basin (including near the South American coast), FLOR's cooler SSTs appear to be driven by its reduced net surface heat flux relative to LOAR1.

As described in Appendix A, the multicentury warm drift below 100 m strengthens from LOAR1 to FLOR (Figures A1b and A1c), even as the surface heat uptake of the tropical Pacific weakens (μ in Figures 4d and 4f). FLOR's stronger warm drift must therefore be due to reduced poleward heat transport within the ocean.

Compared to FLOR, HiFLOR shows a slight reduction in its pattern bias (σ) relative to ERA-I and a further weakening of the basin-mean ocean heat uptake (Figure 4g), mainly west of the dateline and near the equator. Appendix F shows that this reduced heat uptake is linked to cloudier conditions west of the dateline between 15°S and 8°N and stronger longwave cooling away from the equator.

6. Surface Wind Stress

The tropical Pacific trade winds gather moisture from the ocean to fuel atmospheric convection. The winds also drive the ocean currents that transport water and heat across the basin. Along the equator, the easterly (i.e., westward) wind stress causes the sea surface to tilt upward, and the thermocline downward, toward the west; the sea surface tilt then generates an eastward pressure gradient within the equatorial upper ocean that helps to maintain the narrow EUC. The curl of the surface wind stress also drives upper-ocean *Sverdrup transports* (Appendix C), whose meridional divergences are linked to the tropical Pacific's intense zonal currents; and *Ekman transports* (Appendix D), particularly near the equator and eastern boundaries, which upwell cold, nutrient-rich water toward the surface. Here we describe the main features of the observed and simulated wind stress patterns. The meridional component of the wind stress is discussed in Appendix G.

6.1. Zonal Wind Stress

Figure 5 shows the annual-mean surface zonal wind stress ($\overline{\tau}^x$) over the tropical Pacific ocean. The observed easterly trade winds peak along 15°N and 15°S, while along the equator, the trade winds are weaker, with peak easterlies near 150°W and weak westerlies near the eastern and western boundaries.

CM2.1 has stronger-than-observed easterly $\overline{\tau}^x$ over most of the tropical Pacific, especially off-equator and in the west (Figure 5b). Along the equator, CM2.1's overly strong easterly $\overline{\tau}^x$ steepens the zonal tilt of the thermocline, shoaling the thermocline in the east and intensifying the upper-ocean vertical temperature gradient ($\partial_z \overline{T}$) there (Figure 9b)—with subsequent impacts on the seasonal cycle and ENSO (Wittenberg et al., 2006).

LOAR1's $\overline{\tau}^x$ biases (Figure 5d) resemble those in CM2.1. Along the equator, LOAR1 has weaker easterlies than CM2.1 in the western and central Pacific, which would help to flatten LOAR1's equatorial thermocline. However, LOAR1 also has stronger easterlies in the northeast and southwest tropical Pacific than CM2.1—which (as described later) exacerbates the excessive off-equatorial cyclonic curl and poleward Sverdrup transport, further elevating LOAR1's equatorial thermocline.

FLOR's atmospheric refinement greatly improves $\overline{\tau}^x$ relative to LOAR1, particularly near Central America and north of 15°N (Figure 5f). FLOR has much less of LOAR1's excessive cyclonic curl north of the equator, reducing FLOR's poleward Sverdrup transport near the equator and north of 12°N. However, FLOR's easterlies are now slightly too weak over the central equatorial Pacific, which would be expected to weaken the zonal tilt of FLOR's equatorial thermocline. FLOR's zone of cyclonic curl (and poleward Sverdrup transport) in the southwest equatorial Pacific is also situated closer to the equator than in LOAR1.

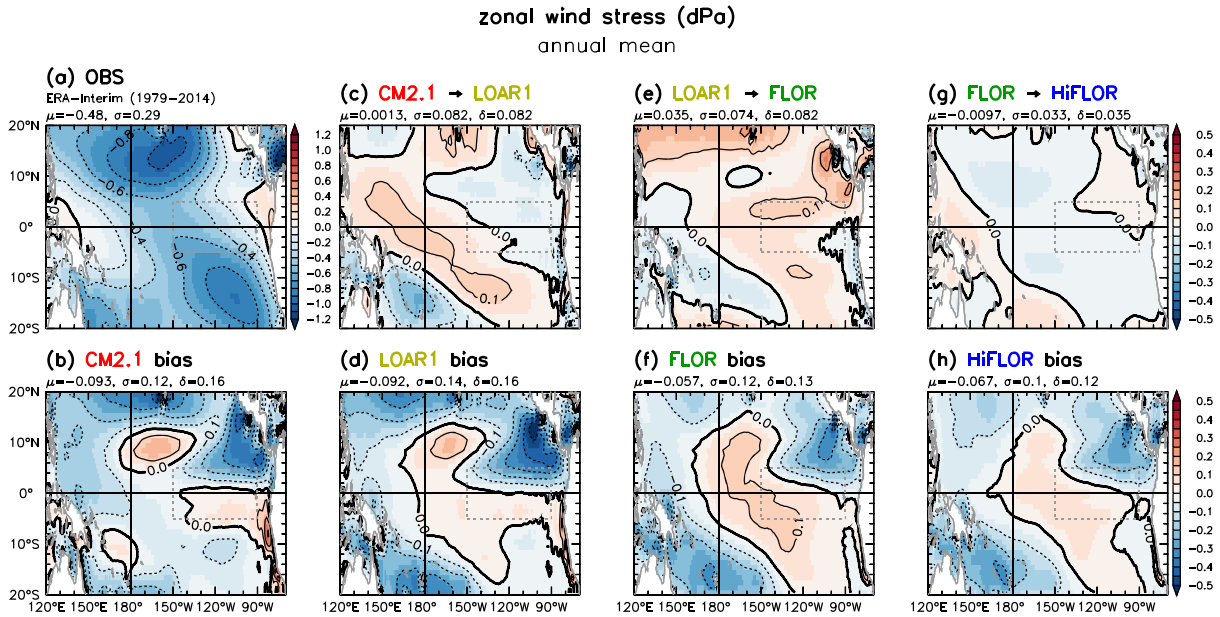

Figure 5. As in Figure 4 but for zonal surface wind stress (dPa). Positive values exert westerly (i.e., eastward) stress on the ocean.

HiFLOR shows further improvement in $\overline{\tau}^x$, with stronger easterlies in the central basin and weaker easterlies in the west Pacific.

6.2. Wind Stress Cyclonicity

Figure 6 shows the annual-mean cyclonicity of the surface wind stress on the ocean, defined here as

$$\mathrm{cycl}(\overline{\boldsymbol{\tau}}) = \mathrm{sgn}(y)\mathrm{curl}(\overline{\boldsymbol{\tau}}). \quad (1)$$

This is simply the wind stress curl, but with the sign flipped in the southern hemisphere so that positive values indicate cyclonic stress in both hemispheres. Cyclonic curl drives Ekman upwelling and poleward Sverdrup transport (Appendices B and C).

Observations (Figure 6a) show cyclonic curl near the atmospheric convergence zones, especially near the ITCZ and SPCZ and in the southeastern equatorial Pacific. CM2.1's excessive off-equatorial easterlies amplify the meridional shear of its wind stress ($\partial_y \overline{\tau}^x$), boosting the cyclonicity along 3°N and 7°S in the east Pacific, 13°N in the central Pacific, and 16°S in the west Pacific. LOAR1 actually expands these cyclonicity biases, especially near the SPCZ. In contrast, the improved atmospheric resolution and reduced rainfall in FLOR and HiFLOR greatly reduce their cyclonicity biases.

6.3. Sverdrup Transport

Figure 7 shows $\partial_y \overline{V}_S$, the meridional divergence of the Sverdrup transport implied by the surface wind stress.

As described in Appendix C, the zonal transport $\overline{U}_S$ at a given longitude must supply all of the $\partial_y \overline{V}_S$ between that longitude and the eastern boundary. Figure 7 thus lends insight into the structure of the tropical Pacific zonal currents, and also into the structure of the sea surface height and thermocline depth whose meridional slopes generate the upper-ocean pressure gradients needed to balance the Coriolis force acting on the zonal currents.

On the equatorward flanks of the observed off-equatorial easterly trade wind cores (Figure 5a), the wind stress curl is cyclonic. These cyclonic features induce poleward $\overline{V}_S$ near the equator in the western and southeast Pacific. The positive $\partial_y \overline{V}_S$ along the equator (Figure 7a) then elevates the equatorial thermocline and supports the eastward-moving EUC. The observed positive $\partial_y \overline{V}_S$ along 6°N is supplied from the west by the eastward-moving North Equatorial Countercurrent (NECC), while the negative $\partial_y \overline{V}_S$ along 10–4°S and 13°N supplies the westward-moving South Equatorial Current (SEC) and North Equatorial Current (NEC), respectively.

CM2.1's excessive cyclonicity (Figure 6b) enhances its poleward Sverdrup transport of upper-ocean heat away from the equator. CM2.1's extrema of $\partial_y \overline{V}_S$ are generally stronger than observed and displaced from their

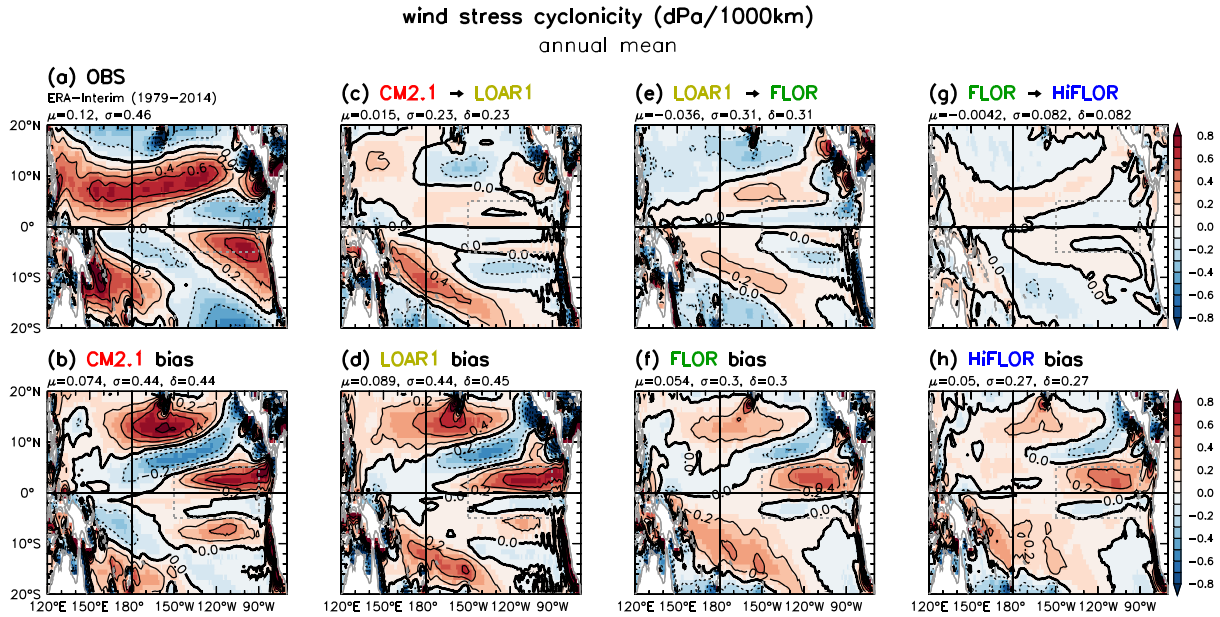

Figure 6. As in Figure 5 but for cycl(τ) = sgn(y)curl(τ), the cyclonicity of the surface wind stress (dPa (1,000 km)$^{-1}$). Positive values exert cyclonic stress on the ocean.

observed positions (Figures 7a and 7b). For example, the meridional divergence linked to the NECC is shifted northwest of its position in ERA-I, and the meridional divergence over the eastern equatorial Pacific cold tongue is shifted onto the equator, north of its position in ERA-I. LOAR1 weakens (improves) $\partial_y \overline{V}_S$ along 10°N, but otherwise shows little improvement. FLOR and HiFLOR, however, greatly reduce the off-equatorial $\partial_y \overline{V}_S$ biases, foreshadowing their improved off-equatorial zonal currents and associated meridional slopes of the thermocline (sections 7 and 8).

In both FLOR and HiFLOR, the $\partial_y \overline{V}_S$ in the eastern equatorial Pacific remains too strong and too centered on the equator, while that in the northeast tropical Pacific (associated with the NECC) remains too weak. Within

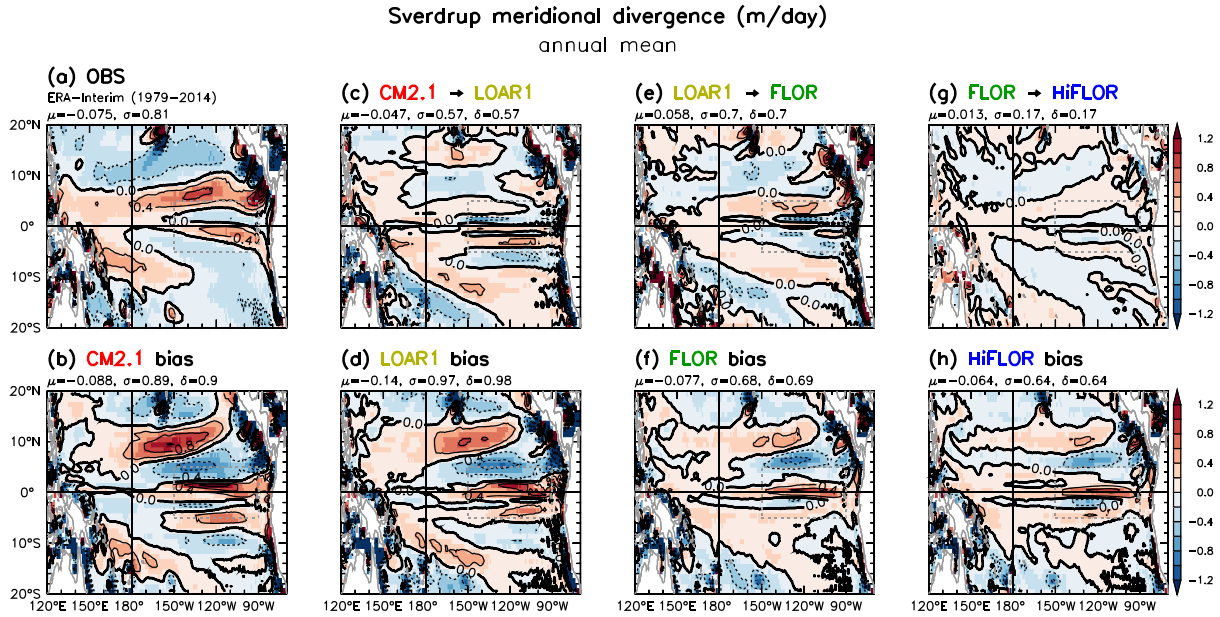

Figure 7. As in Figure 5 but for $\partial_y \overline{V}_S$, the meridional divergence (m/day) of the oceanic Sverdrup transport implied by the annual-mean surface wind stress.

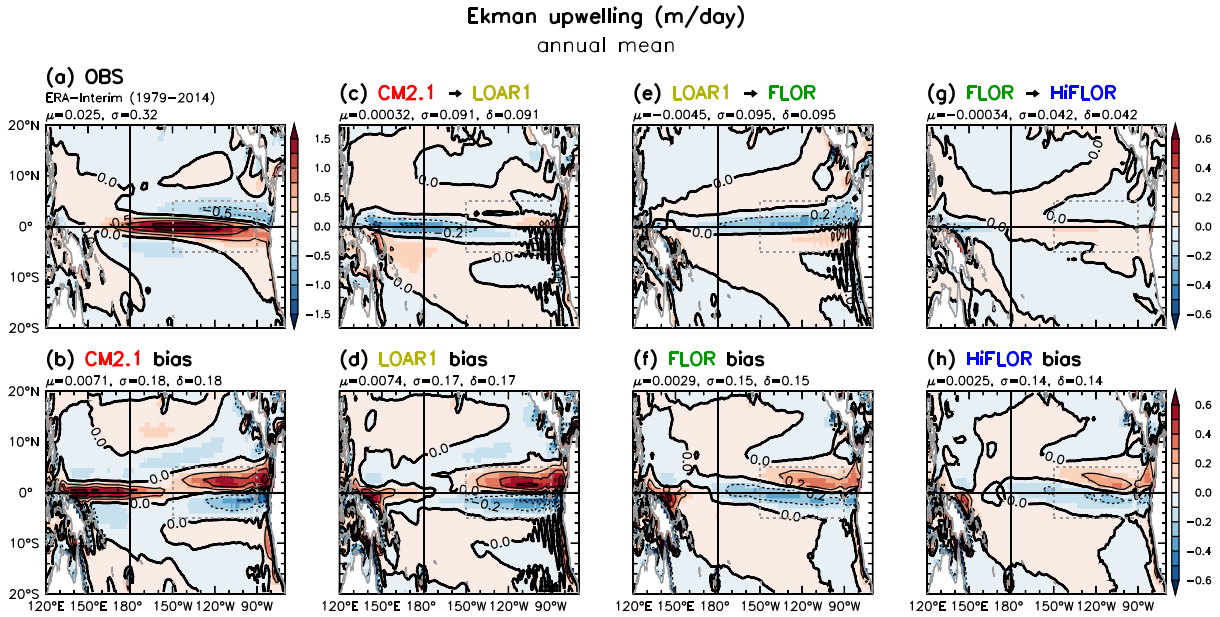

Figure 8. As in Figure 5 but for $\overline{w}_E$, the Ekman upwelling (m/day) implied by the annual-mean surface wind stress.

the 9–2°S band, FLOR retains a bias toward excessive $\partial_y \overline{V}_S$ which would be expected to discharge too much upper-ocean heat from that latitude band; but HiFLOR shows improvement in this regard.

6.4. Ekman Upwelling

As an initial estimate of the annual-mean upwelling driven by local winds, Figure 8 shows the Ekman upwelling velocity ($\overline{w}_E$; Appendix D) implied by the observed and simulated annual-mean wind stresses.

The $\overline{w}_E$ implied by the observed stress (Figure 8a) is strongest in the equatorial cold tongue—due to both the equatorial easterly winds in the central Pacific and the southerly winds in the east Pacific between the equator and 5°S. The $\overline{w}_E$ is also strong along the coast of South America, where southerly winds induce offshore Ekman transport fed by upwelling from below.

CM2.1's overly strong and westward-displaced equatorial trade winds (Figure 5b) produce equatorial $\overline{w}_E$ that is stronger and farther west than its observation-based counterpart (Figure 8b). In addition, CM2.1's weak southerlies in the east generate less $\overline{w}_E$ south of the equator between the equator and 5°S, making the subsurface cooling too symmetric about the equator.

Compared to CM2.1, LOAR1 (Figures 8c and 8d) greatly reduces the excessive $\overline{w}_E$ in the western and central Pacific, although it fails to improve the excessive symmetry in the east. FLOR (Figures 8e and 8f) does improve the east Pacific meridional asymmetry, by strengthening both the downwelling north of the equator and the upwelling south of the equator and along the coast of South America. However, FLOR also overly weakens $\overline{w}_E$ in the central equatorial Pacific, due to its weaker trade winds there. HiFLOR shows improvement in that regard by strengthening $\overline{w}_E$ along the equator.

7. Upper-Ocean Temperature Structure

This section describes the thermal structure of the tropical Pacific upper ocean, which is crucial to both the time-mean density stratification and the dynamics of the seasonal cycle and ENSO. Appendix H discusses the depth of the surface isothermal layer, and Appendix I discusses the upper-ocean salinity structure.

7.1. Equatorial Temperatures

Figure 9 shows the Pacific annual-mean upper-ocean temperature interpolated to the equator. Observations show the thermocline sloping down toward the west, with the peak thermal stratification ($\partial_z \overline{T}$) centered roughly on the 20 °C isotherm (Figure 9a). The weakest $\partial_z \overline{T}$ occurs in the surface mixed layer of the west Pacific warm pool (in the upper 75 m above the 28 °C isotherm) and in the 13 °C thermostad of the east Pacific between 200 and 250 m.

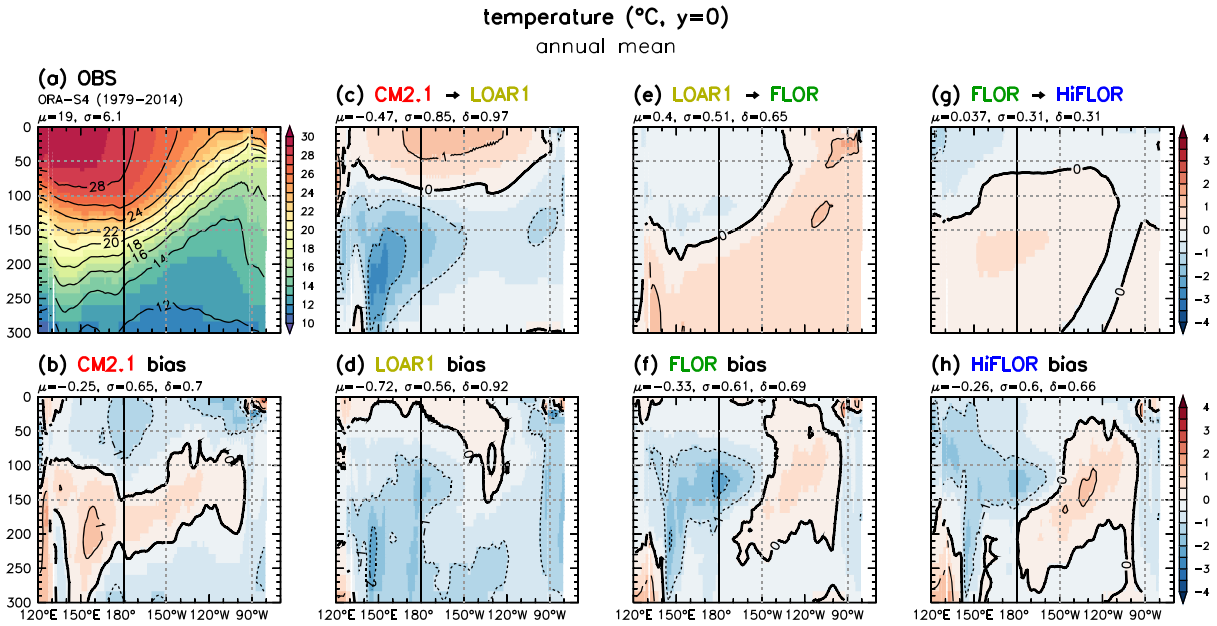

Figure 9. As in Figure 1 but for subsurface ocean temperature (°C) interpolated to the equator. Vertical axis is depth in meters. Observations (a) are from ORA-S4, averaged 1979–2014.

The equatorial Pacific in CM2.1 (Figure 9b) is generally too cold over the top 100 m, with a slightly more diffuse thermocline than observed, and a weaker 13 °C thermostad in the east. Some of the apparent diffuseness of CM2.1's annual-mean thermocline actually arises from the model's overly strong ENSO variability (Wittenberg et al., 2006), which amplifies the interannual fluctuations of thermocline depth and leads to excessive temporal "blurring" of the mean temperature profile (Ogata et al., 2013). Near South America, CM2.1 has excessive $\partial_z \overline{T}$ near the surface, due to both a warm SST bias and a cold bias at 30-m depth.

Compared to CM2.1, LOAR1 has a reduced cold bias above 50 m and slightly weaker/better $\partial_z \overline{T}$ near South America (Figures 9c and 9d). These improvements stem from LOAR1's flatter thermocline and weaker $\overline{w}_E$, associated with its weaker equatorial trade winds (Figure 5c) and possibly also from LOAR1's stronger TIWs (section 10). LOAR1 also has a slightly thicker/better 13° thermostad in the east than CM2.1. However, LOAR1 also develops a cold bias below 100 m, which is amplified in the west due to LOAR1's reduced zonal tilt of the thermocline. LOAR1's cooler temperatures below 100 m may be linked to its greater wind stress cyclonicity and Ekman suction in the southern tropical Pacific (Figures 6c and 8c), which help to cool the South Pacific source waters that feed into the lower part of the EUC (Gu & Philander, 1997; Z. ; Liu & Philander, 1995).

Compared to LOAR1, FLOR (Figures 9e and 9f) shows improved equatorial temperatures and $\partial_z \overline{T}$ (especially above 50 m), with weaker near-surface $\partial_z \overline{T}$ near South America, a reduced cold bias below the thermocline, and a thicker 13 °C thermostad. FLOR's reduced cold bias below 150 m may be due to its weaker wind stress cyclonicity and Ekman suction in both the southwest and northwest tropical Pacific (Figures 6e and 8e). FLOR's weaker equatorial easterly winds (Figure 5e) slightly over-flatten the thermocline. HiFLOR shows additional minor improvements, reducing the excessive $\partial_z \overline{T}$ in the thermocline west of 150°W (Figures 9g and 9h).

7.2. Zonal Mean Temperatures

Figure 10 shows the annual-mean upper-ocean temperatures averaged zonally across the Pacific basin. Observations show strong meridional asymmetry, with a prominent thermocline ridge near 8°N.

CM2.1's zonal-mean temperatures are too symmetric about the equator, with a subsurface cold bias at 8°S near 160-m depth and warm bias at 8°N near 125-m depth (Figure 10b). LOAR1 shows little improvement in this regard and also exhibits a broad cooling relative to CM2.1 below 100 m between 8°S and 10°N (Figures 10c and 10d).

FLOR, however, has substantially better meridional asymmetry (Figure 10f), consistent with its improved $\overline{\tau}^x$ structure and implied Sverdrup transports relative to LOAR1 (Figures 5f and 7f). FLOR does retain a zonal-mean cold bias between 14°S and 6°N and 100 and 220-m depth, likely linked to its excessive wind stress cyclonicity,

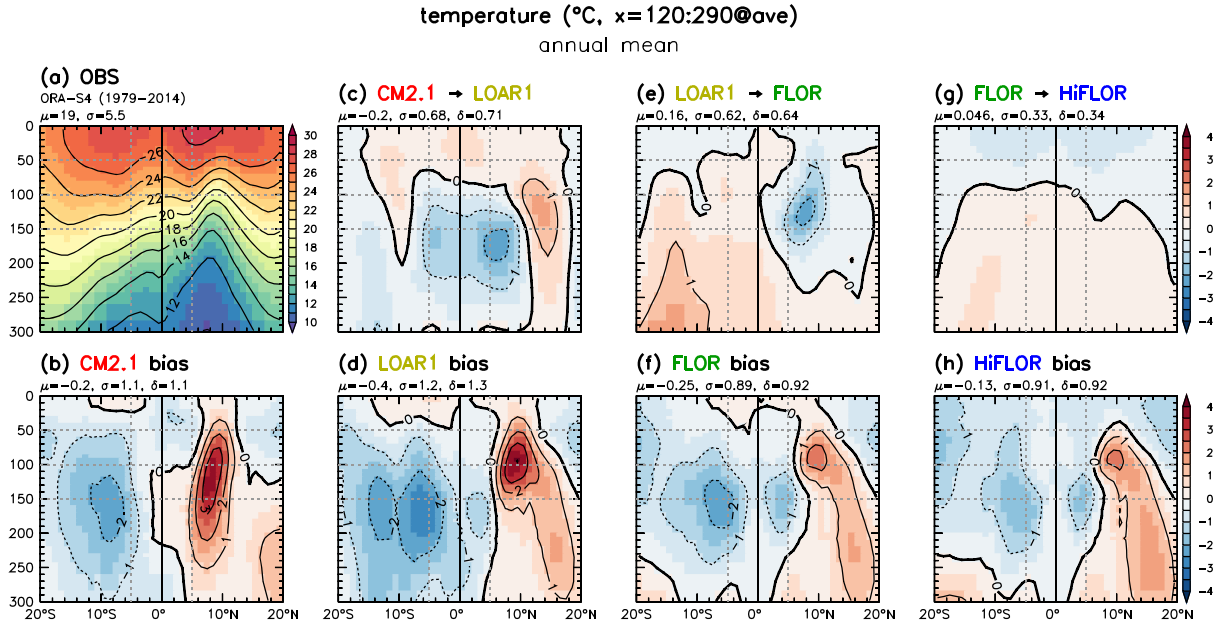

Figure 10. As in Figure 9 but for subsurface ocean temperature (°C) averaged zonally across the Pacific basin (120°E–70°W).

$\partial_y \overline{V}_S$, and $\overline{w}_E$ within this latitude band (Figures 6f, 7f, and 8f). HiFLOR shows further slight improvements in the near-equatorial cold biases between 100 and 220 m.

7.3. Upper-Ocean Heat Content

Figure 11 shows temperatures averaged over the top 300 m of the ocean. Observations (Figure 11a) show cool temperatures (i.e., low upper-ocean heat content) where the thermocline is shallow, in the east Pacific cold tongue and along 6–12°N. Observed temperatures are warmest in the thermocline troughs of the west Pacific warm pool near 160°W, 14°S and 150°E, 16°N.

In CM2.1 (Figure 11b), both the west Pacific warm pools and the north Pacific thermocline ridge along 6–12°N are weaker and less distinct than observed—giving too little meridional asymmetry of the heat content. In the eastern equatorial Pacific, CM2.1's thermocline is also slightly too shallow, which in combination with the warm SST biases near South America results in excessive $\partial_z \overline{T}$ near the surface (Figure 9b). LOAR1 actually worsens these heat content biases—further reducing the meridional asymmetry and shoaling the equatorial thermocline in both the western and far eastern Pacific (Figure 11c).

FLOR, however, greatly improves the heat content field and its meridional asymmetry relative to both LOAR1 and CM2.1—notably in the eastern Pacific, where FLOR's equatorial heat content is now very realistic. Near South America, FLOR's warmer upper-ocean temperatures (Figure 11e) and cooler SSTs (Figure 1e) combine to give weaker and more realistic $\partial_z \overline{T}$ near the surface. FLOR's realistic eastern equatorial Pacific temperature structure comes *despite* FLOR's lingering cold bias in the southwest tropical Pacific source waters of the EUC—foreshadowing that FLOR may have some compensating errors that help to heat the eastern equatorial Pacific. HiFLOR shows further slight improvements in the meridional asymmetry, with increased heat content near the dateline at 12°S.

8. Upper-Ocean Currents

8.1. Surface Zonal Currents

Figure 12 shows $\overline{u}_{30}$, the annual-mean zonal current averaged over the top 30 m of the tropical Pacific. Observations show a westward SEC straddling the equator (10° S–4° N), an eastward NECC between 4° and 9° N, and a westward NEC between 9° and 19° N. The thermocline ridge along 9° N (Figure 11a) has the NEC traversing along its northern slope and the NECC along its southern slope. The shears between the SEC and NECC, and between the SEC and EUC, are important since they give rise to near-equatorial TIWs. The TIWs stir water meridionally across the cold tongue front and also generate intense transient shears which enhance vertical mixing above the thermocline (Holmes & Thomas, 2015; Im et al., 2012; Moum et al., 2009, 2013).

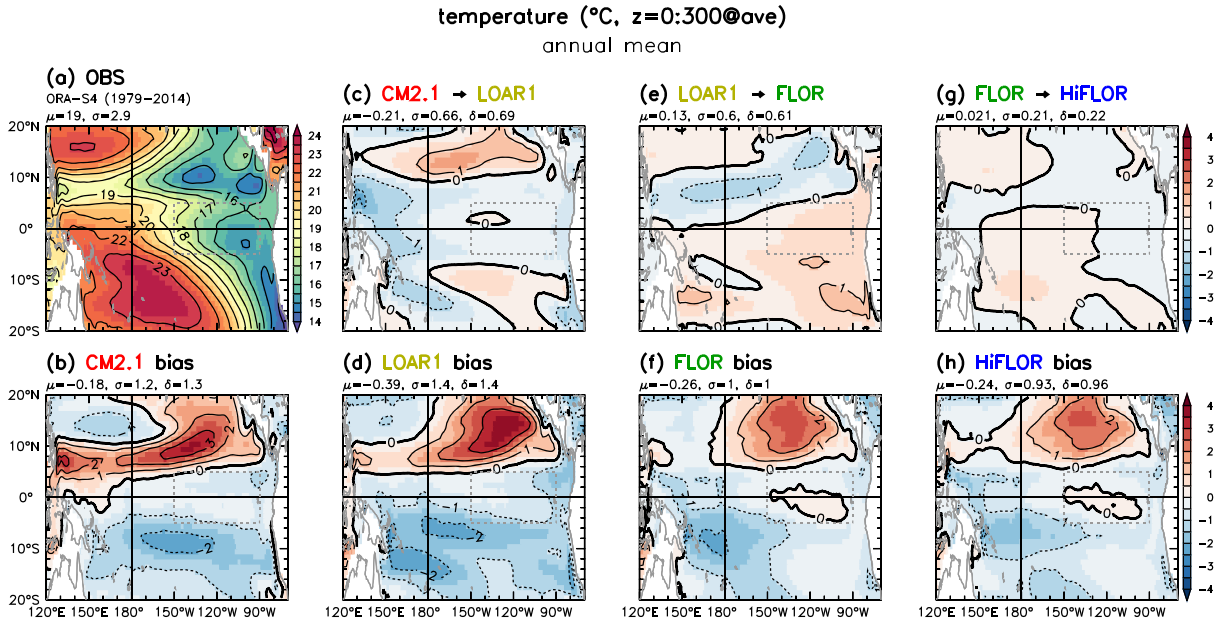

Figure 11. As in Figure 1 but for subsurface ocean temperature (°C) averaged vertically over the top 300 m of the ocean. Observations in (a) are from ORA-S4, averaged 1979-2014.

The time-mean near-surface zonal currents ($\overline{u}_{30}$) reflect not only the Sverdrup transport ($\overline{U}_S$; Appendix C) but also the Ekman transport ($\overline{U}_E$; Appendix D) and its vertical structure. The Ekman surface currents point more downwind than the total vertically integrated Ekman transport: for example, well north of the equator, the depth-integrated Ekman transport is 90° to the right of the wind stress, while the Ekman surface currents are only 45° to the right of the wind stress. While (D4) states that the zonal Ekman transport $\overline{U}_E$ is proportional to $\overline{\tau}^y$ far from the equator, it is clear from Figure 12 that $\overline{U}_E$ must contribute only weakly to $\overline{u}_{30}$, since the observed meridionally narrow zonal surface jets away from the equator do not mirror any similar structures in $\overline{\tau}^y$ (Figure G1).

Thus, it turns out that the Sverdrup component $\overline{U}_S$ strongly predicts the meridional structure of $\overline{u}_{30}$ away from the equator. As described in section 6 and Appendix C, the cyclonicity of the surface wind stress (Figure 6) sustains a poleward Sverdrup transport $\overline{V}_S$, whose meridional divergence $\partial_y \overline{V}_S$ (Figure 7) is compensated by zonal convergence $\partial_x \overline{U}_S$. Equation (C3) then relates the local zonal transport $\overline{U}_S$ to the eastward integral of $\partial_y \overline{V}_S$.

Figure 12 demonstrates that $\overline{u}_{30}$ is well predicted by the $\partial_y \overline{V}_S$ inferred from the wind stress. The eastward NECC feeds into the positive $\partial_y \overline{V}_S$ along 4–10°N, the westward NEC emerges from the negative $\partial_y \overline{V}_S$ along 10–20°N, and the westward southern branch of the SEC emerges from the negative $\partial_y \overline{V}_S$ along 4–6°S. The equator is a local minimum of the near-surface SEC, due to cancellation between the surface-intensified Ekman component (which is westward, driven directly by the westward winds) and the deeper eastward flow associated with the EUC (driven by an eastward subsurface pressure gradient, associated with the eastward downslope of the sea surface).

These observed features of $\overline{u}_{30}$ are also present in CM2.1 but with different intensities and spatial structure. CM2.1's biases in $\overline{u}_{30}$ (Figure 12c) can be understood by examining CM2.1's biases in $\overline{\tau}$ and implied $\partial_y \overline{V}_S$ (Figures 5b, G1b, and 7b). Consistent with Appendices C and D, CM2.1's $\overline{u}_{30}$ biases largely emanate westward from its biases in $\partial_y \overline{V}_S$ (Figure 7b), with some modification near the equator by the surface-intensified Ekman flow. For example, CM2.1's SEC is shifted west of its observed position, due to three biases in CM2.1: (1) westward-displaced trade winds, which cause westward displacement of the westward Ekman flow near the equator; (2) overly divergent $\overline{V}_S$ near the equator east of 150°W, which boosts the equatorial eastward $\overline{U}_S$ in the eastern and central Pacific; and (3) overly convergent $\overline{V}_S$ east of the dateline along 5°N and 3°S, which strengthens the westward $\overline{U}_S$ off-equator in the central and western Pacific. As a result of its westward-displaced SEC, CM2.1 actually exhibits *eastward* $\overline{u}_{30}$ along the equator between 120° and 100°W, which manifests as an excessive shoaling of the EUC relative to observations (Figure 13d, red line).

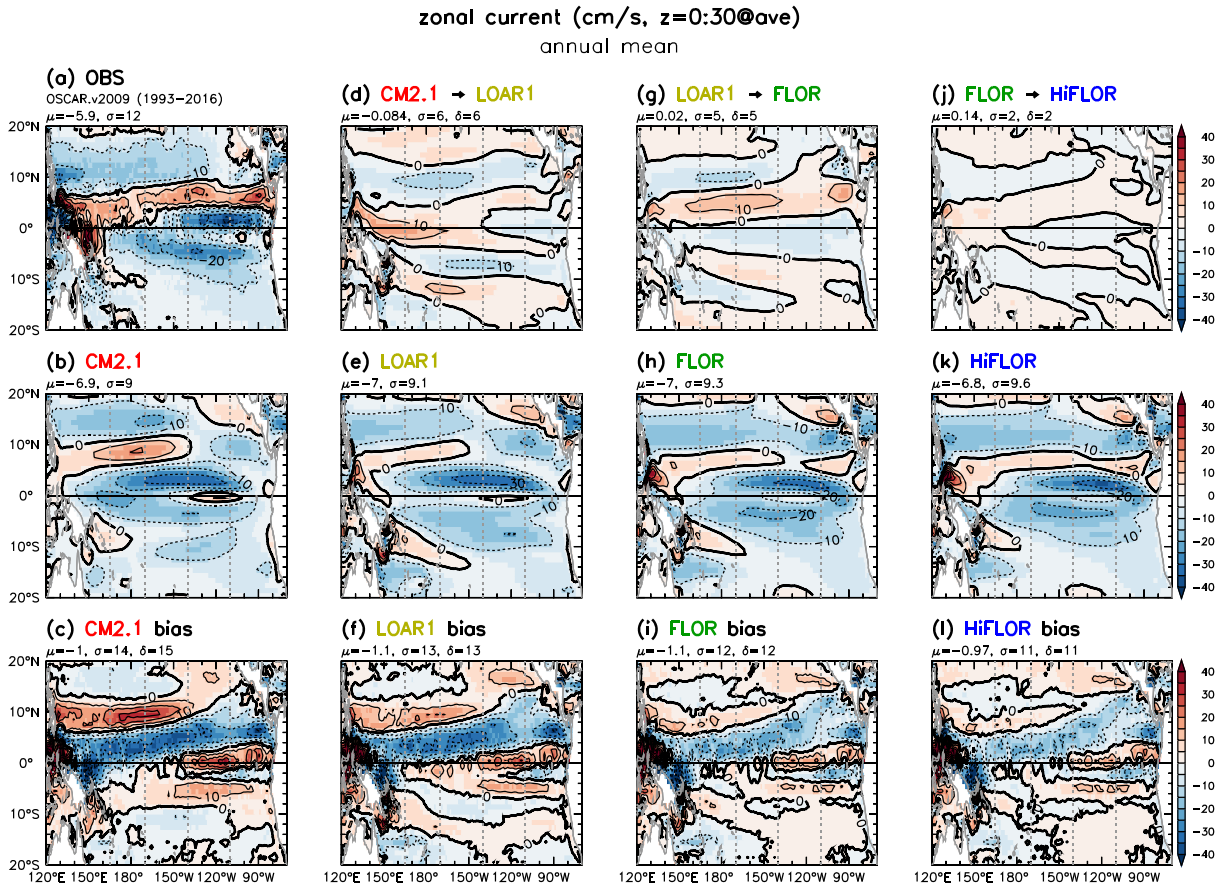

Figure 12. Observed and simulated tropical Pacific climatological annual-mean zonal current velocity averaged over the top 30 m of the ocean ($\overline{u}_{30}$, cm/s). (a) OSCAR observations, averaged 1993–2016. Middle row (b, e, h, and k) shows the model-simulated total fields, analogous to (a), averaged over years 1–100 of each control run. Bottom row (c, f, i, and l) shows each model's bias relative to (a). Dotted vertical lines correspond to the equatorial mooring longitudes in Figure 13. Otherwise as in Figure 1.

In the west/central Pacific, CM2.1's NECC and NEC penetrate only halfway across the basin, and their axes are shifted 2° north of their observed counterparts; both aspects are consistent with CM2.1's $\partial_y \overline{V}_S$ biases to the east of those regions. Along 5–8°N in the far east Pacific, CM2.1's insufficient $\partial_y \overline{V}_S$ actually yields *westward* currents, rather than eastward as observed for the NECC. This NECC bias dramatically reduces CM2.1's meridional shear ($\partial_y \overline{u}_{30}$) on the northern flank of the SEC, which may then contribute to CM2.1's weak TIW activity (Figure 18). CM2.1's weak $\partial_y \overline{V}_S$ in this region is mainly due to insufficient $\partial_y^2 \overline{\tau}^x > 0$ along 5–8°N, which is in turn due to the equatorward displacement of the east Pacific trade wind trough in CM2.1 (Figure 5). LOAR1's $\overline{u}_{30}$ biases are qualitatively similar to CM2.1's, though somewhat reduced.

The $\overline{u}_{30}$ is further improved in FLOR and HiFLOR, due to those models' more realistic $\overline{\tau}^x$ and $\partial_y^2 \overline{\tau}^x$ (Figure 5). The NECC remains too weak, but it at least now flows eastward in the east Pacific—which intensifies the $\partial_y \overline{u}_{30}$ between the SEC and NECC, and would be expected to boost TIW stirring north of the equator in FLOR relative to CM2.1 and LOAR1. Along the equator in the eastern Pacific, $\overline{u}_{30}$ is no longer slightly eastward, though the westward SEC remains too weak. The stronger equatorial westward $\overline{u}_{30}$ in FLOR and HiFLOR relative to LOAR1 (Figure 12g) is *not* due to stronger equatorial trade winds, which actually weaken relative to LOAR1 (Figures 5d, 5f, and 5h); rather, FLOR and HiFLOR's stronger westward $\overline{u}_{30}$ may instead be tied to their weaker EUC, as discussed next.

8.2. Equatorial Undercurrent

The EUC plays a key role in advecting west Pacific subsurface waters into the upwelling zones of the east Pacific, where they can more directly impact SST. The EUC also generates strong vertical shear ($\partial_z \overline{u}$) relative to the westward SEC at the surface, which helps to sustain vertical mixing above the thermocline (D. Wang &

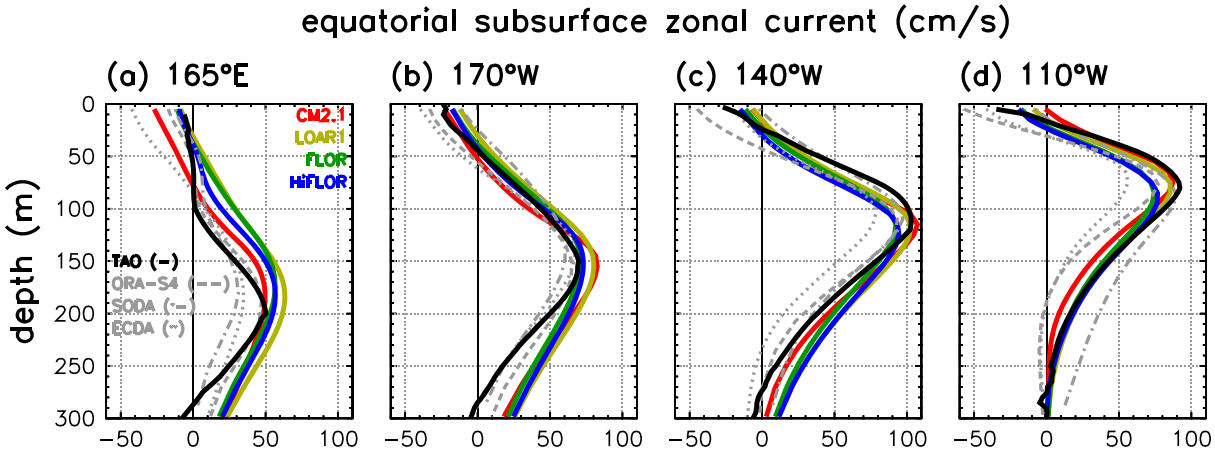

Figure 13. Subsurface zonal current velocity (cm/s) interpolated to four longitudes along the equator. Solid colored lines indicate time means over years 1–100 of the control simulations of CM2.1 (red), LOAR1 (yellow), FLOR (green), and HiFLOR (blue). Also shown are the time means from the TAO/TRITON moorings (black solid, 1980–2017), ORA-S4 reanalysis (gray dashed, 1979–2014), SODA.v3.4.1 reanalysis (gray dot-dashed, 1980–2015), and ECDA.v3.1 reanalysis (gray dotted, 1979-2017). TAO/TRITON buoy data are processed using daily means of measurements from both fixed-depth mechanical current meters and acoustic doppler current profilers, with a simple average of the two where both are available. The merged daily means from the buoys are vertically interpolated and then averaged onto a monthly grid; these monthlies are then used to compute a 12-month climatology, whose annual mean is plotted. The available years for the [mechanical current meter, acoustic doppler current profiler] buoy data are (a) [1985–2017, 1991–2008] at 165°E; (b) [2002–2017, 1988–2010] at 170°W; (c) [1983–2017, 1990–2010] at 140°W; and (d) [1980–2017, 1991–2010] at 110°W.

Müller, 2002). The meridional shear ($\partial_y \overline{u}$) between the EUC and SEC also helps to generate TIWs (Lyman et al., 2007; Willett et al., 2006).

Figure 13 shows upper-ocean profiles of the annual-mean zonal current ($\overline{u}$), interpolated to four key TAO/Triton moorings along the equator. The TAO observations show an eastward EUC sloping upward from 200 m at 165°E to 80 m at 110°W, with a peak speed of about 1 m/s near 140°W. The peak Eulerian-mean $\overline{u}$ on the equator has been estimated to be about 14 cm/s weaker than the peak speed within the meandering EUC core itself, since the narrow EUC meanders within a ±0.4° latitude band about the equator (Leslie et al., 2014).

It remains a challenge for model-based ocean reanalyses to capture the vertical structure of the equatorial currents. This is due to both the sparse observational constraints and a strong sensitivity of the simulated currents to the ocean model formulation and uncertain wind stress forcings. Figure 13 shows that relative to the mooring data, ORA-S4 has a westward bias in its equatorial currents, with a stronger SEC and weaker EUC. However, ORA-S4 does at least show realistic $\partial_z \overline{u}$ above the EUC. In contrast, SODA.v3.4.1 has weaker-than-observed $\partial_z \overline{u}$ both above and below the EUC, with a shallower zonal slope of the EUC and greater eastward transport in the east Pacific than ORA-S4, both above and below the EUC core.

CM2.1 produces quite realistic equatorial currents, outperforming even ORA-S4 and SODA.v.3.4.1 relative to the TAO data at most depths in the east Pacific. Compared to TAO, CM2.1 does show a shallower and stronger EUC in the western Pacific, with stronger $\partial_z \overline{u}$ above the EUC core.

LOAR1 shows improved surface westward currents, which are weaker at 165°E and stronger at 110°W than in CM2.1. At 110°W, LOAR1 matches the TAO data even better than the reanalyses. At the other equatorial moorings, LOAR1 does exacerbate some of CM2.1's EUC biases, strengthening the eastward EUC in the west (165°E) and vertically broadening it in the central Pacific (165°E–140°W).

Compared to LOAR1, the EUC and its zonal slope both weaken in FLOR and HiFLOR, consistent with their flatter equatorial thermocline (Figure 11e) and less divergent $\partial_y \overline{V}_S$ in the eastern equatorial Pacific (Figure 7e). The westward equatorial surface currents also intensify slightly relative to LOAR1 — perhaps due to weaker friction of the surface-intensified Ekman flow against the weaker EUC in FLOR and HiFLOR.

8.3. Equatorial Upwelling

Numerous studies have demonstrated the critical role of upwelling for the tropical Pacific climatology and its response to external radiative forcings (Clement et al., 1996; Dijkstra & Neelin, 1995; Predybaylo et al., 2017; Xie et al., 2010) and for mediating ocean-atmosphere feedbacks during ENSO (Capotondi et al., 2006; Collins et al., 2010; Kug et al., 2010; Neelin, 1991; Wang & An, 2002; Wittenberg, 2002; Zebiak & Cane, 1987). As yet there are

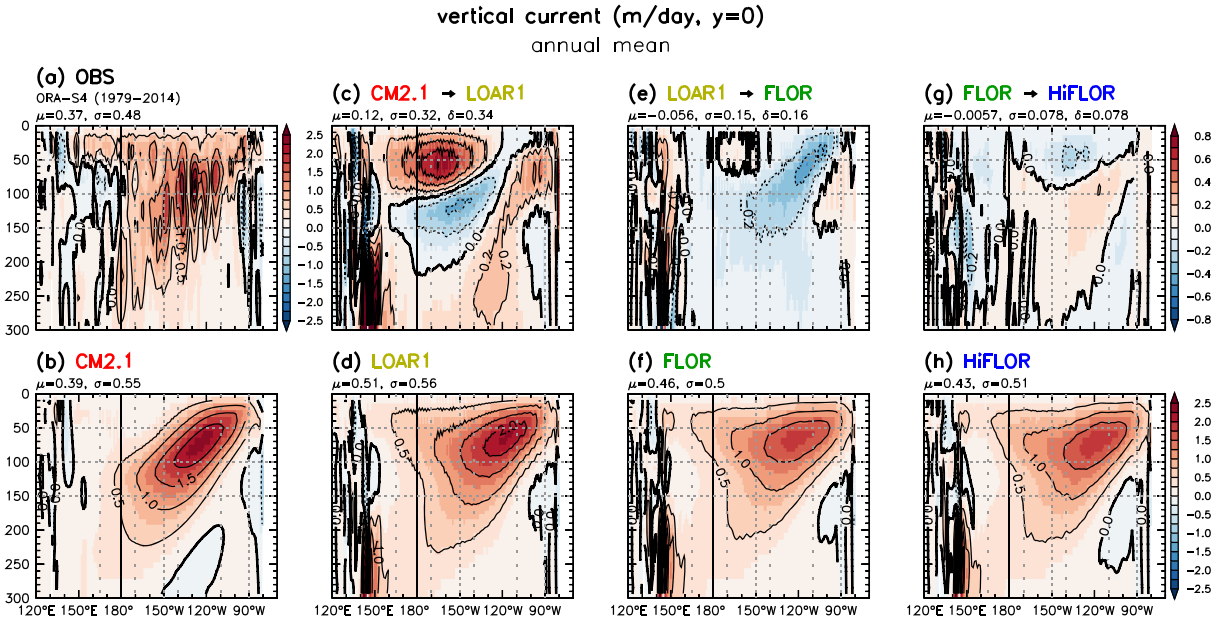

Figure 14. As in Figure 9 but for the subsurface vertical velocity (m/day, positive upward). (a) ORA-S4 reanalysis, averaged 1979–2014. Bottom row (b, d, f, and h) shows averages over years 1–100 of each control simulation. Remaining top panels (c, e, and g) as in Figure 9. The reliability of ORA-S4 for this field is unknown, since direct upwelling observations are not available.

no direct observations of this critical field, and so the modeling community must still rely on model reanalyses to help evaluate ocean simulations. Unfortunately, ORA-S4's biases in the zonal currents (Figure 13) lend little confidence in that product's ability to capture the real-world intensity and pattern of the annual-mean vertical velocity ($\overline{w}$). Yet we display ORA-S4's $\overline{w}$ here, if only to motivate future efforts to better constrain $\overline{w}$ via improved observations and reanalyses.

Figure 14 shows $\overline{w}$ interpolated to the equator. ORA-S4's equatorial $\overline{w}$ extends from the surface to the base of the thermocline. Not all of that $\overline{w}$ contributes to advective cooling of the layers above, since a large component of $\overline{w}$ arises simply from the vertical component of the EUC, which flows upward toward the east along the zonally tilted thermocline. ORA-S4 also has persistent localized peaks along the equator, which are likely artifacts created by assimilating sparse observations into a biased ocean model.

CM2.1 similarly has intense $\overline{w}$ at the equator—exceeding 2.25 m/day near 125°W at 75-m depth—that is stronger than the ORA-S4 values which spatially fluctuate about 1.5 m/day. Compared to ORA-S4, CM2.1 has much weaker $\overline{w}$ within the top 50 m of the western and central equatorial Pacific. CM2.1's peak $\overline{w}$ sits slightly above the thermocline and compared to ORA-S4 slopes more strongly upward toward the east and appears to be more linked to the tilted EUC. West of the dateline, CM2.1's $\overline{w}$ is generally stronger than in ORA-S4, consistent with CM2.1's stronger Ekman suction in the west (Figure 8).

Compared to CM2.1, LOAR1 develops a second, near-surface branch of $\overline{w}$ toward the west along 50 m, greatly broadening the vertical extent of $\overline{w}$ and better resembling ORA-S4. That LOAR1 has stronger $\overline{w}$ west of 130°W above 70 m, despite LOAR1's appropriately *weaker* implied $\overline{w}_E$ in the west Pacific (Figure 8), suggests that LOAR1's stronger density stratification in the west Pacific above 50 m (Figures 9c and I1c) may be helping to focus its Ekman transport into a shallower surface layer.

Compared to both CM2.1 and LOAR1, both FLOR and HiFLOR show a weaker peak equatorial $\overline{w}$ of just over 1.75 m/day near 120°W at 70-m depth. This is consistent with the weaker $\overline{w}_E$ inferred from the weaker equatorial trade winds in FLOR and HiFLOR, with relatively little change in density stratification above 70 m relative to LOAR1. The equatorial $\overline{w}$ is shifted slightly deeper in HiFLOR than FLOR, likely due to HiFLOR's slightly weaker thermal stratification above 70 m (Figure 9g).

9. Upper Ocean Heat Budget

Appendix E derives a simplified annual mean climatological heat budget relevant to a fixed-depth surface layer in the tropical Pacific ocean:

$$\frac{\overline{Q}_{sfc}}{\rho_0 C_p H_m} - \overline{\left[\nabla \cdot (\boldsymbol{u}_s T_s)\right]} + \overline{[R]} = 0, \tag{2}$$

where an overbar ($\overline{\ }$) denotes a climatological annual mean, square brackets ([ ]) denote a vertical average over the layer, Q_{sfc} is the net surface heat flux, ρ_0 is the seawater density, C_p is the seawater specific heat capacity, $H_m = 50$ m is a spatially and temporally constant mixed layer depth, $\boldsymbol{u}_s$ is the "slow" (monthly mean) component of the three-dimensional ocean velocity field, T_s is the slow temperature field, and R is a residual heating term. In short, the time-mean surface heat flux is balanced by time-mean *monthly advection* (namely, heating attributable to advection of monthly mean temperatures by the monthly mean currents), plus a residual heating associated with submonthly eddy advection, parameterized subgridscale oceanic mixing and stirring, and solar penetration. $\overline{Q}_{sfc}$ was displayed in Figure 4. The present section will discuss the remaining two terms of (2).

9.1. Monthly Scale Advection

Figure 15 shows the equatorial vertical structure of the monthly scale advective temperature tendency, $-\overline{\nabla \cdot (\boldsymbol{u}_s T_s)}$, namely, the time-mean heating that would arise from advection of the monthly mean temperature structure by the monthly mean currents. The ORA-S4 reanalysis shows strong cooling from this monthly advection in the eastern equatorial Pacific above 100 m, with the most intense cooling at 35 m east of 120°W, where the equatorial thermocline is shallow.

Given ORA-S4's strong localized peaks in $\overline{w}$ along the equator (Figure 14), the relative smoothness of ORA-S4's total monthly advective tendency is rather surprising. This smoothness stems from colocation of the peaks of $\overline{w}$ with the peaks of $\partial_x \overline{T}$ along the equator, associated with the subtle step-like features in the ORA-S4 thermocline (Figure 9a), so that the extrema in vertical advective cooling are offset by extrema in zonal advective warming.

In the central equatorial Pacific, CM2.1's monthly advective cooling is weaker near the surface than in ORA-S4, due to CM2.1's weaker SEC and $\partial_z \overline{T}$ (which weaken the westward and upward cold advection, respectively). CM2.1's cooling is more narrowly focused just above the thermocline, where $\overline{w}$ is stronger than in ORA-S4 (Figure 14b).

Compared to CM2.1, LOAR1's vertically broader $\overline{w}$ and stronger $\partial_z \overline{T}$ act to strengthen the equatorial monthly advective cooling and extend it closer to the surface, especially near the dateline. FLOR further shoals the advective cooling in the central equatorial Pacific but also reduces the cooling near the surface in the shallow-thermocline region east of 140°W, where $\overline{w}$ and $\partial_z \overline{T}$ both weaken in FLOR. HiFLOR slightly deepens the advective cooling, due to its deeper $\overline{w}$.

Figure 16 maps the horizontal structure of the upper-layer monthly advective tendency, $-\overline{\left[\nabla \cdot (\boldsymbol{u}_s T_s)\right]}$, which is the time-mean heating of the top 50 m of the ocean due to the monthly scale advective heat convergence. In ORA-S4, the monthly advective cooling extends across nearly the entire basin between 6°S and 4°N and is strongest between 2°S and 2°N east of 140°W. There is strong monthly advective cooling near the South American coast, due to southerly winds which induce offshore Ekman flow and coastal upwelling. There is also strong cooling near the Guatemala basin, associated with $\overline{w}$ and mixing driven by the narrow wind jets that flow through the Tehuantepec, Papagayo, and Panama gaps in the Central American cordillera (Alexander et al., 2012).

In contrast, CM2.1 has a more horseshoe-shaped pattern of cooling, with weaker monthly advective cooling in the top 50 m between 2°S and 2°N and 180° and 110°W and stronger monthly advetive cooling near South America and along 8°S and 6°N (Figure 16b). CM2.1 also shows much less cooling west of Costa Rica and Panama, likely caused by the inability of CM2.1's 220 km atmosphere grid to represent the narrow gap winds and their associated Ekman upwelling (Figure 8b).

LOAR1 shows minor improvements, with slightly more cooling than CM2.1 in the eastern equatorial Pacific, and less of a horseshoe pattern. FLOR and HiFLOR show further improvements, with their weaker equatorial trade winds (Figure 5) and flatter thermocline (Figure 9) slightly weakening their excessive near-surface

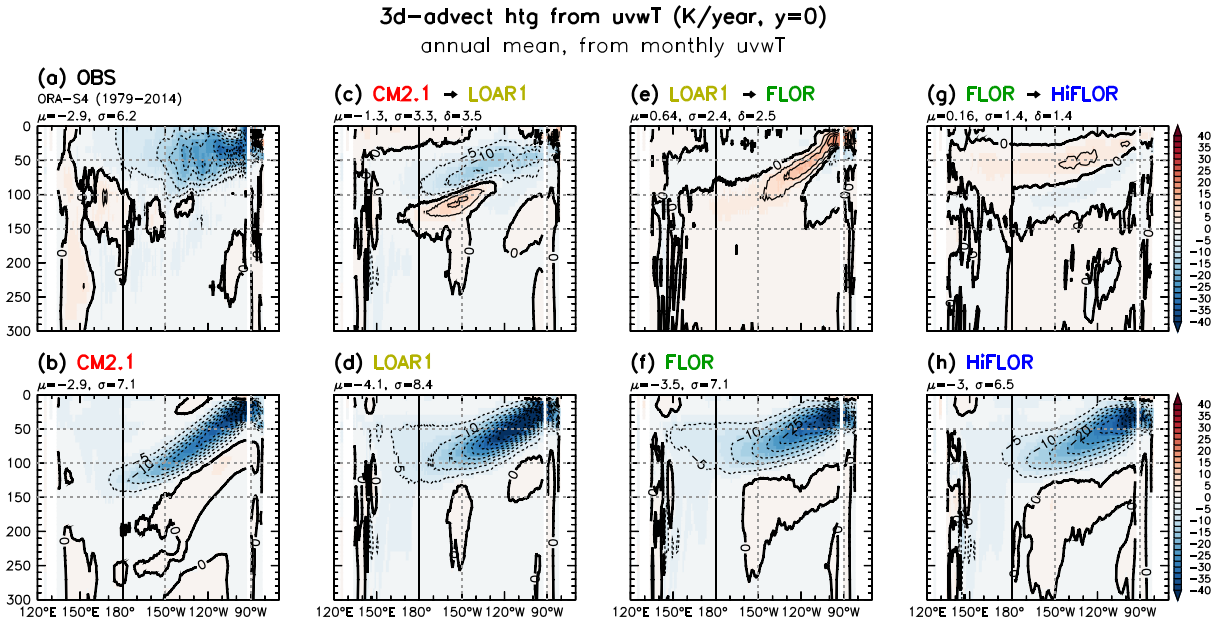

Figure 15. As in Figure 14 but for the total monthly advective heating (K/year), which is diagnosed pointwise from the monthly mean currents and temperature gradients, then interpolated to the equator, then time-averaged over the full data set.

$\partial_z \overline{T}$ and monthly advective cooling near South America. The higher-resolution atmosphere and topography (and stronger gap winds) in FLOR and HiFLOR also improve their subsurface advective cooling near Central America.

9.2. Residual Heating

Figure 17 shows $[\overline{R}]$ from equation (2), namely, the time-mean residual heating required to balance the surface heat flux and monthly advection, averaged over the top 50 m of the ocean. For the models, $[\overline{R}]$ estimates the

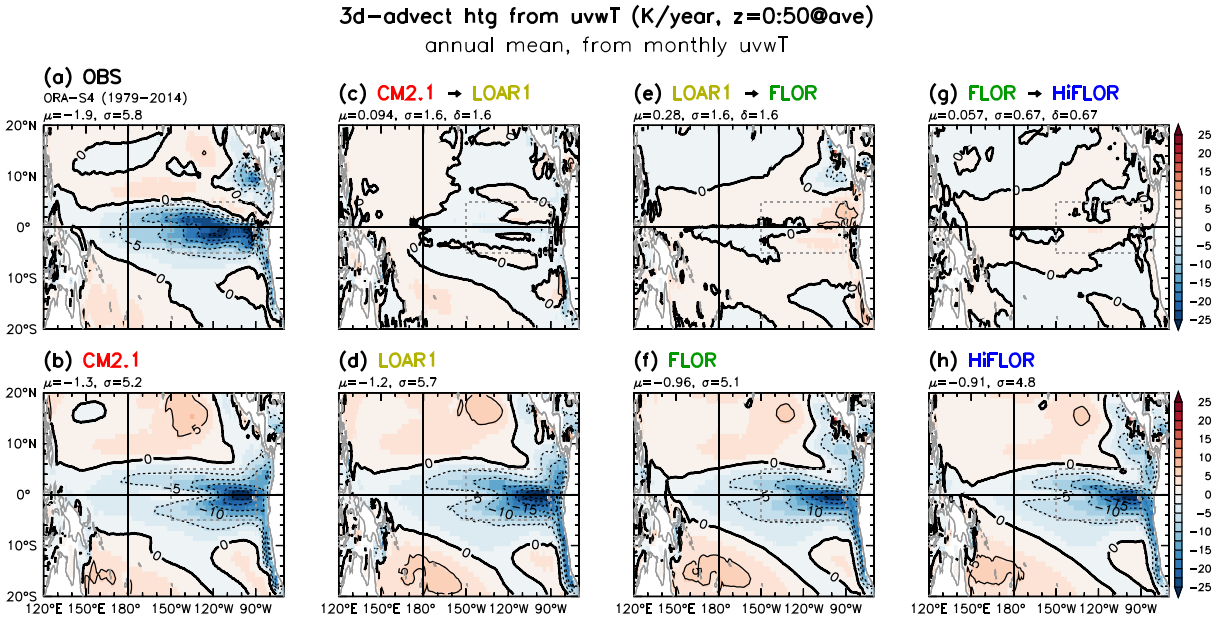

Figure 16. As in Figure 1 but for the total monthly advective heating (K/year), which is diagnosed pointwise from the monthly mean currents and temperature gradients, then averaged over the top 50 m of the ocean, then time-averaged over the full data set. (a) ORA-S4 reanalysis, averaged 1979–2014. Bottom row (b, d, f, and h) shows averages over years 1–100 of each control simulation. Biases relative to (a) are not shown, since the ORA-S4 solution for this field is of unknown quality.

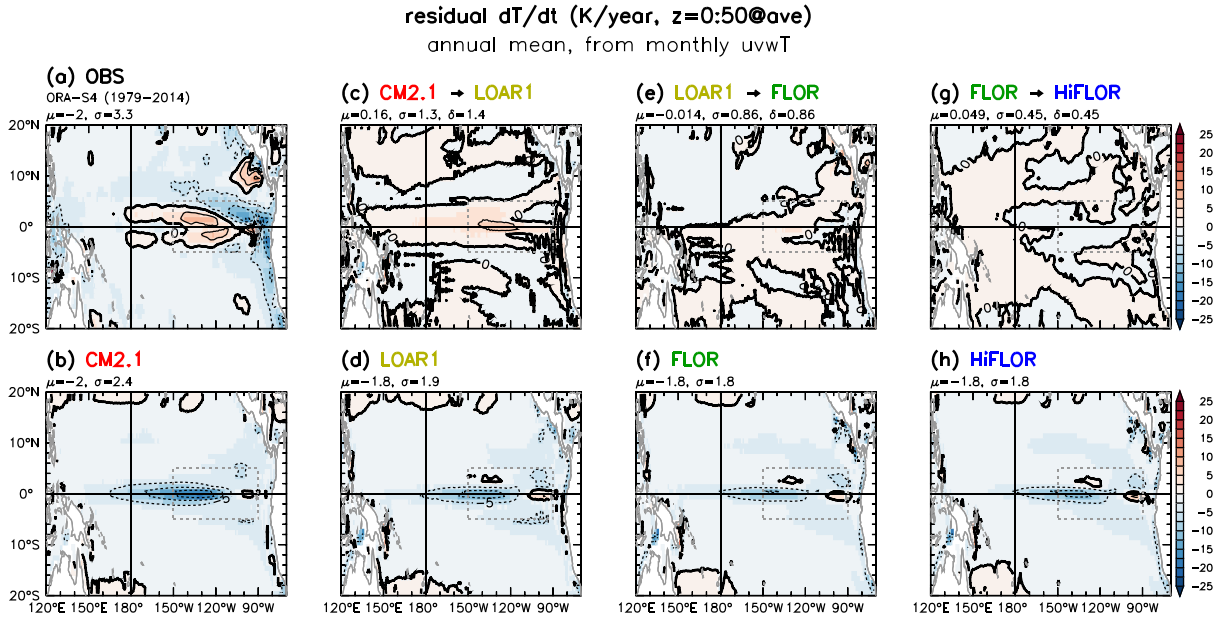

Figure 17. As in Figure 16 but for $\overline{[R]}$ (K/year), the inferred residual heating averaged over the top 50 m of the ocean and then time-averaged over the full data set. For each month, R is computed pointwise by subtracting the monthly advective heating (Figure 16) and surface flux heating (Figure 4) from the total temperature tendency ($\partial_t T$). In the model simulations, R in the tropical Pacific is almost entirely due to submonthly advection and parameterized vertical diffusion. In the ORA-S4 reanalysis, R further includes the assimilation increments that nudge the ocean solution toward observations and stand in for real-world forcings and physical processes that are missing from the assimilating ocean model. Because there is very little long-term temperature trend $\overline{\partial_t T}$, the sum of Figures 4, 16, and this figure essentially vanish within the tropical Pacific upper ocean.

heating due mainly to submonthly advection and vertical mixing. For ORA-S4, $\overline{[R]}$ also includes any time-mean heating due to assimilation increments, which nudge the ocean model toward the observations and thereby compensate for unresolved ocean processes and/or errors in the surface forcings (see Appendix E).

In ORA-S4, $\overline{[R]}$ is a cooling term over most of the tropical Pacific, with the strongest cooling near the eastern and western boundaries and along 8°N and 6°S. $\overline{[R]}$ is a warming term in the central Pacific along 2°N and 2°S, due in part to submonthly TIWs which stir warm water equatorward. $\overline{[R]}$ is also a warming term in the *gap winds* region southwest of Central America, helping the surface heat flux to counter ORA-S4's strong monthly advective cooling in this region (Figure 16a).

The $\overline{[R]}$ simulated in the models differs greatly from that in ORA-S4. CM2.1's $\overline{[R]}$ shows cooling nearly everywhere, especially in the central equatorial Pacific where $\overline{[R]}$ is a heating term in ORA-S4. CM2.1's $\overline{[R]}$ also shows relatively little residual cooling along the coast of South America, in contrast to ORA-S4. Compared to CM2.1, the LOAR1, FLOR, and HiFLOR simulations show slightly less residual cooling from $\overline{[R]}$ along the equator and more cooling along the South American coast; yet all still look very different from ORA-S4.

The similarity of the residual patterns among the GFDL simulations (Figures 17b, 17d, 17f, and 17h) and their differences from ORA-S4 suggest that any bias in their submonthly processes must be common to all of them. Biases could plausibly arise from the ocean models' relatively coarse (1°) resolution in the zonal direction, which may suppress the TIWs, coastal eddies, and their effects on the heat transports and vertical exchange. If so, then apparently, the models compensate not with surface heat flux biases (which according to Figure 4 are relatively minor) but rather with stronger monthly advective cooling near the eastern boundary (where $\partial_z \overline{T}$ is too strong) and weaker monthly advective cooling in the top 50 m of the cold tongue (due to weaker $\overline{w}$, weaker westward $\overline{u}$, and/or weaker $\partial_z \overline{T}$ above 50-m depth). Alternatively, the analysis increments that contribute to ORA-S4's $\overline{[R]}$ may not solely represent corrections to submonthly processes; the increments could also be responding to biases in ORA-S4's surface fluxes and/or monthly advection, which would then make the ORA-S4 residual a less appropriate target for the models' submonthly residuals.

If ORA-S4's $\overline{[R]}$ were taken at face value and interpreted as a term arising from submonthly processes, then the models' stronger residual cooling near the equator would suggest that the models either underestimate a warming effect or overestimate a cooling effect of submonthly variability in these regions. One contributor

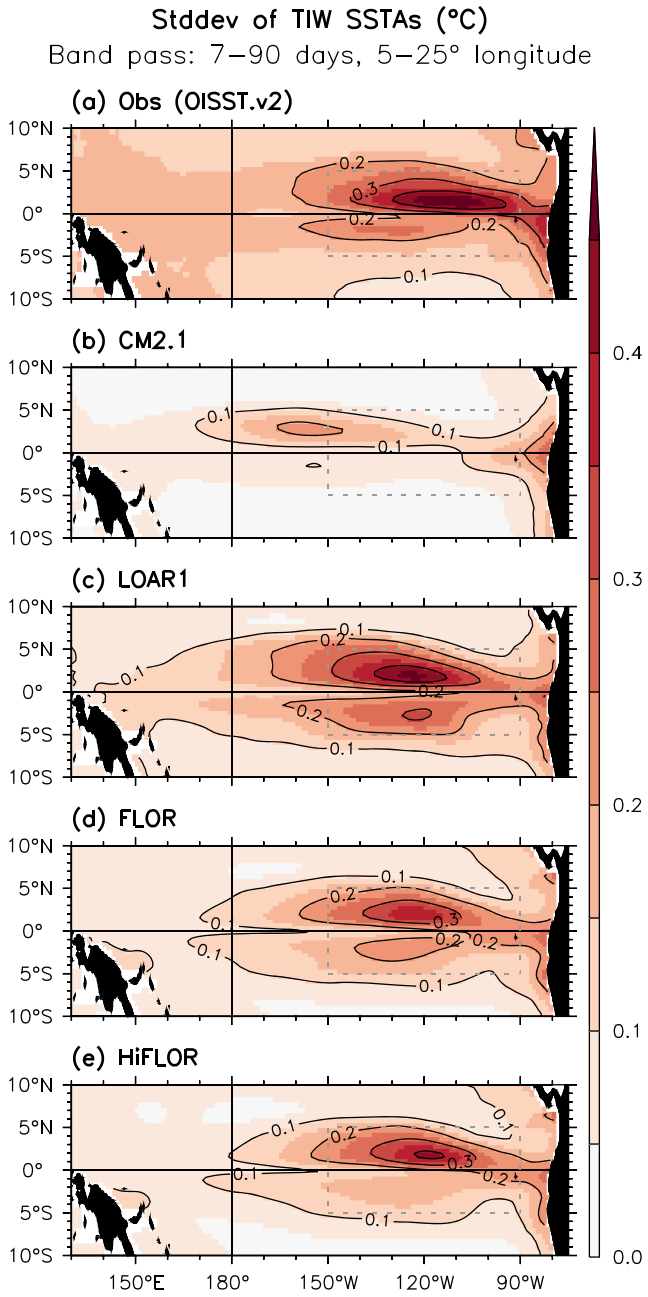

Figure 18. Temporal standard deviation of zonally narrow subseasonal sea surface temperature (SST) anomalies (°C), driven mainly by tropical instability waves (TIWs). (a) Observations from OISST.hi.v2 (1982–2016); (b) CM2.1 1860 control run (years 101–200); (c) LOAR1 1990 control run (years 1–100); (d) FLOR 1990 control run (years 701-800); and (e) HiFLOR 1990 control run (years 1–100). Each data set's daily-mean SSTs are averaged onto the FLOR ocean grid and then band-passed with triangle smoothers to retain periods of 7–90 days, zonal wavelengths of 5–25° longitude, and meridional wavelengths exceeding 2° latitude. The result is squared, then smoothed to retain zonal wavelengths greater than 11°, and finally time-averaged to produce a variance whose square root is plotted. Gray dashes mark the Niño-3 region.

could be the models' weaker-than-observed TIWs (section 10), which could reduce both the equatorward heat convergence in the upper ocean, and the ocean's heat uptake from the atmosphere along 2°N and 2°S due to insufficient poleward spreading of the cold tongue (Jochum & Murtugudde, 2006). Alternatively, the models might inadvertently have been tuned toward excessive vertical diffusive cooling within the equatorial cold tongue, to compensate for insufficient monthly advective cooling near the surface (Figure 16) and excessive influx of heat from the atmosphere (Figure 4). The opposite situation holds near the coast of South America, where the models show much *less* residual cooling than ORA-S4. This weaker east Pacific submonthly cooling in the models—which helps compensate for their stronger monthly advective cooling in the far east Pacific (Figures 16b, 16d, and 16f)—could conceivably stem from insufficient simulated high-frequency upwelling and vertical mixing in the east Pacific, associated with the models' overly strong thermal stratification there.

10. Tropical Instability Wave Activity

To understand the differences in residual heating seen in section 9.2, we next examine the TIW activity in the observations and simulations. As mentioned above, TIWs stir warm surface water equatorward to help maintain the thermal stratification of the cold tongue, while also stirring cold equatorial water poleward to meridionally broaden the cold tongue SST. The TIWs also produce small-scale transient shears which enhance vertical mixing, further cooling the near-equatorial SST and enhancing the cold tongue's heat uptake from the atmosphere.

Figure 18 shows the amplitude of observed and simulated TIW SSTAs, with zonal and temporal filtering to help isolate the subseasonal variability associated with TIWs from that associated with equatorial Kelvin waves excited by westerly wind events in the western/central Pacific. The observed TIW SSTAs (Figure 18a) are strongest north of the equator and in the Niño-3 region, peaking near 110°W, 3°N where there is both strong $\partial_y \overline{u}$ to amplify the waves and strong $\partial_y \overline{T}$ to boost their meridional heat transports.

In CM2.1, the TIW SSTAs are much weaker and farther west than observed, peaking near 155°W, 3°N. CM2.1's TIW SSTAs are weak despite the model's excessive climatological cold tongue (Figure 1), which enhances the poleward $\partial_y \overline{T}$ and thus the meridional advective heat flux for a given meridional current anomaly; thus, the stirring by TIW currents in CM2.1 is likely even weaker than suggested by the model's weak SSTAs in Figure 18.

LOAR1's TIW SSTAs, which peak near 125°W, are much stronger and more realistic than in CM2.1. LOAR1's improved TIW SSTAs are particularly impressive given that LOAR1 also has an improved (weaker) climatological cold tongue, which on its own would tend to weaken the TIW advection due to weaker $\partial_y \overline{T}$. LOAR1's improved TIWs are likely due to both its improved $\boldsymbol{\tau}$ and $\partial_y \overline{u}$ in the east Pacific (Figures 5 and 12) and its improved ocean physics and numerics—in particular its biharmonic viscosity scheme (which weakens the frictional dissipation at and above the spatial scale of the TIWs) and its less dissipative advection scheme. LOAR1 does produce more TIW activity south of the equator than observed, perhaps due to LOAR1's excessive shear between the EUC and SEC south of the equator (Figure 12).

FLOR and HiFLOR retain LOAR1's improved spatial pattern of TIW SSTA variability—but interestingly, these simulations' TIW SSTAs *weaken* relative to LOAR1, despite FLOR and HiFLOR having an identical ocean formulation and a *stronger* $\partial_y \overline{u}$ in the northeast Pacific near the equator. The weaker TIW SSTAs in FLOR and HiFLOR may be due to those models' improved (weaker) $\partial_y \overline{T}$ near the equator (Figure 1), which would weaken the TIW advective fluxes in the off-equatorial central and eastern Pacific.

The weaker-than-observed TIW activity in all four models is likely associated with the relatively coarse resolution of their common ocean grid, which is 1° × 1° narrowing to 0.33° meridional spacing near the equator. Marchesiello et al. (2011) suggest that a 10-km grid is needed to adequately capture TIW dynamics near the equator, and indeed, the TIWs are much stronger in the GFDL-CM2.6 model which has the same atmosphere as FLOR but uses a 10-km ocean grid in the tropics (Delworth et al., 2012; Griffies et al., 2015). This suggests that FLOR's coarse oceanic horizontal (especially zonal) resolution is a key limiting factor for its simulation of TIWs and their role in the heat budget of the equatorial Pacific.

11. Discussion

11.1. Remaining Challenges

Compared to CM2.1, the LOAR1, FLOR, and HiFLOR models yield progressively more realistic simulations of tropical Pacific annual-mean climate. The atmospheric grid refinement from LOAR1 to FLOR (208 → 55 km)

generally has more of an impact on the simulated tropical Pacific climatology than the subsequent refinement from FLOR to HiFLOR (55 → 26 km). This is in contrast to the simulations of small-scale and regional phenomena (tropical storms, seasonal snowpack, and regional climate extremes) that continue to show striking improvements from FLOR to HiFLOR (Kapnick et al., 2018; Murakami et al., 2015; van der Wiel et al., 2016). This suggests that while simulations of these regional phenomena (and their dependence on tropical Pacific climate) might continue to benefit from further increases in atmospheric resolution, the simulation of the tropical Pacific climatology itself may benefit more from improved parameterizations of subgridscale atmospheric processes (e.g., convection and clouds) and improved ocean models. It is conceivable that some of the tropical Pacific climate improvements seen in the 55-km FLOR could also have been attained with a 100-km grid (midway between LOAR1 and FLOR), though we have not tested this in the FLOR lineage which has focused on improving simulations of regional and extreme phenomena that clearly benefit from higher atmospheric resolution. However, analyses of the 100-km GFDL-AM4 atmosphere model (Zhao et al., 2018a; 2018b) and its coupled counterpart GFDL-Coupled Model version 4 confirm that excellent simulations of tropical Pacific climate are indeed possible with a 100-km atmosphere grid.

Several challenges remain. All four simulations (CM2.1, LOAR1, FLOR, and HiFLOR) have overly shallow thermoclines between 20°S and 5°N, with prominent zonal-mean cold biases between 50- and 250-m depth, and too little meridional asymmetry of the thermocline about the equator. All four simulations also have excessive off-equatorial trade winds, which leads to excessive wind stress cyclonicity and poleward Sverdrup transport near the equator.

Some of the changes from CM2.1 → LOAR1 → FLOR → HiFLOR are *not* improvements. In particular, LOAR1's change in tropical Pacific wind stress boosts the off-equatorial trade winds and evaporative cooling near the dateline between 10° and 20°S, which worsens the cold SST bias there compared to CM2.1. LOAR1's wind changes also exacerbate the wind stress cyclonicity south of the equator—leading to stronger $\overline{w}_E$ in that region and more poleward Sverdrup transport away from the equator. LOAR1's stronger wind-driven circulation then cools the source waters of the EUC, helping to shoal the equatorial thermocline and boost the subsurface monthly advective cooling at the equator, despite LOAR1's *weaker* equatorial $\overline{w}_E$. This remotely driven wind stress effect is sufficiently strong that the eastern equatorial Pacific cold SST bias and excessive ocean heat uptake remain present in LOAR1 despite its much improved (weaker) equatorial trade winds. LOAR1's excessive off-equatorial cyclonicity may well be masking an inherent tendency of the ocean component to overdeepen the equatorial thermocline.

Relative to LOAR1, FLOR further strengthens the trade winds and evaporation in the southwest tropical Pacific, worsening the cold SST bias there relative to LOAR1. FLOR also shows greater intercentennial warm drift of tropical Pacific temperatures below 100 m, reflecting stronger heat uptake outside the tropics. On the bright side, FLOR's reduced rainfall, wind stress cyclonicity, and subsurface cold bias south of the equator produce a warmer and saltier EUC, which (together with FLOR's weaker equatorial trade winds) leads to very realistic equatorial thermal stratification within the top 50 m of ocean in FLOR. This practically eliminates the equatorial cold SST bias in FLOR and improves (weakens) FLOR's equatorial oceanic heat uptake.

FLOR's still-excessive wind stress cyclonicity may yet be masking an intrinsic tendency of its ocean component to overdeepen the equatorial thermocline. This is suggested by HiFLOR's overly deep isothermal layer depth (ILD), discussed in Appendix H, which indicates that more realistic winds cause the ocean component to generate excessive vertical mixing near the surface.

11.2. A Path Forward

Future progress toward simulating tropical Pacific climate depends on better observing, simulating, and understanding its multiscale coupled interactions. Atmospheric GCMs intended for coupling must be assessed for their ability to produce realistic tropical Pacific patterns of *time-mean surface fluxes*—in particular the surface wind stress and the net surface heat flux. Surface flux biases may hardly affect an AGCM forced by observed SSTs, but in coupled mode, those flux biases can affect SST, strongly feeding back onto the atmospheric simulation. Similarly, ocean GCMs intended for coupling must be assessed for their ability to produce realistic equatorial near-surface *thermal stratification*, *heat budget tendencies*, and *heat uptake* from the atmosphere. These near-surface features may be tightly constrained in flux-forced ocean GCM (OGCM) runs (e.g., Coordinated Ocean-ice Reference Experiments; Griffies et al., 2009), but in coupled mode, a model's upper-ocean dynamical biases can alter the SST and thus the atmospheric simulation of surface wind stress, heat fluxes, and rainfall, feeding back onto the OGCM and biasing its water mass formation and transports.

To guide future model development, more precise, accurate, representative, and reliable tropical Pacific constraints are needed from observations and reanalyses. Better constraints are particularly needed for the annual-mean wind stress and its curl, the net surface heat flux and its components, time-mean rainfall and the atmospheric moisture budget, subsurface currents, upwelling, mixing, and the upper-ocean heat budget. Improved model-based reanalyses are critical, as are enhancements to the Tropical Pacific Observing System (TPOS) as proposed by the international TPOS2020 Project (Cravatte et al., 2016).

The results of this study highlight the role of nonlocal air-sea feedbacks in the equatorial Pacific climatology, namely, the influence of off-equatorial surface heat and momentum fluxes on the equatorial cold tongue intensity and thermocline depth. Nonlocal controls on cold tongue intensity have been proposed by several previous studies, involving subtropical cloud albedos (Burls et al., 2017), the depth of off-equatorial mixing and solar penetration (Anderson et al., 2009), equatorward subsurface advection of temperature biases subducted in the eastern subtropical Pacific (Thomas & Fedorov, 2017), SSTs in the tropical Indian and Atlantic Oceans (Katjar et al., 2017), and the Indonesian Throughflow (Song et al., 2007). Our study adds the time-mean off-equatorial wind stress curl and its implied Ekman and Sverdrup transports as key remote influences on equatorial Pacific climate. This in turn implies that the off-equatorial wind stress curl and the many factors that contribute directly and indirectly to it (e.g., the SST, net surface heat flux, rainfall, clouds, atmospheric latent heating and convective momentum transports, and vertical mixing within the oceanic and atmospheric boundary layers) will need to be better constrained by observations, to provide reliable targets for model developers.

We would thus encourage investigators to apply the following dynamically motivated diagnostics, both to intercompare observational and reanalysis products and to help attribute biases in coupled simulations:

1. The time-mean net surface heat flux (ocean heat uptake), as a proxy for the time-mean intensity of local ODC arising from advection, stirring, and mixing.
2. The surface wind stress cyclonicity cycl($\boldsymbol{\tau}$), and its implied Ekman suction $\overline{w}_E$ and Sverdrup transport meridional divergence $\partial_y \overline{V}_S$, to diagnose wind-induced biases in the equatorial thermocline depth and the upper-ocean currents and heat transports.
3. The upper-ocean stratification and heat budget, to attribute ocean temperature biases to particular deficiencies in simulated surface fluxes, currents, temperature gradients, and submonthly processes.

12. Summary

Realistic simulations of the tropical Pacific climatology are needed to support reliable predictions and future projections of ENSO and its effects on global climate. This study documents improved simulations of the annual-mean tropical Pacific climatology in two global CGCMs recently developed at GFDL. Relative to their predecessor model CM2.1, FLOR and HiFLOR introduce a more sophisticated ocean model—with a more scale-selective viscosity scheme, a less dissipative advection scheme, and improved parameterizations of mesoscale and submesoscale eddies—plus refinement of the atmospheric horizontal grid and land topography by a factor of 4 (FLOR) or 8 (HiFLOR). These models are being used extensively for climate research, with CM2.1 and FLOR also contributing global seasonal predictions to the NMME each month. A fourth model, LOAR1, was used to isolate the roles of improved ocean/atmosphere parameterizations (CM2.1 → LOAR1) versus atmospheric grid refinement (LOAR1 → FLOR → HiFLOR) in improving the tropical Pacific simulation.

The improved ocean/atmosphere parameterizations (CM2.1 → LOAR1) warm and improve the simulated time-mean central equatorial Pacific SST, producing a beneficial (roughly El Niño-like) change that includes eastward and equatorward shifts of the atmospheric convection, rainfall, and fresh surface pool in the western/central tropical Pacific; weaker trade winds and Ekman upwelling ($\overline{w}_E$) in the western equatorial Pacific; weaker evaporation off-equator; improved surface currents; a shallower and flatter equatorial thermocline; an oceanic mixed layer that is shallower in the western/central equatorial Pacific (and deeper in the rest of the tropical Pacific); and reduced intercentennial warm drift within the top 300 m of the ocean.

Compared to CM2.1, LOAR1's enhanced east/central Pacific TIW activity, shallower thermocline, and intensified west Pacific fresh pool all contribute to a more stratified upper ocean near the equator. This weakens the upper-ocean vertical mixing, contributing to LOAR1's warmer SST and shallower upwelling and advective cooling along the equator. LOAR1 also has weaker implied $\overline{w}_E$ in the central equatorial Pacific, which helps to warm the local SST. The warmer equatorial SST in turn induces more cloud shading in the west and

more evaporation in the east, which improves (weakens) the net ocean heat uptake near the equator. LOAR1's warmer equatorial SST also enhances the southeast tropical Pacific meridional SST gradient—boosting the southeasterly trade winds and weakening their convergence into the southeastern ITCZ and strengthening the southerly winds, upwelling, evaporative and subsurface advective cooling, and cloud shading along the South American coast.

Most of these features further improve with progressive refinement of the atmospheric grid (LOAR1 → FLOR → HiFLOR). In addition, the atmospheric refinement improves the simulated SST gradients, surface wind stresses, implied Ekman and Sverdrup transports, subsurface temperature and salinity structure, and upper-ocean heat budget. FLOR has practically eliminated the cold SST bias along the equator, which is remarkable for a global CGCM without any flux adjustments. FLOR's warmer equatorial SST is due to both weaker *off-equatorial* trade winds (which weaken the poleward Sverdrup transport and thereby deepen the equatorial thermocline) and weaker *equatorial* trade winds (which weaken the equatorial $\overline{w}_E$ and may arise partly from coupled Bjerknes feedbacks involving the weakened zonal gradient of SST). These wind changes improve (weaken) the monthly scale advective cooling in the eastern equatorial Pacific, which is then compensated locally by intensified evaporative cooling due to stronger cross-equatorial southerly winds. FLOR's and HiFLOR's equatorward-shifted ITCZ and improved wind stresses also lead to enhanced meridional shear of the zonal surface currents north of the equator, which in turn enhances the meridional asymmetry of the simulated TIW activity. These results highlight the critical role of tropical Pacific wind patterns (and their response to atmospheric model resolution) in governing the oceanic currents and eddies.

The improved tropical Pacific climate simulations of FLOR and HiFLOR are already contributing to improved ENSO forecast performance (Barnston et al., 2017; Jia et al., 2015) and progress in simulating and forecasting ENSO and its global impacts (Choi et al., 2015; Delworth et al., 2015; Krishnamurthy et al., 2015, 2016; Murakami, Vecchi, Delworth, et al., 2017; Vecchi et al., 2014; Yang et al., 2015). Ray et al. (2018a, 2018b) provide further analyses of the climatological upper-ocean heat budget of FLOR, as well as of a version called FLOR Flux-Adjusted (FLOR-FA) in which surface flux adjustments are used to correct the climatological SST and wind stress. The improved simulations of tropical Pacific climate variability—including the seasonal cycle and ENSO—in FLOR, HiFLOR, and FLOR-FA will be described in a future study.

Appendix A: Model Initialization, Forcings, and Equilibration

Each CGCM in this study is initialized from present-day ocean conditions at year 1 as described in Delworth et al. (2006) and then integrated forward in time subject to 1990 values of trace gases, insolation, aerosols, and land cover. No flux adjustments are used.

In all of the control simulations, the tropical Pacific upper ocean gradually warms during the first 300 years, as it equilibrates to the prescribed 1990 radiative forcings and to model biases in the patterns of surface heat fluxes, ocean heat uptake, and heat transports. Figure A1 summarizes this warming, in terms of the change in centennial-mean zonal-mean temperature across the tropical Pacific from the first century (years 1–100) to the third (years 201–300).

In all cases the near-surface thermal stratification, $SST - T_{z=100m}$, changes by less than 0.1 °C. At the equator, CM2.1 warms by over 0.3 °C, both above 75 m and below 200 m. CM2.1 warms by 0.1–0.2 °C south of the equator and above 150 m and 0.4–0.6 °C below 200 m and between 10° and 15°N. In contrast, LOAR1 warms less than 0.2 °C above 200 m. FLOR warms less than CM2.1 near the surface, but more than LOAR1 at all depths, especially below 150 m. On the equator, FLOR warms by over 0.4 °C below 200 m and by over 0.7 °C below 300 m. HiFLOR shows slightly less warming than FLOR, though with a similar pattern.

Figure A2 shows the horizontal structure of this warming, averaged over the top 300 m of the ocean. In CM2.1, the warming is strongest in the central Pacific, with the peak warming between 180° and 150°W north of the equator. In LOAR1, the warm drift is much weaker; within 10° of the equator LOAR1's warming generally does not exceed 0.4 °C. The stronger warming of FLOR and HiFLOR peaks in the western/central Pacific between 10° and 15°N and generally does not exceed 0.8 °C.

Because FLOR and HiFLOR are designed mainly for seasonal-to-decadal forecasting, it is most relevant to evaluate them within the context of present-day climate—for example, using the well-observed period of the past 30–40 years. This study thus focuses on years 1–100 of each simulation, short enough to minimize the

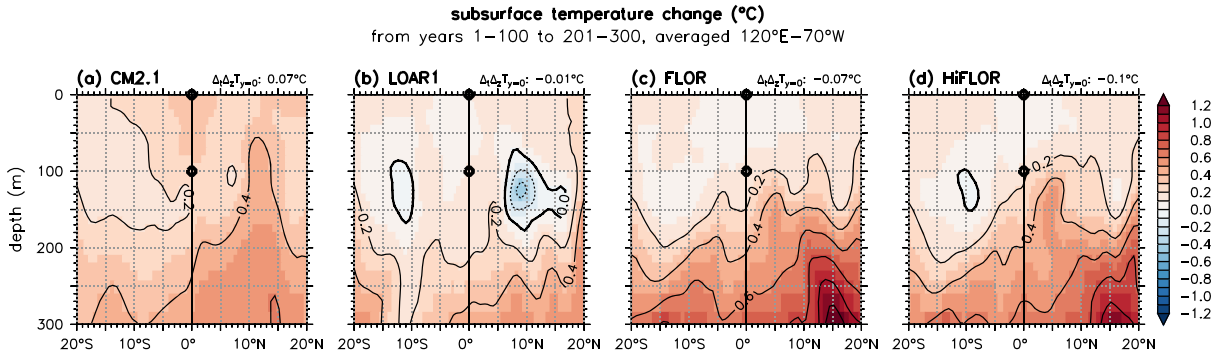

Figure A1. Intercentennial change in subsurface temperature (°C), for control simulations with year-1990 forcings, averaged zonally across the tropical Pacific ocean (120°E–70°W): (a) CM2.1, (b) LOAR1, (c) FLOR, and (d) HiFLOR. For each panel, the label at top right indicates the temporal change in equatorial Pacific zonal-mean stratification, that is, the vertical difference between the two black circles; this is the zonal mean of $\Delta_t \Delta_z T$ at the equator, where $\Delta_z T = \mathrm{SST} - T_{z=100}$ is the upper-ocean thermal stratification, and Δ_t is the change in centennial mean between the first and third centuries of simulation.

accrued commitment warming and model drift shown in Figures A1 and A2 but long enough to robustly characterize the climatological annual mean.

Appendix B: Model Intercomparison and Evaluation Methods

The observational and model data sets exist on different spatial grids. To compare them over the tropical Pacific ocean, we process each data set as follows.

On each data set's native longitude-latitude-depth-time ($\{x, y, z, t\}$) grid, any cells that are more than 50% occupied by land, either in the data set or in the real world, are masked out. The desired spatial transformation (e.g., interpolating to the equator, averaging zonally across the basin, or determining the depth of the isothermal layer) is then applied, to extract a lower-dimensional field from the data set. These spatial transformations are performed on the model's native grid, to leverage the full resolution of the input data. This is especially important when dealing with meridionally narrow climatological features near the equator, such as the EUC.

To compare fields of temporal statistics (e.g., means, variances, or regressions) which may be nonlinear functions of the source data, it is important to ensure that these statistics will summarize the same range of scales in both data sets. To that end, we generally use monthly and longer-term means to help attenuate temporal variance at spatial scales near the grid scale. In addition, prior to computing any temporal statistics, we further place all data sets onto a standard $\{x, y, z\}$ spatial *comparison grid*, as follows.

After the native-grid land masking and spatial transformation, each data set is regridded to a standard horizontal $\{x, y\}$ grid, consisting of uniformly spaced 1° × 1° cells spanning 0–360°E, 90°S to 90°N. The centers of these cells lie midway between the cell edges, so that the southwesternmost cell has its southwestern corner at (0°E, 90°S) and is centered at (0.5°E, 89.5°S).

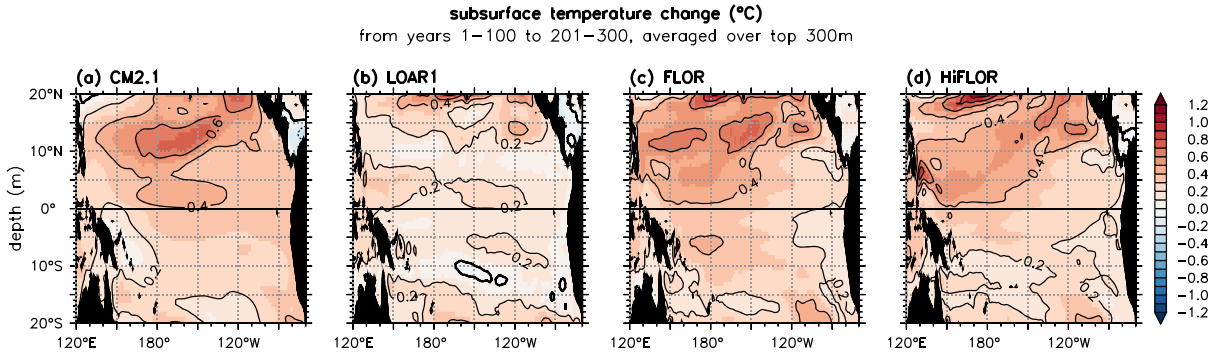

Figure A2. As in Figure A1 but for temperature averaged over the top 300 m of the ocean.

Along a given longitude or latitude, if the average spacing of the source grid is *finer* than that of the target comparison grid, then the denser source cells are *averaged* onto the target grid with appropriate spherical-area weighting. When such averaging is needed in both longitude and latitude, it is done as a two-dimensional spherical area-weighted average.

If the average spacing of the source grid is instead *coarser* than that of the comparison grid, then the coarser source is *linearly interpolated* to the target cell centers. When interpolation is needed in both longitude and latitude, it is done via bilinear spherical interpolation. Any coastal cell that cannot be interpolated in this manner is then filled by spherical area-weighted averaging of any partially overlapping source cells (if they exist; otherwise, the target cell is left undefined, i.e., "missing").

In the vertical direction, the observational and model source grids are typically very different and highly nonuniform—for example, with densely packed levels near the surface and coarse spacing at depth. To compare data sets on such disparate vertical grids, we utilize a refined comparison grid, constructed as the union of the two sets of vertical coordinate centers, and with new cell edges inserted midway between the new cell centers. The source data are then linearly interpolated to the new coordinate centers of the refined vertical comparison grid. Any vertical cell that cannot be interpolated in this manner, for example, near the surface or ocean bottom, is then filled via depth-weighted averaging of any partially overlapping source cells (if they exist; otherwise, the target cell is left undefined).

Once both data sets have been brought onto the comparison grid, they are then both masked with the union of their land and bathymetry masks, resulting in either the same or a smaller data-filled ocean domain. This ensures that any spatial summary statistics will refer to a common ocean domain for each data set.

Finally, the temporal statistic of interest—for example, a climatological average or temporal standard deviation—is computed and displayed as a spatial map, for each data set and for the difference between them. Each map is labeled with statistics to summarize the map, including the spatial mean (μ) and spatial standard deviation (σ) which are both spherical area-weighted. For the difference map, an additional label indicates the spatial root-mean-square difference, that is, $\delta = (\mu^2 + \sigma^2)^{1/2}$.

In summary, the comparison procedure is to (1) mask out land; (2) reduce dimensionality by spatially transforming on the native grid; (3) average/interpolate onto a common grid that is horizontally coarse but vertically fine; (4) apply the union of land masks; (5) compute a temporal statistic to create a spatial map; (6) display the results and their interdata set differences; and then (7) label each map with spatial summary statistics.

Appendix C: Sverdrup Transport

Munk (1950) showed that in steady state and away from the frictional zones near the western boundaries of the ocean, the curl of the wind stress drives a vertically integrated Sverdrup transport within the active upper layer of the ocean, whose meridional component is

$$V_S = \frac{\mathrm{curl}(\boldsymbol{\tau})}{\rho_0 \beta}, \tag{C1}$$

where $\boldsymbol{\tau} = (\tau^x, \tau^y)$ is the vector wind stress on the ocean surface; $\mathrm{curl}(\boldsymbol{\tau}) = \boldsymbol{k} \cdot \boldsymbol{\nabla}_h \times \boldsymbol{\tau}$; $\boldsymbol{\nabla}_h = (\partial_x, \partial_y)$; $\rho_0 \approx 1,035\,\mathrm{kg/m^3}$ is the seawater density; $\beta = \partial_y f = 2\Omega R_a^{-1} \cos\phi$; $f = 2\Omega \sin\phi$ is the Coriolis parameter; $\Omega = 2\pi \mathrm{day}^{-1}$ is the angular frequency of Earth's rotation; $R_a = 6,371\mathrm{km}$ is the Earth's authalic mean radius; and $\phi = y/R_a$ is the latitude in radians.

Consider a Boussinesq ocean in steady state, with the time-mean net surface water flux (e.g., due to rainfall, evaporation, and rivers) assumed to be negligible relative to the time-mean local convergence of ocean mass transport. The vertically integrated transport is then nondivergent, that is

$$\partial_x U_S = -\partial_y V_S, \tag{C2}$$

where $\partial_i \equiv \partial/\partial i$. Integrating (C2) zonally from a given longitude x to the eastern boundary at x_E gives

$$U_S(x) = U_S(x_E) + \int_x^{x_E} \partial_y V_S \mathrm{d}x, \tag{C3}$$

where $U_S(x_E)$ vanishes for a purely meridional eastern boundary but is nonzero for a meridionally sloping boundary like Central America (Kessler et al., 2003). In short, the time-mean zonal transport at a given longitude feeds the total meridional divergence of the Sverdrup transport east of it. Thus, $\partial_y V_S$ helps to relate the structure and intensity of the time-mean zonal currents to the structure of the time-mean surface wind stress.

Appendix D: Ekman Transport and Upwelling

In the pioneering ENSO model of Zebiak and Cane (1987, ZC hereafter), a key breakthrough was to simulate the effects of Ekman upwelling (Yoshida, 1959) on the SST, by embedding a shallow frictional surface mixed layer within the deeper, reduced-gravity active layer of the ocean model. By including the effects of surface Ekman transports and upwelling on mixed layer temperatures, the ZC model simulated more realistic SSTs than did other models of the time, leading to the first successful forecast of ENSO.

Wittenberg (2002, his Appendix C) derived from the ZC model an expression for the mixed layer lateral Ekman transport:

$$\boldsymbol{U}_E = \frac{t_s b}{\rho_0 (\tilde{y}^2 + 1)} (\boldsymbol{\tau} - \tilde{y}\boldsymbol{k} \times \boldsymbol{\tau}), \tag{D1}$$

where $\boldsymbol{U}_E$ (units of m^2/s) is the lateral Ekman transport within the mixed layer; $b = (H - H_m)/H$ is the fraction of the thermocline depth H that lies below the mixed layer depth H_m; t_s is an e-folding time scale for dissipation of vertical shear across the mixed layer base; $\tilde{y} = t_s f$ is a nondimensional latitude; and $\boldsymbol{\tau}$ is the vector surface wind stress.

We define the Ekman component of the upwelling across the base of the mixed layer as

$$w_E = \boldsymbol{\nabla}_h \cdot \boldsymbol{U}_E. \tag{D2}$$

To estimate $\boldsymbol{U}_E$ and w_E from a wind stress data set, we apply (D1) and (D2) on the data set's native grid, with $\boldsymbol{U}_E = \boldsymbol{0}$ at lateral boundaries and $b = 0.6$ and $t_s = 2$ days as in the ZC model.

It is enlightening to examine the components of w_E away from ocean boundaries, with t_s and b constant, on an equatorial beta plane with $f = \beta y$ and $\beta = 4\pi R_a^{-1}(\text{day})^{-1} \approx 1.97 \times 10^{-6}(\text{m day})^{-1}$:

$$w_E = \frac{t_s b}{\rho_0(\tilde{y}^2 + 1)} \left\{ \boldsymbol{\nabla}_h \cdot \boldsymbol{\tau} + \tilde{y}\,\text{curl}(\boldsymbol{\tau}) + \frac{t_s \beta \left[(\tilde{y}^2 - 1)\tau^x - 2\tilde{y}\tau^y \right]}{\tilde{y}^2 + 1} \right\}. \tag{D3}$$

Far from the equator ($\tilde{y} \gg 1$) and for a relatively deep thermocline ($b \to 1$), (D1) and (D3) become the familiar midlatitude expressions for total Ekman transport and upwelling:

$$\boldsymbol{U}_E(\tilde{y} \gg 1, b \to 1) \approx -\frac{\boldsymbol{k} \times \boldsymbol{\tau}}{\rho_0 f}, \tag{D4}$$

$$w_E(\tilde{y} \gg 1, b \to 1) \approx \frac{\text{curl}(\boldsymbol{\tau})}{\rho_0 f}. \tag{D5}$$

Thus, at high latitudes, the Ekman transport is *perpendicular* to the wind stress (to the right of the stress in the northern hemisphere, left in the southern hemisphere); and *cyclonic* wind stress curl induces Ekman *upwelling*.

At the equator, however, (D1) and (D3) become

$$\boldsymbol{U}_E(\tilde{y} = 0) = \frac{t_s b}{\rho_0} \boldsymbol{\tau}, \tag{D6}$$

$$w_E(\tilde{y} = 0) = \frac{b}{\rho_0} \left(t_s \boldsymbol{\nabla}_h \cdot \boldsymbol{\tau} - t_s^2 \beta \tau^x \right), \tag{D7}$$

so that the Ekman transport is purely downwind, and upwelling is driven by both easterly stress and stress divergence.

The final term in (D3) is an interesting consequence of the β effect. Consider a spatially uniform purely meridional wind stress, $\boldsymbol{\tau} = (0, \tau^y)$, such that (D3) becomes

$$w_{\mathrm{E},\tau^y} = \frac{2t_s^2 \beta b}{\rho_0} \frac{-\tilde{y}}{(\tilde{y}^2+1)^2} \tau^y. \tag{D8}$$

Because the coefficient multiplying τ^y has a sign opposite the latitude, an equatorward wind stress induces upwelling. This is because from (D1), equatorward stress drives Ekman transport that turns from crosswind to downwind approaching the equator, giving meridional divergence. The peak upwelling response to τ^y is found by setting $\partial_{\tilde{y}} w_{E,\tau^y} = 0$, which for uniform southerlies occurs at $\tilde{y} = -3^{-1/2}$ or $y = -(t_s \beta 3^{1/2})^{-1} \approx 1.32\,°\mathrm{S}$. This effect of the southerly winds, together with the Ekman suction generated by the cyclonic curl of the wind stress just south of the equator in the east Pacific, helps to explain why the observed east Pacific cold tongue is displaced slightly south of the equator.

Appendix E: Time-Mean Upper-Ocean Heat Budget

Ray et al. (2018a, 2018b) derived a detailed heat budget for the tropical Pacific upper ocean and applied it to FLOR and the SODA.v2.2.4 reanalysis. Here we present a simplified version of that budget, sufficient to highlight the main annual-mean biases and intermodel differences.

Following Kim et al. (2006), the temperature tendency of a given model grid cell in the upper ocean is given by

$$\partial_t T = \frac{\partial_z q}{\rho C_p} - \boldsymbol{\nabla} \cdot (\boldsymbol{u} T) + Q_{\mathrm{subgrid}}, \tag{E1}$$

where T is the cell-averaged temperature, $\partial_z q$ is the vertical convergence of heat flux into the cell due to air-sea exchange and penetrative shortwave radiation, $\rho \approx \rho_0 \approx 1{,}035\ \mathrm{kg/m^3}$ is the seawater density, $C_p \approx 3{,}992\ \mathrm{J \cdot kg^{-1} \cdot K^{-1}}$ is the specific heat capacity of seawater, $\boldsymbol{u} = (u, v, w)$ is the three-dimensional current velocity, $\boldsymbol{\nabla} = (\partial_x, \partial_y, \partial_z)$, and Q_{subgrid} denotes subgridscale mixing and stirring that is parameterized in the ocean model. We have neglected other processes (e.g., sensible heating due to rainfall and rivers) that play a relatively minor role in the overall heat budget of the tropical Pacific upper ocean.

Taking a vertical average (denoted by $[\,]$) from the surface down to the constant depth H_{m}, and then applying a long-term mean (denoted by $\overline{\ }$), yields

$$\overline{[\partial_t T]} = \frac{\overline{Q}_{\mathrm{sfc}} - \overline{Q}_{\mathrm{pen}}}{\rho_0 C_p H_{\mathrm{m}}} - \overline{[\boldsymbol{\nabla} \cdot (\boldsymbol{u} T)]} + \overline{[Q_{\mathrm{subgrid}}]}, \tag{E2}$$

where Q_{sfc} is the net downward heat flux at the surface, and Q_{pen} is the shortwave radiation penetrating through the layer base at H_m.

We next decompose the time series of T and $\boldsymbol{u}$ at each spatial gridpoint as $\psi = \psi_{\mathrm{s}} + \psi_{\mathrm{f}}$, where ψ_{s} is a slow component containing only monthly and longer time scales, and ψ_{f} is a fast component containing the remaining submonthly variability. Expressed as a Fourier decomposition,

$$\psi = \sum_{i=0}^{n/2} \tilde{\psi}_i \cos\left(i\omega_0 t + \theta_i\right) = \psi_{\mathrm{s}} + \psi_{\mathrm{f}}, \tag{E3}$$

$$\psi_{\mathrm{s}} = \sum_{i=0}^{n_s} \tilde{\psi}_i \cos\left(i\omega_0 t + \theta_i\right), \tag{E4}$$

$$\psi_{\mathrm{f}} = \sum_{j=n_{s+1}}^{n/2} \tilde{\psi}_j \cos\left(j\omega_0 t + \theta_j\right), \tag{E5}$$

where $\omega_0 = 2\pi L^{-1}$ is the fundamental frequency, $L = t_{\mathrm{final}} - t_{\mathrm{initial}}$ is the time series length, $n = L/\Delta t$ is the number of time steps, n_s is the number of Fourier harmonics in the slow component, and $\tilde{\psi}_i$ and θ_i are the amplitude and phase of the ith harmonic.

The time-mean temperature flux in (E2) is

$$\overline{\boldsymbol{u}T} = \overline{\boldsymbol{u}_{\mathrm{s}} T_{\mathrm{s}}} + \overline{\boldsymbol{u}_{\mathrm{s}} T_{\mathrm{f}}} + \overline{\boldsymbol{u}_{\mathrm{f}} T_{\mathrm{s}}} + \overline{\boldsymbol{u}_{\mathrm{f}} T_{\mathrm{f}}}. \tag{E6}$$

Substituting the Fourier sums (E4) and (E5) into (E6), the $\boldsymbol{u}_s T_f$ and $\boldsymbol{u}_f T_s$ become sums of products of cosines with unequal harmonic frequencies, $i\omega_0 < j\omega_0$. Each such product vanishes when averaging over the full time series of length L. For example, the average of each term in $\overline{\boldsymbol{u}_f T_s}$ is

$$\begin{aligned}
&\overline{\tilde{u}_j \cos(j\omega_0 t + \theta_j) \times \tilde{T}_i \cos(i\omega_0 t + \theta_i)} \\
&\quad = \frac{\tilde{u}_j \tilde{T}_i}{2} \left\{ \overline{\cos\left[(j+i)\omega_0 t + \theta_j + \theta_i\right]} + \overline{\cos\left[(j-i)\omega_0 t + \theta_j - \theta_i\right]} \right\} \\
&\quad = 0,
\end{aligned} \tag{E7}$$

since the mean of each harmonic cosine vanishes when averaging over L, an integral number of periods. Thus,

$$\overline{\boldsymbol{u}T} = \overline{\boldsymbol{u}_s T_s} + \overline{\boldsymbol{u}_f T_f}, \tag{E8}$$

and so (E2) becomes

$$\frac{\overline{Q}_{sfc}}{\rho_0 C_p H_m} - \overline{\left[\boldsymbol{\nabla} \cdot (\boldsymbol{u}_s T_s)\right]} + \overline{[R]} = 0, \tag{E9}$$

$$\overline{[R]} = \overline{\left[Q_{subgrid}\right]} - \overline{\left[\boldsymbol{\nabla} \cdot (\boldsymbol{u}_f T_f)\right]} - \frac{\overline{Q}_{pen}}{\rho_0 C_p H_m} - \overline{\left[\partial_t T\right]}. \tag{E10}$$

For this study where $H_m = 50$ m, less than 5% of the surface shortwave escapes through the base of the layer, that is, $\overline{Q}_{pen} \ll \overline{Q}_{sfc}$; so for simplicity, we have grouped $\overline{Q}_{pen}$ into $\overline{[R]}$. We also consider epochs longer than 35 years, so that $\overline{\left[\partial_t T\right]}$ is negligible.

Thus, in the time mean, the downward surface heat flux is balanced by advective cooling due to the monthly mean currents and temperature gradients, plus a residual term arising mainly from submonthly eddy advection and parameterized oceanic stirring and mixing.

In ORA-S4, $\overline{[R]}$ also includes any time-mean heating arising from the assimilation increments, which nudge the ocean model toward the observations and thereby compensate for unresolved ocean processes and/or errors in the surface forcings. If the ORA-S4 monthly advection and surface heat fluxes were realistic, then the analysis increments would serve to compensate for imperfections in the assimilating ocean model's parameterizations of subgridscale processes (e.g., mixing), and the full residual term would then be a reasonable target for the residuals diagnosed from FLOR, HiFLOR, and so on. However, biases in ORA-S4's surface heat fluxes and wind stresses, and in ORA-S4's monthly advection as mentioned above, could lead to additional compensating increments in the residual, making it difficult to interpret this term in ORA-S4. Unfortunately, the ORA-S4 product does not provide the reanalysis increments, so we are unable to quantify their role in the ORA-S4 residual.

Although it is straightforward to *compare* heat budget terms among the model simulations, assessing the *realism* of the simulations is far more difficult. The heat budget of the tropical Pacific upper ocean remains poorly constrained by observations, and indeed improving these constraints is a major thrust of the TPOS2020 project's efforts to enhance the tropical Pacific observing system (Cravatte et al., 2016). Systematic estimates of the tropical Pacific ocean heat budget can be derived from ocean reanalyses, namely, ocean models that are forced by surface flux estimates and which assimilate sparse measurements from moorings, floats, ships, and satellites. However, the ocean reanalyses available today produce diverse estimates of the subsurface fields, particularly for the subsurface currents and upwelling which have almost no direct observational constraints (Balmaseda et al., 2015; Ray et al., 2018b; Stammer et al., 2016; Xue et al., 2017). We have already seen that the ORA-S4 reanalysis produces time-mean equatorial zonal currents that differ from mooring data (Figure 13) and time-mean equatorial upwelling that exhibits substantial spatial noise (Figure 14). This lends little confidence to reanalysis heat budgets as reliable targets for ocean simulations. In section 9, we include ORA-S4 in the comparisons only to illustrate the degree of disparity with our simulations. These disparities will need to be resolved through future improvements in both the models and the observational constraints.

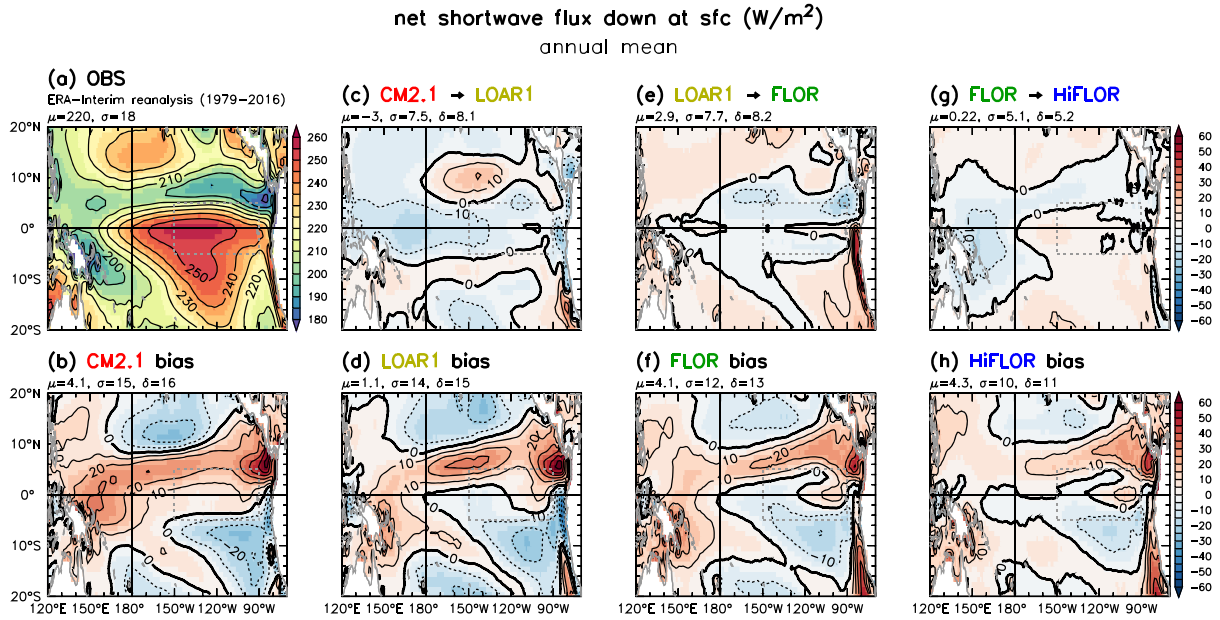

Figure F1. As in Figure 4 but for surface net shortwave heat flux (W/m^2, positive values heat the ocean). Observations (a) are from ERA-Interim, averaged 1979–2016.

Appendix F: Surface Heat Flux Components

F1. Shortwave Heating

Figure F1 shows the annual-mean shortwave heating of the ocean, and Figure F2 shows the total cloud cover. Observations show strong heating under the clear skies of the central equatorial and southern tropical Pacific. There is weaker heating under the deep convective clouds of the main convergence zones and under the stratus cloud decks near South America.

CM2.1 allows too much sunlight to reach the surface, mainly between 6°S and 10°N, with too little contrast between clear and cloudy regions. Exceptions include the northern and southern central Pacific and the South American coastal zone, where there is too much shading from excessive high cloud. LOAR1 improves (weakens) the tropical Pacific shortwave heating due to increased high cloud cover in the equatorial western and central Pacific, which improves the shortwave in the west, but further reduces the clear/cloudy contrast over most of the basin. Averaged over the tropical Pacific, LOAR1's cloud cover exceeds ERA-I by 12%, in contrast to the 3% bias in CM2.1. LOAR1's increased cloud shading is mainly attributable to more high cloud cover.

FLOR generally improves the shortwave pattern, particularly in the central Pacific dry zones due to reduced (improved) high cloud. However, FLOR's reduced high cloud also brings back the basin-mean excessive shortwave bias present in CM2.1. FLOR also increases the excessive shortwave heating along the South American coast, by further reducing the coastal low cloudiness despite FLOR's cooler and more realistic SST near the coast (Figures 1e and 1f); this indicates that FLOR's cooler coastal SSTs cannot be driven by the cloud changes and must instead stem from either stronger subsurface advective cooling (as inferred from Figure 4e) or enhanced evaporation (Figure F3e) associated with FLOR's stronger coastal southerly winds (Figure G1e).

HiFLOR further improves the tropical Pacific shortwave pattern, by reducing high cloud cover throughout the basin and increasing middle and low cloudiness in the deep convective zones.

F2. Evaporative Cooling

Figure F3 shows the annual-mean evaporative cooling of the ocean. ERA-I suggests strong cooling of the tropical Pacific, 130 W/m^2 on average, with stronger cooling beneath the off-equatorial cores of the trade winds. The evaporation weakens over the cooler and less windy eastern equatorial Pacific, especially near the South American coast.

With respect to ERA-I, all four simulations show 4–8 W/m^2 too much evaporative cooling over the basin, with the strongest biases in deep convective regions. The models show even larger biases relative to the other observational estimates (Figure 3). The models' excessive evaporation, which is consistent with their excessive

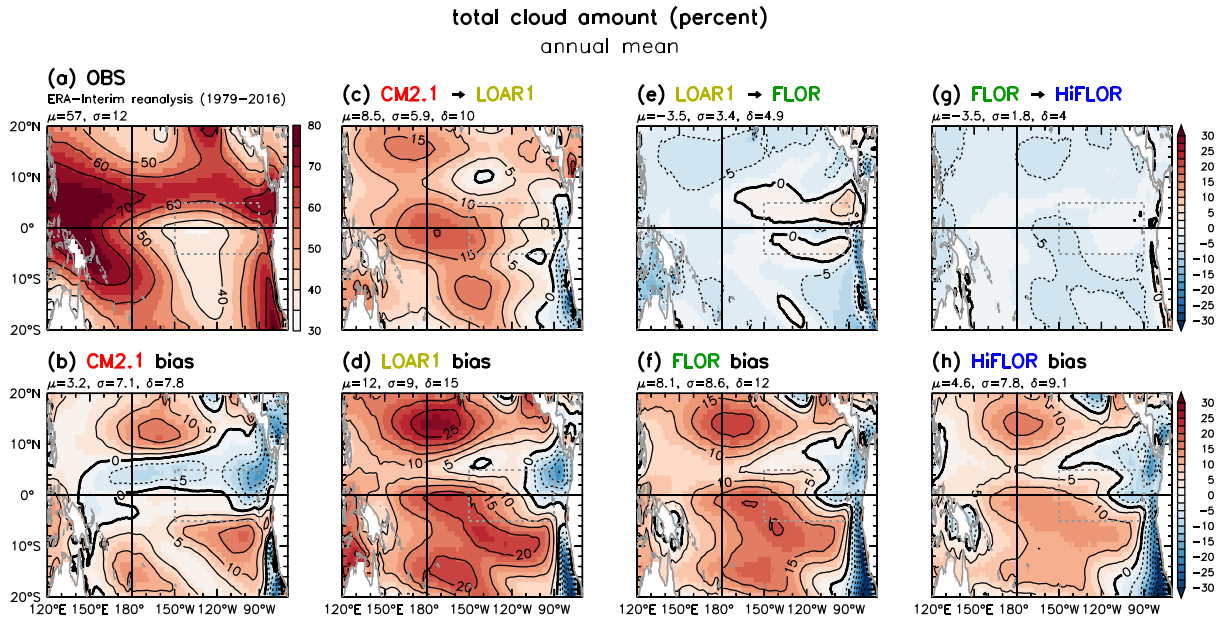

Figure F2. As in Figure F1 but for total cloud cover (%).

rainfall (Figure 2), also partly offsets their excessive insolation near the equator (particularly in the west Pacific and on the southern flank of the ITCZ; Figure F1).

Compared to CM2.1, LOAR1 shows improved (reduced) evaporation, especially near the eastern boundary and near the Maritime continent. FLOR further improves the spatial pattern by enhancing the evaporation near South America and reducing it near Central America but also boosts the spatial-mean evaporation bias relative to LOAR1. HiFLOR shows further improvement relative to FLOR, reducing the excessive evaporation in the deep convective regions.

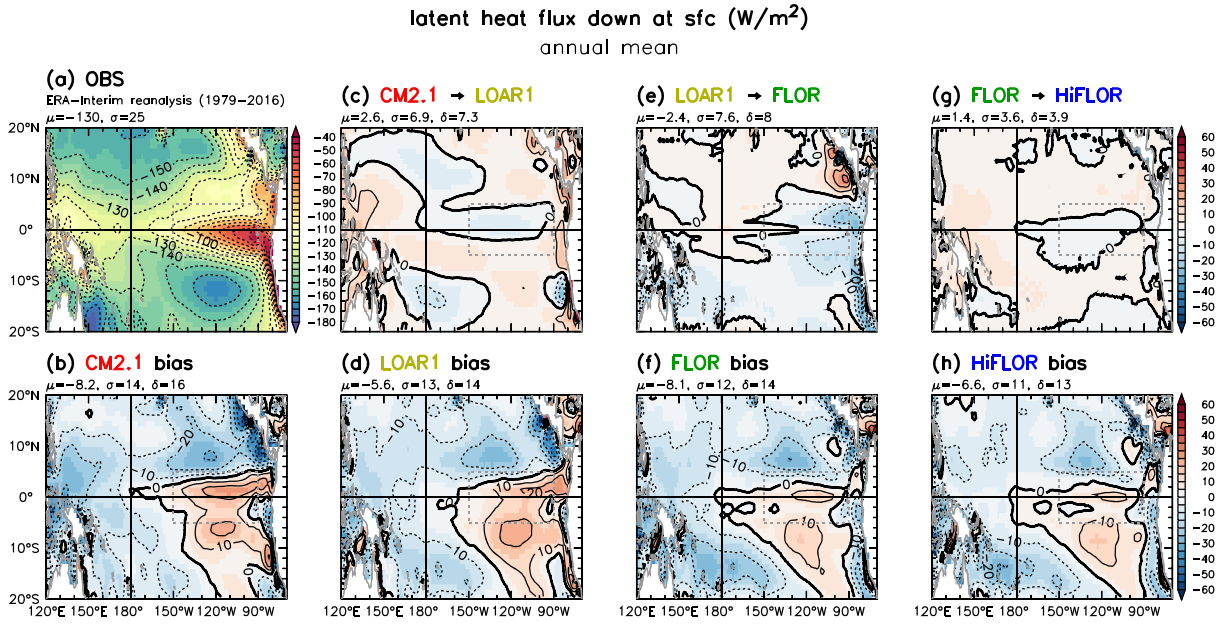

Figure F3. As in Figure F1 but for surface latent heat flux (W/m^2). Positive values heat the ocean.

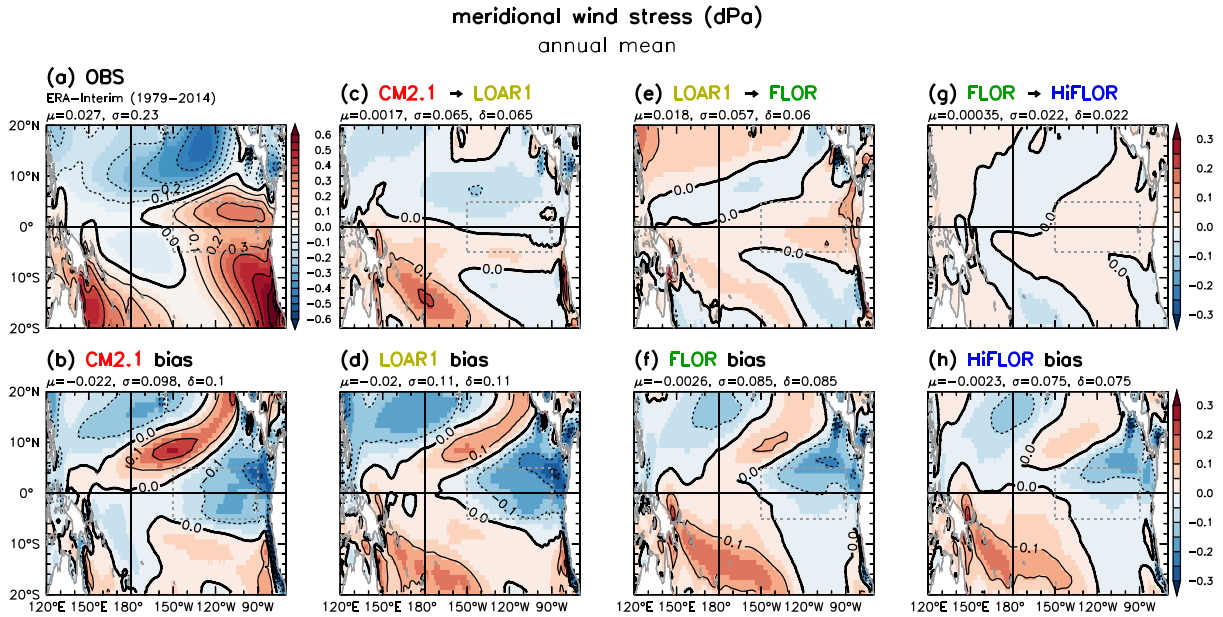

Figure G1. As in Figure 5 but for meridional surface wind stress (dPa). Positive values exert southerly (i.e., northward) stress on the ocean.

F3. Longwave and Sensible Cooling

As suggested by Figure 3, the bias and difference maps for the annual-mean surface longwave and sensible cooling (not shown) are generally much weaker and less spatially variable than those for the shortwave and latent heat fluxes. The sensible cooling biases and intermodel differences are particularly small, owing to the small magnitude of the sensible flux term throughout the tropical Pacific.

The longwave patterns offset part of the shortwave component, with cloudy regions having the weakest longwave cooling of the surface. Relative to ERA-I, all four simulations have 1–5 W/m^2 too much longwave cooling over the tropical Pacific, with insufficient contrast between cloudy and clear zones, again tending to offset the shortwave biases mentioned earlier. Compared to CM2.1, the LOAR1, FLOR, and HiFLOR simulations slightly exacerbate the longwave cooling biases, especially near South America where the latter three models produce too little stratus cloud. HiFLOR has over 5 W/m^2 of excessive longwave cooling over the tropical Pacific, much of which is linked to its basinwide reductions of high cloud relative to FLOR.

Appendix G: Meridional Wind Stress

Figure G1 shows the annual-mean tropical Pacific surface meridional wind stress ($\overline{\tau}^y$). Observations show meridional wind convergence into the ITCZ and SPCZ, with southerly winds crossing the equator in the east Pacific and strong southerlies along the Peru coast. The southeasterly winds near Peru and along 0–2°S in the east Pacific help drive upwelling of cold water from the deep ocean (Appendix D). Along the eastern boundary, there is also a narrow coastal upwelling, associated with the longshore wind stress component that drives an offshore Ekman transport in the upper ocean.

CM2.1 captures these $\overline{\tau}^y$ features, but its southerlies are weaker than observed in the equatorial eastern Pacific, with less intense wind convergence into the ITCZ and weaker divergence over the equatorial cold tongue. CM2.1's peak southerlies are not adjacent to the Peru coast as observed, but farther offshore—greatly reducing the narrow coastal upwelling, and also creating a spuriously strong zone of cyclonic curl and Ekman upwelling farther offshore. LOAR1 has improved (stronger) southerlies along the Peru coast, but otherwise has biases similar to CM2.1 in the east and develops overly strong southerlies in the southwest tropical Pacific. In FLOR and HiFLOR, the $\overline{\tau}^y$ shows more improvement—with stronger southerlies in the eastern equatorial Pacific and along the South American coast, a stronger ITCZ, more wind divergence over the cold tongue, and a weaker southern ITCZ in the east Pacific.

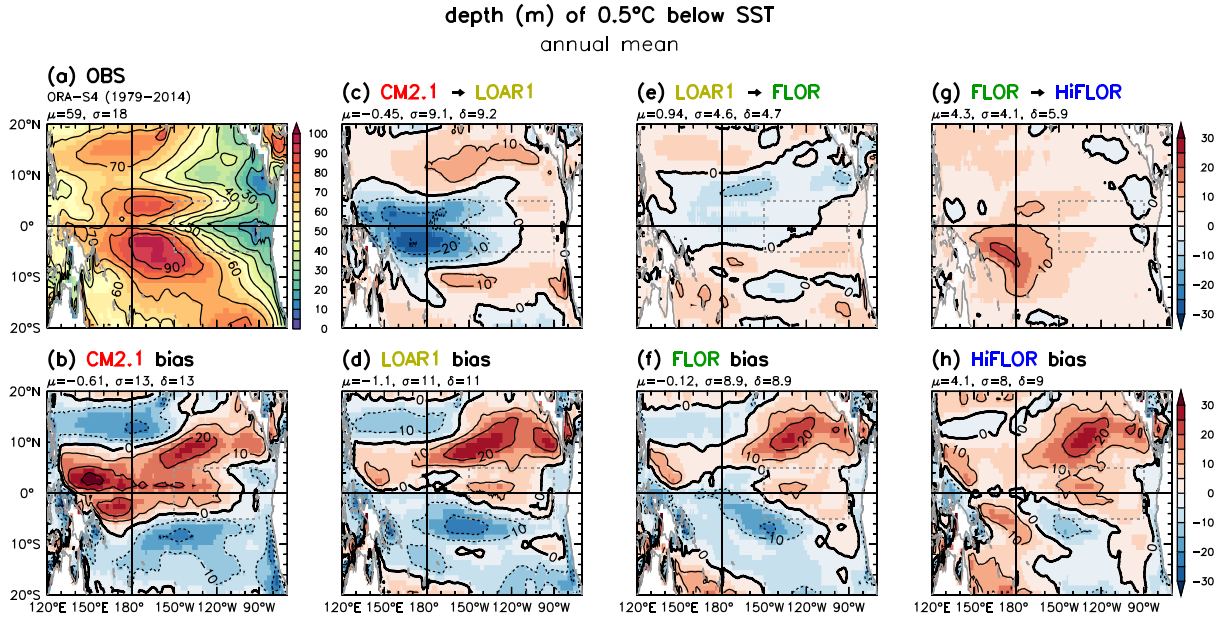

Figure H1. As in Figure 11 but for the depth (m) at which the ocean temperature is 0.5 °C below the surface temperature. This depth is computed each month using the monthly mean temperature field and then time-averaged over the full record.

Appendix H: Isothermal Layer Depth

Figure H1 shows the annual-mean climatology of the monthly ILD, defined here as the depth at which the monthly mean ocean temperature is 0.5 °C cooler than the monthly mean SST.

The ILD is one indicator of the time-mean efficacy of near-surface mixing and stirring. The observed ILD (Figure H1a) shoals where weak winds and strong thermal stratification suppress vertical mixing, as in the shallow-thermocline regions of the eastern equatorial Pacific and near the eastern boundary (Figure 11a). The ILD also shoals where strong haline stratification due to intense local rainfall (Figure 2a) reduces vertical mixing, as in the far west Pacific, near the Philippines, and in the Coral Sea near Australia. The observed ILD peaks in the off-equatorial central Pacific (180–140°W; 8–2°S, 2–6°N), where the thermocline is deep (Figure 11a), there is strong evaporation and wind-induced stirring (Figures F3a and 5a), and clear waters permit deep penetration of solar radiation.

CM2.1's ILD (Figure H1b) is 10–20 m too deep within a broad band about the equator (4°S–10°N, 130°E–100-W) but is 10–20 m too shallow over the rest of the tropical Pacific—including near the South American coast, where a warm SST bias caps a subsurface cold bias. These ILD biases are reduced in LOAR1 (Figures H1c and H1d), especially in the western/central equatorial Pacific where the ILD shoals by more than 20 m relative to CM2.1. This shallower ILD in the equatorial warm pool is likely tied to LOAR1's weaker trade winds, shallower thermocline, and rainfall-induced surface freshening in that region (Figures 2c, 5c, 9c, and H1c), which suppress vertical mixing even in the face of LOAR1's weaker surface solar heating there (Figure F1c).

FLOR further reduces the ILD biases, making its ILD quite realistic, especially along the equator and near South America. HiFLOR further improves the spatial pattern of ILD but also overdeepens the basin-mean ILD by an average of 4 m relative to FLOR and observations (Figures H1g and H1h), with HiFLOR's ILD over 20 m deeper than FLOR's near 170°E, 5°S (where the thermocline is also deeper in HiFLOR). HiFLOR's overly deep ILD is likely due in part to HiFLOR's slightly stronger wind variability and mean wind speeds—suggesting that retuning of the ocean's near-surface mixing may be warranted in the presence of HiFLOR's stronger wind stirring.

Appendix I: Salinity

I1. Sea Surface Salinity

Figure I1 shows the annual-mean sea surface salinity (SSS) over the tropical Pacific, with ORA-S4 as the observational reference. (Comparisons with the World Ocean Atlas 2013 [Zweng et al., 2013] yielded similar results.)

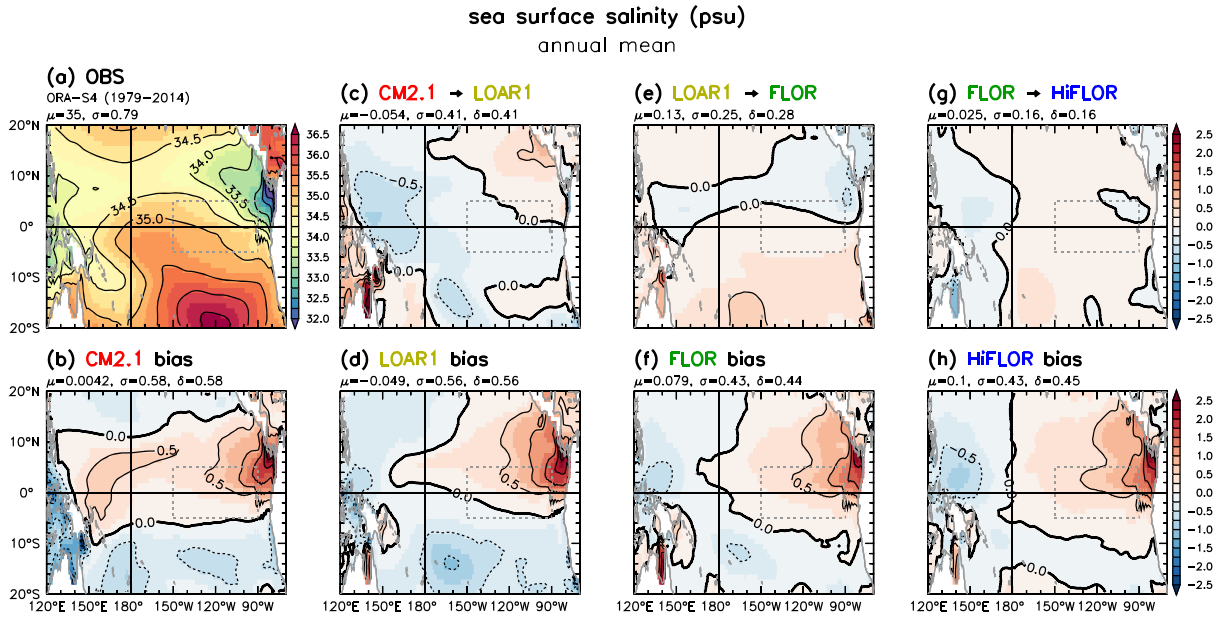

Figure I1. As in Figure 1 but for sea surface salinity (psu). Observations (a) are from ORA-S4, averaged 1979–2014.

The freshest surface waters are in rainy regions (e.g., in the western equatorial Pacific and near the Panama Basin), while the saltiest waters lie in the clear, dry, and windy southeast tropical Pacific near 120°W, 20°S.

CM2.1's SSS biases largely reflect its rainfall biases (Figure 2b), with excessive salinity near the equator and in the Panama Basin (where CM2.1 has dry biases) and overly fresh waters near the Maritime continent and outside 10°S to 12°N (where CM2.1 has too much rainfall). LOAR1's eastward shift of equatorial rainfall relative to CM2.1 (Figure 2c) leads to improved western equatorial Pacific SSS, but otherwise, LOAR1's SSS biases are similar to those in CM2.1. FLOR and HiFLOR show further slight improvements in SSS, particularly for the meridional asymmetry about the equator. All four simulations, however, show excessive SSS near the Panama Basin.

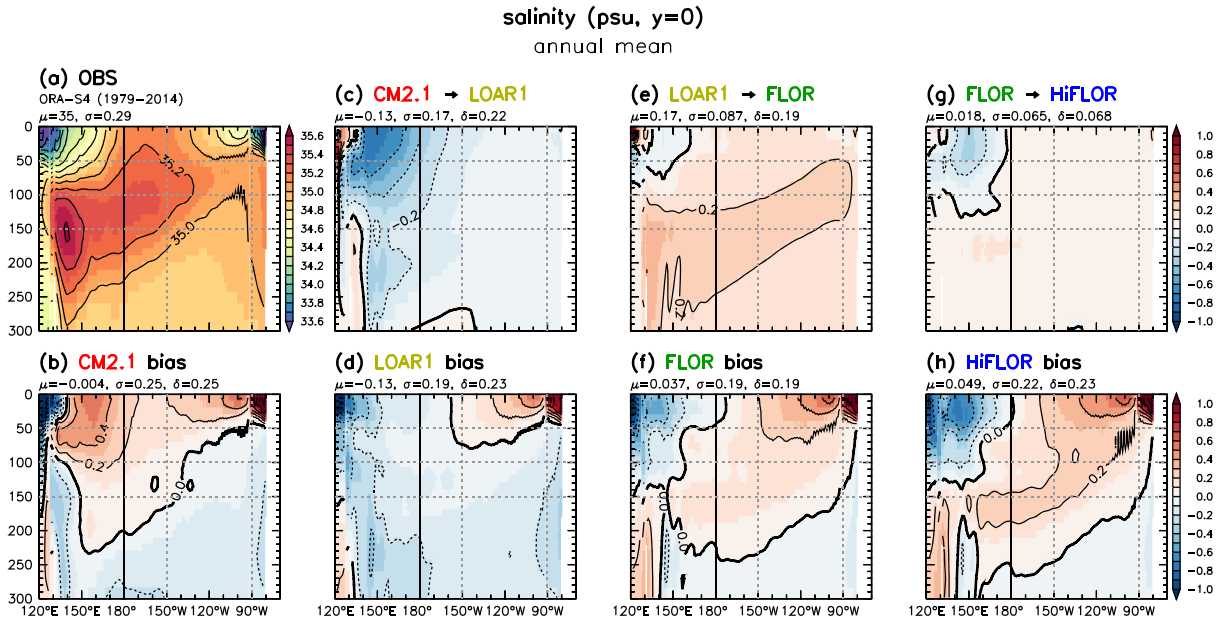

Figure I2. As in Figure I1 but for subsurface salinity (psu) interpolated to the equator. Vertical axis is depth in meters.

I2. Equatorial Salinity

Figure I2 shows the equatorial Pacific annual-mean salinity above 300 m. ORA-S4 shows a salty tongue associated with the EUC, emerging from near the western boundary at 150-m depth. This salty tongue is capped by a surface fresh pool in the west Pacific, creating an intense halocline west of the dateline between 30- and 100-m depth. This halocline is an important player in the density stratification of the warm pool, due to the deep thermocline and weak near-surface $\partial_z \overline{T}$ there. In particular, the strong haloclines that develop during El Niño, and during active phases of the intraseasonal Madden-Julian Oscillation, can trap wind-driven currents within a shallow barrier layer and amplify the resulting advective effects on SST (Maes & Belamari, 2011). East of 120°W where a shallower thermocline generates much stronger $\partial_z \overline{T}$, the halocline is much less critical to the near-surface density stratification.

CM2.1's westward-displaced rainfall in the west Pacific intensifies its equatorial halocline near the Maritime continent, while its poleward-shifted ITCZ weakens its halocline farther east (Figure I2b). CM2.1 also has a deep fresh bias below the thermocline. LOAR1's eastward shift of west Pacific rainfall reduces the salinity of the entire upper ocean along the equator, which reduces the surface salty biases (especially near the dateline), but also slightly worsens the fresh bias below the thermocline.

Compared to LOAR1, FLOR deepens and intensifies the salty tongue associated with the EUC, further reducing the overall salinity biases in FLOR (Figures I2e and I2f). FLOR's stronger salty tongue is apparently due to its saltier source waters south of the equator (Figure I2), since FLOR's EUC is actually weaker than LOAR1's (Figure 13). HiFLOR exhibits slightly stronger equatorial salinity biases than FLOR, with HiFLOR showing a stronger surface fresh bias in the west, and a stronger salty bias within the equatorial thermocline in the central and east Pacific.

Acknowledgments

We thank Baoqiang Xiang, Feiyu Lu, and the two anonymous reviewers for their insightful comments. This study was supported by NOAA GFDL, by NOAA's (Climate Variability and Predictability Program award GC14-250a), and by Princeton University's Cooperative Institute for Climate Science (CICS) under NOAA Cooperative Agreement NA14OAR4320106. The observational and reanalysis data used in this paper are available from the references and links listed in Tables 1 and 2, and the simulation-derived data may be downloaded freely from https://extranet.gfdl.noaa.gov/~atw/yr/2018/wittenberg_etal_james2018.

References

Adler, R. F., Gu, G., & Huffman, G. J. (2012). Estimating climatological bias errors for the Global Precipitation Climatology Project (GPCP). *Journal of Applied Meteorology and Climatology*, *51*, 84–99. https://doi.org/10.1175/JAMC-D-11-052.1

Adler, R. F., Huffman, G. J., Chang, A., Ferraro, R., Xie, P., Janowiak, J., et al. (2003). The version 2 Global Precipitation Climatology Project (GPCP) monthly precipitation analysis (1979-Present). *Journal of Hydrometeorology*, *4*, 1147–1167.

Adler, R. F., Sapiano, M., Huffman, G., Bolvin, D., Gu, G., Wang, J., et al. (2016). *The new version 2.3 of the Global Precipitation Climatology Project (GPCP) monthly analysis product*. MD: Internal Report, Earth System Science Interdisciplinary Center Univ. of Maryland, College Park.

Alexander, M. A., Seo, H., Xie, S.-P., & Scott, J. D. (2012). ENSO's impact on the gap wind regions of the eastern tropical Pacific ocean. *Journal of Climate*, *25*, 3549–3565. https://doi.org/10.1175/JCLI-D-11-00320.1

Anderson, W., Gnanadesikan, A., & Wittenberg, A. (2009). Regional impacts of ocean color on tropical Pacific variability. *Ocean Science*, *5*, 313–327. https://doi.org/10.5194/osd-6-243-2009

Balmaseda, M. A., Hernandez, F., Storto, A., Palmer, M. D., Alves, O., Shi, L., et al. (2015). The Ocean Reanalyses Intercomparison Project (ORA-IP). *Journal of Operational Oceanography*, *8*(S1), s80–s97. https://doi.org/10.1080/1755876X.2015.1022329

Balmaseda, M. A., Mogensen, K., & Weaver, A. T. (2013). Evaluation of the ECMWF ocean reanalysis system ORAS4. *Quarterly Journal of the Royal Meteorological Society*, *139*, 1132–1161. https://doi.org/10.1002/qj.2063

Banzon, V., Smith, T. M., Chin, T. M., Liu, C., & Hankins, W. (2016). A long-term record of blended satellite and in situ sea-surface temperature for climate monitoring, modeling and environmental studies. *Earth System Science Data*, *8*, 165–176. https://doi.org/10.5194/essd-8-165-2016

Barnston, A. G., Tippett, M. K., Ranganathan, M., & L'Heureux, M. L. (2017). Deterministic skill of ENSO predictions from the North American Multimodel Ensemble. *Climate Dynamics*. https://doi.org/10.1007/s00382-017-3603-3, in press.

Behrangi, A., Stephens, G., Adler, R. F., Huffman, G. J., Lambrigtsen, B., & Lebsock, M. (2014). An update on the oceanic precipitation rate and its zonal distribution in light of advanced observations from space. *Journal of Climate*, *27*, 3957–3965. https://doi.org/10.1175/JCLI-D-13-00679.1

Bellenger, H., Guilyardi, E., Leloup, J., Lengaigne, M., & Vialard, J. (2014). ENSO representation in climate models: From CMIP3 to CMIP5. *Climate Dynamics*, *42*, 1999–2018. https://doi.org/10.1007/s00382-013-1783-z

Bonjean, F., & Lagerloef, G. S. E. (2002). Diagnostic model and analysis of the surface currents in the tropical Pacific ocean. *Journal of Physical Oceanography*, *32*, 2938–2954.

Brown, P. J., & Kummerow, C. D. (2014). An assessment of atmospheric water budget components over tropical oceans. *Journal of Climate*, *27*, 2054–2071. https://doi.org/10.1175/JCLI-D-13-00385.1

Burls, N. J., Muir, L., Vincent, E. M., & Fedorov, A. (2017). Extra-tropical origin of equatorial Pacific cold bias in climate models with links to cloud albedo. *Climate Dynamics*, *49*, 2093–2113. https://doi.org/10.1007/s00382-016-3435-6

Cai, W., Santoso, A., Wang, G., Yeh, S.-W., An, S.-I., Cobb, K. M., et al. (2015). ENSO and greenhouse warming. *Nature Climate Change*, *5*, 849–859. https://doi.org/10.1038/nclimate2743

Capotondi, A., Ham, Y.-G., & Wittenberg, A. T. (2015). Climate model biases and El Niño Southern Oscillation (ENSO) simulation. *U.S. CLIVAR Variations*, *13*(1), 21–25.

Capotondi, A., Wittenberg, A., & Masina, S. (2006). Spatial and temporal structure of tropical Pacific interannual variability in 20th century coupled simulations. *Ocean Modelling*, *15*, 274–298. https://doi.org/10.1016/j.ocemod.2006.02.004

Capotondi, A., Wittenberg, A. T., Newman, M., Lorenzo, E. D., Yu, J.-Y., Braconnot, P., et al. (2015). Understanding ENSO diversity. *Bulletin of the American Meteorological Society*, *96*(6), 921–938. https://doi.org/10.1175/BAMS-D-13-00117.1

Carton, J. A., Chepurin, G., Cao, X., & Giese, B. (2000). A simple ocean data assimilation analysis of the global upper ocean 1950–95. Part I: Methodology. *Journal of Physical Oceanography*, *30*, 294–309.

Carton, J. A., Chepurin, G. A., & Chen, L. (2018). SODA3: A new ocean climate reanalysis. *Journal of Climate*, 31, 6967–6983. http://doi.org/10.1175/JCLI-D-18-0149.1

Carton, J. A., Chepurin, G. A., Chen, L., & Grodsky, S. A. (2018) Improved global net surface heat flux. *Journal of Geophysical Research: Oceans*, *123*, 3144–3163. https://doi.org/10.1002/2017JC013137

Chang, Y. S., Zhang, S., Rosati, A., Delworth, T. L., & Stern, W. F. (2013). An assessment of oceanic variability for 1960–2010 from the GFDL ensemble coupled data assimilation. *Climate Dynamics*, *40*, 775–803.

Chen, C.-K., Wang, C., Ma, K.-L., & Wittenberg, A. (2011). Static correlation visualization for large time-varying volume data. In *Proc. IEEE Pacific Visualization Symposium, Hong Kong, China* (pp. 27–34). https://doi.org/10.1109/PACIFICVIS.2011.5742369

Choi, K.-Y., Vecchi, G. A., & Wittenberg, A. T. (2013). ENSO transition, duration, and amplitude asymmetries: Role of the nonlinear wind stress coupling in a conceptual model. *Journal of Climate*, *26*, 9462–9476. https://doi.org/10.1175/JCLI-D-13-00045.1

Choi, K.-Y., Vecchi, G. A., & Wittenberg, A. T. (2015). Nonlinear zonal wind response to ENSO in the CMIP5 models: Roles of the zonal and meridional shift of the ITCZ/SPCZ and the simulated climatological precipitation. *Journal of Climate*, *28*, 8556–8573. https://doi.org/10.1175/JCLI-D-15-0211.1

Christensen, J. H., Kumar, K. K., Aldrian, E., An, S.-I., Cavalcanti, I., De Castro, M., et al. (2014). Climate phenomena and their relevance for future regional climate change. In T. F. Stocker, et al. (Eds.), *Climate change 2013: The physical science basis. Contribution of Working Group I to the Fifth Assessment Report of the Intergovernmental Panel on Climate Change* (Chap. 14, pp. 1217–1308). Cambridge: Cambridge University Press. https://doi.org/10.1017/CBO9781107415324.028

Clement, A. C., Seager, R., Cane, M. A., & Zebiak, S. E. (1996). An ocean dynamical thermostat. *Journal of Climate*, *9*, 2190–2196.

Colella, P., & Woodward, P. R. (1984). The Piecewise Parabolic Method (PPM) for gas-dynamical simulations. *Journal of Computational Physics*, *54*, 174–201. https://doi.org/10.1016/0021-9991(84)90143-8

Collins, M., An, S.-I., Cai, W., Ganachaud, A., Guilyardi, E., Jin, F.-F., et al. (2010). The impact of global warming on the tropical Pacific and El Niño. *Nature Geoscience*, *3*, 391–397. https://doi.org/10.1038/ngeo868

Cravatte, S., Kessler, B., Smith, N., Wijffels, S., Ando, K., Cronin, M., et al. (2016). First report of TPOS 2020 (*Tech. Rep. 215*): UNESCO IOC Global Ocean Observing System (GOOS). Retrieved from http://tpos2020.org/first-report.

Curry, J. A., Bentamy, A., Bourassa, M. A., Bourras, D., Bradley, E. F., Brunke, M., et al. (2004). Seaflux. *Bulletin of the American Meteorological Society*, *85*, 409–424. https://doi.org/10.1175/BAMS-85-3-409

Dee, D. P., Uppala, S. M., Simmons, A. J., Berrisford, P., Poli, P., Kobayashi, S., et al. (2011). The ERA-Interim reanalysis: Configuration and performance of the data assimilation system. *Quarterly Journal of the Royal Meteorological Society*, *137*, 553–597. https://doi.org/10.1002/qj.828

Delworth, T. L., Broccoli, A. J., Rosati, A., Stouffer, R. J., Balaji, V., Beesley, J. A., et al. (2006). GFDL's CM2 global coupled climate models, Part I: Formulation and simulation characteristics. *Journal of Climate*, *19*, 643–674. https://doi.org/10.1175/JCLI3629.1

Delworth, T. L., Rosati, A., Anderson, W., Adcroft, A. J., Balaji, V., Benson, R., et al. (2012). Simulated climate and climate change in the GFDL CM2.5 high-resolution coupled climate model. *Journal of Climate*, *25*, 2755–2781. https://doi.org/10.1175/JCLI-D-11-00316.1

Delworth, T. L., Zeng, F., Rosati, A., Vecchi, G., & Wittenberg, A. T. (2015). A link between the hiatus in global warming and North American drought. *Journal of Climate*, *28*, 3834–3845. https://doi.org/10.1175/JCLI-D-14-00616.1

DiNezio, P. N., Kirtman, B. P., Clement, A. C., Lee, S.-K., Vecchi, G. A., & Wittenberg, A. (2012). Mean climate controls on the simulated response of ENSO to increasing greenhouse gases. *Journal of Climate*, *25*, 7399–7420. https://doi.org/10.1175/JCLI-D-11-00494.1

Dijkstra, H. A., & Neelin, J. D. (1995). Ocean-atmosphere interaction and the tropical climatology. Part II: Why the Pacific cold tongue is in the east. *Journal of Climate*, *8*, 1343–1359.

Emile-Geay, J., Cobb, K. M., Mann, M. E., & Wittenberg, A. T. (2013a). Estimating central equatorial Pacific SST variability over the past millennium. Part I: Methodology and validation. *Journal of Climate*, *26*, 2302–2328. https://doi.org/10.1175/JCLI-D-11-00510.1

Emile-Geay, J., Cobb, K. M., Mann, M. E., & Wittenberg, A. T. (2013b). Estimating central equatorial Pacific SST variability over the past millennium. Part II: Reconstructions and implications. *Journal of Climate*, *26*, 2329–2352. https://doi.org/10.1175/JCLI-D-11-00511.1

Erb, M. P., Broccoli, A. J., Graham, N. T., Clement, A. C., Wittenberg, A. T., & Vecchi, G. A. (2015). Response of the equatorial Pacific seasonal cycle to orbital forcing. *Journal of Climate*, *28*, 9258–9276. https://doi.org/10.1175/JCLI-D-15-0242.1

Ferrari, R., Griffies, S. M., Nurser, A. J. G., & Vallis, G. K. (2010). A boundary-value problem for the parameterized mesoscale eddy transport. *Ocean Modelling*, *32*, 143–156. https://doi.org/10.1016/j.ocemod.2010.01.004

Fox-Kemper, B., Danabasoglu, G., Ferrari, R., Griffies, S. M., Hallberg, R. W., Holland, M. M., et al. (2011). Parameterization of mixed layer eddies. III: Implementation and impact in global ocean climate simulations. *Ocean Modelling*, *39*, 61–78. https://doi.org/10.1016/j.ocemod.2010.09.002

Gainusa-Bogdan, A., Braconnot, P., & Servonnat, J. (2015). Using an ensemble data set of turbulent air-sea fluxes to evaluate the IPSL climate model in tropical regions. *Journal of Geophysical Research: Atmospheres*, *120*, 4483–4505. https://doi.org/10.1002/2014JD022985

Gent, P. R., & McWilliams, J. C. (1990). Isopycnal mixing in ocean circulation models. *Journal of Physical Oceanography*, *20*, 150–155.

Global Atmospheric Model Development Team GFDL (2004). The new GFDL global atmosphere and land model AM2/LM2: Evaluation with prescribed SST simulations. *Journal of Climate*, *17*, 4641–4673. https://doi.org/10.1175/JCLI-3223.1

Gnanadesikan, A., Dixon, K. W., Griffies, S. M., Balaji, V., Barreiro, M., Beesley, J. A., et al. (2006). GFDL's CM2 global coupled climate models, Part II: The baseline ocean simulation. *Journal of Climate*, *19*, 675–697. https://doi.org/10.1175/JCLI3630.1

Graham, F., Wittenberg, A. T., Brown, J. N., Marsland, S. J., & Holbrook, N. J. (2017). Understanding the double peaked El Niño in coupled GCMs. *Climate Dynamics*, *48*, 2045–2063. https://doi.org/10.1007/s00382-016-3189-1

Griffies, S. M. (1998). The Gent-McWilliams skew flux. *Journal of Physical Oceanography*, *28*, 831–841.

Griffies, S. M (2012). Elements of the Modular Ocean Model (MOM): 2012 release (*GFDL Ocean Group Tech. Rep. 7*): NOAA Geophysical Fluid Dynamics Laboratory. Retrieved from http://mom-ocean.org/web/docs/project/MOM5_elements.pdf

Griffies, S. M., Biastoch, A., Böning, C., Bryan, F., Danabasoglu, G., Chassignet, E. P., England, M. H., et al. (2009). Coordinated Ocean-ice Reference Experiments (COREs). *Ocean Modelling*, *26*, 1–46. https://doi.org/10.1016/j.ocemod.2008.08.007

Griffies, S. M., Gnanadesikan, A., Dixon, K. W., Dunne, J. P., Gerdes, R., Harrison, M. J., et al. (2005). Formulation of an ocean model for global climate simulations. *Ocean Science*, *1*, 45–79. https://doi.org/10.5194/os-1-45-200

Griffies, S. M., Gnanadesikan, A., Pacanowski, R. C., Larichev, V. D., Dukowicz, J. K., & Smith, R. D. (1998). Isoneutral diffusion in a z-coordinate ocean model. *Journal of Physical Oceanography*, *28*, 805–830.

Griffies, S. M., & Hallberg, R. W. (2000). Biharmonic friction with a Smagorinsky-like viscosity for use in large-scale eddy-permitting ocean models. *Monthly Weather Review*, *128*, 2935–2946.

Griffies, S. M., Pacanowski, R. C., Schmidt, M., & Balaji, V. (2001). Tracer conservation with an explicit free surface method for z-coordinate ocean models. *Monthly Weather Review*, *129*, 1081–1098. https://doi.org/10.1175/1520-0493(2001)129<1081:TCWAEF>2.0.CO;2

Griffies, S. M., Winton, M., Anderson, W. G., Benson, R., Delworth, T. L., Dufour, C. O., et al. (2015). Impacts on ocean heat from transient mesoscale eddies in a hierarchy of climate models. *Journal of Climate*, *28*, 952–977. https://doi.org/10.1175/JCLI-D-14-00353.1

Gu, D., & Philander, S. G. H. (1997). Interdecadal climate fluctuations that depend on exchanges between the tropics and extratropics. *Science*, *275*, 805–807. https://doi.org/10.1126/science.275.5301.805

Guilyardi, E., Cai, W., Collins, M., Fedorov, A., Jin, F.-F., Kumar, A., et al. (2012). New strategies for evaluating ENSO processes in climate models. *Bulletin of the American Meteorological Society*, *93*, 235–238. https://doi.org/10.1175/BAM S-D-11-00106.1

Guilyardi, E., Wittenberg, A., Balmaseda, M., Cai, W., Collins, M., McPhaden, M. J., et al. (2016). Fourth CLIVAR workshop on the evaluation of ENSO processes in climate models: ENSO in a changing climate. *Bulletin of the American Meteorological Society*, *97*, 817–820. https://doi.org/10.1175/BAMS-D-15-00287.1

Guilyardi, E., Wittenberg, A., Fedorov, A., Collins, M., Wang, C., Capotondi, A., et al. (2009). Understanding El Niño in ocean-atmosphere general circulation models: Progress and challenges. *Bulletin of the American Meteorological Society*, *90*, 325–340. https://doi.org/10.1175/2008BAMS2387.1

Holmes, R. M., & Thomas, L. N. (2015). The modulation of equatorial turbulence by tropical instability waves in a regional ocean model. *Journal of Physical Oceanography*, *45*, 1155–1173. https://doi.org/10.1175/JPO-D-14-0209.1

Im, S.-H., An, S.-I., Lengaigne, M., & Noh, Y. (2012). Seasonality of tropical instability waves and its feedback to the seasonal cycle in the tropical eastern Pacific. *Scientific World Journal*, *2012*, 612048. https://doi.org/10.1100/2012/612048

Jia, L., Yang, X., Vecchi, G. A., Gudgel, R. G., Delworth, T. L., Rosati, A., et al. (2015). Improved seasonal prediction of temperature and precipitation over land in a high-resolution GFDL climate model. *Journal of Climate*, *28*, 2044–2062. https://doi.org/10.1175/JCLI-D-14-00112.1

Jochum, M., & Murtugudde, R. (2006). Temperature advection by tropical instability waves. *Journal of Physical Oceanography*, *36*, 592–605. https://doi.org/10.1175/JPO2870.1

Johnson, G. C., Lyman, J. M., & Loeb, N. G. (2016). Improving estimates of Earth's energy imbalance. *Nature Climate Change*, *6*, 639–640. https://doi.org/10.1038/nclimate3043

Josey, S. A., Yu, L., Gulev, S., Jin, X., Tilinina, N., Barnier, B., & Brodeau, L. (2014). Unexpected impacts of the Tropical Pacific array on reanalysis surface meteorology and heat fluxes. *Geophysical Research Letters*, *41*, 6213–6220. https://doi.org/10.1002/2014GL061302

Kapnick, S. B., Yang, X., Vecchi, G. A., Delworth, T. L., Gudgel, R., Malyshev, S., et al. (2018). Potential for western US seasonal snowpack prediction. *Proceedings of the National Academy of Sciences*, *6*, 1180–1185.

Karamperidou, C., Cane, M. A., Lall, U., & Wittenberg, A. T. (2014). Intrinsic modulation of ENSO predictability viewed through a local Lyapunov lens. *Climate Dynamics*, *42*, 253–270. https://doi.org/10.1007/s00382-013-1759-z

Katjar, J. B., Santoso, A., England, M. H., & Cai, W. (2017). Tropical climate variability: Interactions across the Pacific, Indian, and Atlantic Oceans. *Climate Dynamics*, *48*, 2173–2190. https://doi.org/10.1007/s00382-016-3199-z

Kato, S., Loeb, N. G., Rose, F. G., Doelling, D. R., Rutan, D. A., Caldwell, T. E., et al. (2013). Surface irradiances consistent with CERES-derived top-of-atmosphere shortwave and longwave irradiances. *Journal of Climate*, *26*, 2719–2740. https://doi.org/10.1175/JCLI-D-12-00436.1

Kessler, W. S., Johnson, G. C., & Moore, D. W. (2003). Sverdrup and nonlinear dynamics of the Pacific equatorial currents. *Journal of Physical Oceanography*, *33*, 994–1008. https://doi.org/10.1175/1520-0485(2003)033<0994:SANDOT>2.0.CO;2

Kim, S.-B., Fukumori, I., & Lee, T. (2006). The closure of the ocean mixed layer temperature budget using level-coordinate model fields. *Journal of Atmospheric and Oceanic Technology*, *23*, 840–853. https://doi.org/10.1175/JTECH1883.1

Kirtman, B. P., Min, D., Infanti, J. M., Kinter, J. L. III, Paolino, D. A., Zhang, Q., et al. (2014). The North American Multimodel Ensemble: Phase-1 seasonal-to-interannual prediction; Phase-2 toward developing intraseasonal prediction. *Bulletin of the American Meteorological Society*, *95*, 585–601. https://doi.org/10.1175/BAMS-D-12-00050.1

Krishnamurthy, L., Vecchi, G., Msadek, R., Murakami, H., Wittenberg, A., & Zeng, F. (2016). Impact of strong ENSO on regional tropical cyclone activity in a high-resolution climate model in the North Pacific and North Atlantic. *Journal of Climate*, *29*, 2375–2394. https://doi.org/10.1175/JCLI-D-0468.1

Krishnamurthy, L., Vecchi, G., Msadek, R., Wittenberg, A., Delworth, T., & Zeng, F. (2015). The seasonality of the Great Plains Low-Level Jet and ENSO relationship. *Journal of Climate*, *28*, 4525–4544. https://doi.org/10.1175/JCLI-D-14-00590.1

Kug, J.-S., Choi, J., An, S.-I., Jin, F.-F., & Wittenberg, A. T. (2010). Warm pool and cold tongue El Niño events as simulated by the GFDL CM2.1 coupled GCM. *Journal of Climate*, *23*, 1226–1239. https://doi.org/10.1175/2009JCLI43293.1

L'Ecuyer, T. S., Beaudoing, H. K., Rodell, M., Olson, W., Kato, S., Clayson, C. A., et al. (2015). The observed state of the energy budget in the early twenty-first century. *Journal of Climate*, *28*, 8319–8346. https://doi.org/10.1175/JCLI-D-14-00556.1

Large, W. G., Danabasoglu, G., McWilliams, J. C., Gent, P. R., & Bryan, F. O. (2001). Equatorial circulation of a global ocean climate model with anisotropic horizontal viscosity. *Journal of Physical Oceanography*, *31*, 518–536.

Large, W. G., McWilliams, J. C., & Doney, S. C. (1994). Oceanic vertical mixing: A review and a model with a vertical K-profile boundary layer parameterization. *Reviews of Geophysics*, *32*, 363–403.

Leslie, W. R., Karnauskas, K. B., & Witting, J. H. (2014). The equatorial undercurrent and TAO sampling bias from a decade at SEA. *Journal of Atmospheric and Oceanic Technology*, *31*, 2015–2025. https://doi.org/10.1175/JTECH-D-13-00262.1

Li, G., Du, Y., Xu, H., & Ren, B. (2015). An intermodel approach to identify the source of excessive equatorial Pacific cold tongue in CMIP5 models and uncertainty in observational datasets. *Journal of Climate*, *28*, 7630–7640. https://doi.org/10.1175/JCLI-D-15-0168.1

Li, G., & Xie, S.-P. (2014). Tropical biases in the CMIP5 multimodel ensemble: The excessive equatorial Pacific cold tongue and double ITCZ problems. *Journal of Climate*, *27*, 1765–1780. https://doi.org/10.1175/JCLI-D-13-00337.1

Lin, S.-J. (2004). A "vertically Lagrangian" finite-volume dynamical core for global models. *Monthly Weather Review*, *132*, 2293–2307.

Liu, C., Allan, R. P., Berrisford, P., Mayer, M., Hyder, P., Loeb, N., et al. (2015). Combining satellite observations and reanalysis energy transports to estimate global net surface energy fluxes 1985–2012. *Journal of Geophysical Research: Atmospheres*, *120*, 9374–9389. https://doi.org/10.1002/2015JD023264

Liu, C., Allan, R. P., Mayer, M., Hyder, P., Loeb, N. G., Roberts, C. D., et al. (2017). Evaluation of satellite and reanalysis-based global net surface energy flux and uncertainty estimates. *Journal of Geophysical Research: Atmospheres*, *122*, 6250–6272. https://doi.org/10.1002/2017JD026616

Liu, Z., & Philander, S. G. H. (1995). How different wind stress patterns affect the tropical-subtropical circulations of the upper ocean. *Journal of Physical Oceanography*, *25*, 449–462. https://doi.org/10.1175/1520-0485(1995)025<0449:HDWSPA>2.0.CO;2

Lock, A. P., Brown, A. R., Bush, M. R., Martin, G. M., & Smith, R. N. B. (2000). A new boundary layer mixing scheme. Part I: Scheme description and single-column model tests. *Monthly Weather Review*, *128*, 3187–3199.

Lyman, J. M., Johnson, G. C., & Kessler, W. S. (2007). Distinct 17- and 33-day tropical instability waves in subsurface observations. *Journal of Physical Oceanography*, *37*, 855–872. https://doi.org/10.1175/JPO3023.1

Maes, C., & Belamari, S. (2011). On the impact of salinity barrier layer in the Pacific ocean mean state and ENSO. *Scientific Online Letters on the Atmosphere*, *7*, 97–100. https://doi.org/10.2151/sola.2011-025

Manizza, M., Le Quéré, C., Watson, A. J., & Buitenhuis, E. T. (2005). Bio-optical feedbacks among phytoplankton, upper ocean physics and sea-ice in a global model. *Geophysical Research Letters*, *32*, L05603. https://doi.org/10.1029/2004GL020778

Marchesiello, P., Capet, X., Menkes, C., & Kennan, S. C. (2011). Submesoscale dynamics in tropical instability waves. *Ocean Modelling*, *39*, 31–46. https://doi.org/10.1016/j.ocemod.2011.04.011

McGregor, S., Timmermann, A., England, M. H., Elison Timm, O., & Wittenberg, A. T. (2013). Inferred changes in El Niño-Southern Oscillation variance over the past six centuries. *Climate Past*, *9*, 2269–2284. https://doi.org/10.5194/cp-9-2269-2013

McPhaden, M. J., Busalacchi, A. J., Cheney, R., Donguy, J.-R., Gage, K. S., Halpern, D., et al. (1998). The tropical ocean-global atmosphere observing system: A decade of progress. *Journal of Geophysical Research*, *103*, 14169–14240.

McPhaden, M. J., Timmermann, A., Widlansky, M. J., Balmaseda, M. A., & Stockdale, T. N. (2015). The curious case of the El Niño that never happened: A perspective from 40 years of progress in climate research and forecasting. *Bulletin of the American Meteorological Society*, *96*, 1647–1665. https://doi.org/10.1175/BAMS-D-14-00089.1

Milly, P. C., Malyshev, S. L., Shevliakova, E., Dunne, K. A., Findell, K. L., Gleeson, T., et al. (2014). An enhanced model of land water and energy for global hydrologic and earth-system studies. *Journal of Hydrometeorology*, *15*, 1739–1761. https://doi.org/10.1175/JHM-D-13-0162.1

Moorthi, S., & Suarez, M. J. (1992). Relaxed Arakawa-Schubert: A parameterization of moist convection for general circulation models. *Monthly Weather Review*, *120*, 978–1002.

Morel, A., & Antoine, D. (1994). Heating rate within the upper ocean in relation to its bio-optical state. *Journal of Physical Oceanography*, *24*, 1652–1665.

Moum, J. N., Lien, R.-C., Perlin, A., Nash, J. D., Gregg, M. C., & Wiles, P. J. (2009). Sea surface cooling at the equator by subsurface mixing in tropical instability waves. *Nature Geoscience*, *2*, 761–765. https://doi.org/10.1038/ngeo657

Moum, J. N., Perlin, A., Nash, J. D., & McPhaden, M. J. (2013). Seasonal sea surface cooling in the equatorial Pacific cold tongue controlled by ocean mixing. *Nature*, *500*, 64–67. https://doi.org/10.1038/nature12363

Msadek, R., Delworth, T. L., Rosati, A., Anderson, W., Vecchi, G., Chang, Y.-S., et al. (2014). Predicting a decadal shift in North Atlantic climate variability using the GFDL forecast system. *Journal of Climate*, *27*, 6472–6496. https://doi.org/10.1175/JCLI-D-13-00476.1

Munk, W. H (1950). On the wind-driven ocean circulation. *Journal of Meteorology*, *7*, 79–93. https://doi.org/10.1175/1520-0469(1950)007<0080:OTWDOC>2.0.CO;2

Murakami, H., Vecchi, G. A., Delworth, T. L., Wittenberg, A. T., Underwood, S., Gudgel, R., et al. (2017). Dominant role of subtropical Pacific warming in extreme eastern Pacific hurricane seasons: 2015 and the future. *Journal of Climate*, *30*, 243–264. https://doi.org/10.1175/JCLI-D-16-0424.1

Murakami, H., Vecchi, G. A., & Underwood, S. (2017). Increasing frequency of extremely severe cyclonic storms over the Arabian Sea. *Nature Climate Change*, *7*, 885–889. https://doi.org/10.1038/s41558-017-0008-6

Murakami, H., Vecchi, G. A., Underwood, S., Delworth, T., Wittenberg, A. T., Anderson, W. G., et al. (2015). Simulation and prediction of category 4 and 5 hurricanes in the high-resolution GFDL HiFLOR coupled climate model. *Journal of Climate*, *28*, 9058–9079. https://doi.org/10.1175/JCLI-D-15-0216.1

Murakami, H., Vecchi, G. A., Villarini, G., Delworth, T. L., Gudgel, R., Underwood, S., et al. (2016). Seasonal forecasts of major hurricanes and landfalling tropical cyclones using a high-resolution GFDL coupled climate model. *Journal of Climate*, *29*, 7977–7989. https://doi.org/10.1175/JCLI-D-16-0233.1

Neelin, J. D. (1991). The slow sea surface temperature mode and the fast-wave limit: Analytic theory for tropical interannual oscillations and experiments in a hybrid coupled model. *Journal of the Atmospheric Sciences*, *48*, 584–606.

Ogata, T., Xie, S.-P., Wittenberg, A., & Sun, D.-Z. (2013). Interdecadal amplitude modulation of the El Niño–Southern Oscillation and its impacts on tropical Pacific decadal variability. *Journal of Climate*, *26*, 7280–7297. https://doi.org/10.1175/JCLI-D-12-00415.1

Pacanowski, R. C (1987). Effect of equatorial currents on surface stress. *Journal of Physical Oceanography*, *17*, 833–838. https://doi.org/10.1175/1520-0485(1987)017<0833:EOECOS>2.0.CO;2

Praveen Kumar, B., Vialard, J., Lengaigne, M., Murty, V. S. N., & McPhaden, M. J. (2012). TropFlux: Air-sea fluxes for the global tropical oceans—Description and evaluation. *Climate Dynamics*, *38*, 1521–1543. https://doi.org/10.1007/s00382-011-1115-0

Predybaylo, E., Stenchikov, G., Wittenberg, A. T., & Zeng, F. (2017). Impacts of a Pinatubo-scale volcanic eruption on ENSO. *Journal of Geophysical Research: Atmospheres*, *122*, 925–947. https://doi.org/10.1002/2016JD025796

Putman, W. M., & Lin, S. J. (2007). Finite-volume transport on various cubed-sphere grids. *Journal of Computational Physics*, *227*, 55–78. https://doi.org/10.1016/j.jcp.2007.07.022

Raschke, E., Kinne, S., Rossow, W., Stackhouse, P., & Wild, M. (2016). Comparison of radiative energy flows in observational datasets and climate modeling. *Journal of Applied Meteorology and Climatology*, *55*, 93–117. https://doi.org/10.1175/JAMC-D-14-0281.1

Ray, S., Wittenberg, A. T., Griffies, S. M., & Zeng, F. (2018a). Understanding the equatorial Pacific cold tongue time-mean heat budget, Part I: Diagnostic framework. *Journal of Climate*, *31*, 9965–9985. https://doi.org/10.1175/JCLI-D-18-0152.1

Ray, S., Wittenberg, A. T., Griffies, S. M., & Zeng, F. (2018b). Understanding the equatorial Pacific cold tongue time-mean heat budget, Part II: Evaluation of the GFDL-FLOR coupled GCM. *Journal of Climate*, *31*, 9987–10,011. https://doi.org/10.1175/JCLI-D-18-0152.1

Reynolds, R. W., Rayner, N. A., Smith, T. M., Stokes, D. C., & Wang, W. (2002). An improved in situ and satellite SST analysis for climate. *Journal of Climate*, *15*, 1609–1625.

Richter, I. (2015). Climate model biases in the eastern tropical oceans: Causes, impacts and ways forward. *Wiley Interdisciplinary Reviews: Climate Change*, *6*, 345–358. https://doi.org/10.1002/wcc.338

Richter, I., Xie, S.-P., Wittenberg, A. T., & Masumoto, Y. (2012). Tropical Atlantic biases and their relation to surface wind stress and terrestrial precipitation. *Climate Dynamics*, *38*, 985–1001. https://doi.org/10.1007/s00382-011-1038-9

Rodell, M., Beaudoing, H., L'Ecuyer, T., Olson, W., Famiglietti, J., Houser, P., et al. (2015). The observed state of the water cycle in the early twenty-first century. *Journal of Climate*, *28*, 8289–8318. https://doi.org/10.1175/JCLI-D-14-00555.1

Song, Q., Vecchi, G. A., & Rosati, A. J. (2007). The role of the Indonesian Throughflow in the Indo-Pacific climate variability in the GFDL coupled climate model. *Journal of Climate*, *20*, 2434–2451. https://doi.org/10.1175/JCLI4133.1

Stammer, D., Balmaseda, M., Heimbach, P., Köhl, A., & Weaver, A. (2016). Ocean data assimilation in support of climate applications: Status and perspectives. *Annual Review of Marine Science*, *8*, 491–518. https://doi.org/10.1146/annurev-marine-122414-034113

Stenchikov, G., Delworth, T. L., Ramaswamy, V., Stouffer, R. J., Wittenberg, A., & Zeng, F. (2009). Volcanic signals in oceans. *Journal of Geophysical Research*, *114*, D16104. https://doi.org/10.1029/2008JD011673

Stephens, G. L., & L'Ecuyer, T. (2015). The Earth's energy balance. *Atmospheric Research*, *166*, 195–203. https://doi.org/10.1016/j.atmosres.2015.06.024

Sun, C., Rienecker, M. M., Rosati, A., Harrison, M., Wittenberg, A., Keppenne, C. L., et al. (2007). Comparison and sensitivity of ODASI ocean analyses in the tropical Pacific. *Monthly Weather Review*, *135*, 2242–2264. https://doi.org/10.1175/MWR3405.1

Sweeney, C., Gnanadesikan, A., Griffies, S. M., Harrison, M. J., Rosati, A. J., & Samuels, B. L. (2005). Impacts of shortwave penetration depth on large-scale ocean circulation and heat transport. *Journal of Physical Oceanography*, *35*, 1103–1119. https://doi.org/10.1175/JPO2740.1

Thomas, M. D., & Fedorov, A. V. (2017). The eastern subtropical Pacific origin of the equatorial cold bias in climate models: A Lagrangian perspective. *Journal of Climate*, *30*, 5885–5900. https://doi.org/10.1175/JCLI-D-16-0819.1

Tian, B. (2015). Spread of model climate sensitivity linked to double-Intertropical Convergence Zone bias. *Geophysical Research Letters*, *42*, 4133–4141. https://doi.org/10.1002/2015GL064119

Valdivieso, M., Haines, K., Balmaseda, M., Chang, Y.-S., Drevillon, M., Ferry, N., et al. (2017). An assessment of air-sea heat fluxes from ocean and coupled reanalyses. *Climate Dynamics*, *49*, 1–26. https://doi.org/10.1007/s00382-015-2843-3

van der Wiel, K., Kapnick, S. B., van Oldenborgh, G. J., Whan, K., Philip, S., Vecchi, G. A., et al. (2017). Rapid attribution of the August 2016 flood-inducing extreme precipitation in south Louisiana to climate change. *Hydrology and Earth System Sciences*, *21*, 897–921. https://doi.org/10.5194/hess-21-897-2017

van der Wiel, K., Kapnick, S. B., & Vecchi, G. A. (2017). Shifting patterns of mild weather in response to projected radiative forcing. *Climatic Change*, *140*, 649–658. https://doi.org/10.1007/s10584-016-1885-9

van der Wiel, K., Kapnick, S. B., Vecchi, G. A., Cooke, W. F., Delworth, T. L., Jia, L., et al. (2016). The resolution dependence of contiguous US precipitation extremes in response to CO_2 forcing. *Journal of Climate*, *29*, 7991–8012. https://doi.org/10.1175/JCLI-D-16-0307.1

Vecchi, G. A., Delworth, T., Gudgel, R., Kapnick, S., Rosati, A., Wittenberg, A. T., et al. (2014). On the seasonal forecasting of regional tropical cyclone activity. *Journal of Climate*, *27*, 7994–8016. https://doi.org/10.1175/JCLI-D-14-00158.1

Vecchi, G. A., Msadek, R., Anderson, W., Chang, Y.-S., Delworth, T., Dixon, K., et al. (2013). Multiyear predictions of North Atlantic hurricane frequency: Promise and limitations. *Journal of Climate*, *26*, 5337–5357. https://doi.org/10.1175/JCLI-D-12-00464.1

Vecchi, G. A., Soden, B. J., Wittenberg, A. T., Held, I. M., Leetmaa, A., & Harrison, M. J. (2006). Weakening of tropical Pacific atmospheric circulation due to anthropogenic forcing. *Nature*, *441*, 73–76. https://doi.org/10.1038/nature04744

Vecchi, G. A., & Wittenberg, A. T. (2010). El Niño and our future climate: Where do we stand? *Wiley Interdisciplinary Reviews: Climate Change*, *1*, 260–270. https://doi.org/10.1002/wcc.33

Wang, B., & An, S.-I. (2002). A mechanism for decadal changes of ENSO behavior: Roles of background wind changes. *Climate Dynamics*, *18*, 475–486.

Wang, D., & Müller, P. (2002). Effects of equatorial undercurrent shear on upper-ocean mixing and internal waves. *Journal of Physical Oceanography*, *32*, 1041–1057. https://doi.org/10.1175/1520-0485(2002)032<1041:EOEUSO>2.0.CO;2

Wang, C., Zhang, L., Lee, S.-K., Wu, L., & Mechoso, C. R. (2014). A global perspective on CMIP5 climate model biases. *Nature Climate Change*, *4*, 201–205. https://doi.org/10.1038/nclimate2118

Wild, M. (2017). Towards global estimates of the surface energy budget. *Current Climate Change Reports*, *3*, 87–97. https://doi.org/10.1007/s40641-017-0058-x

Wild, M., Folini, D., Hakuba, M. Z., Schär, C., Seneviratne, S. I., Kato, S., et al. (2015). The energy balance over land and oceans: An assessment based on direct observations and CMIP5 climate models. *Climate Dynamics*, *44*, 3393–3429. https://doi.org/10.1007/s00382-014-2430-z

Willett, C. S., Leben, R. R., & Lavin, M. F. (2006). Eddies and Tropical Instability Waves in the eastern tropical Pacific: A review. *Progress in Oceanography*, *69*, 218–238. https://doi.org/10.1016/j.pocean.2006.03.010

Wittenberg, A. T. (2002). ENSO response to altered climates (Ph.D. thesis), Princeton University. Retrieved from http://www.gfdl.noaa.gov/~atw/research/thesis

Wittenberg, A. T. (2009). Are historical records sufficient to constrain ENSO simulations? *Geophysical Research Letters*, *36*, L14709. https://doi.org/10.1029/2009GL038710

Wittenberg, A. T. (2015). Low-frequency variations of ENSO. *U.S. CLIVAR Variations*, *13*(1), 21–25.

Wittenberg, A. T., Rosati, A., Delworth, T. L., Vecchi, G. A., & Zeng, F. (2014). ENSO modulation: Is it decadally predictable? *Journal of Climate*, *27*, 2667–2681. https://doi.org/10.1175/JCLI-D-13-00577.1

Wittenberg, A. T., Rosati, A., Lau, N.-C., & Ploshay, J. J. (2006). GFDL's CM2 global coupled climate models. Part III: Tropical Pacific climate and ENSO. *Journal of Climate*, *19*, 698–722. https://doi.org/10.1175/JCLI3631.1

Xie, S.-P., Deser, C., Vecchi, G. A., Ma, J., Teng, H., & Wittenberg, A. T. (2010). Global warming pattern formation: Sea surface temperature and rainfall. *Journal of Climate*, *23*, 966–986. https://doi.org/10.1175/2009JCLI3329.1

Xue, Y., Wen, C., Kumar, A., Balmaseda, M., Fujii, Y., Alves, O., et al. (2017). A real-time ocean reanalyses intercomparison project in the context of tropical Pacific observing system and ENSO monitoring. *Climate Dynamics*, *49*, 3647–3672. https://doi.org/10.1007/s00382-017-3535-y

Yang, X., Rosati, A., Zhang, S., Delworth, T. L., Gudgel, R. G., Zhang, R., et al. (2013). A predictable AMO-like pattern in GFDL's fully-coupled ensemble initialization and decadal forecasting system. *Journal of Climate*, *26*, 650–661. https://doi.org/10.1175/JCLI-D-12-00231.1

Yang, X., Vecchi, G. A., Gudgel, R. G., Delworth, T. L., Zhang, S., Rosati, A., et al. (2015). Seasonal predictability of extratropical storm tracks in GFDL's high-resolution climate prediction model. *Journal of Climate*, *28*, 3592–3611. https://doi.org/10.1175/JCLI-D-14-00517.1

Yoshida, K. (1959). A theory of the Cromwell current (the equatorial undercurrent) and of the equatorial upwelling. *Journal of the Oceanographic Society of Japan*, *15*, 159–170. https://doi.org/10.5928/kaiyou1942.15.159

Yu, L., Jin, X., & Weller, R. A. (2008). Multidecade global flux datasets from the Objectively Analyzed Air-sea Fluxes (OAFlux) Project: Latent and sensible heat fluxes, ocean evaporation, and related surface meteorological variables, OAFlux Project Technical Report OA-2008-1, Woods Hole Oceanographic Institution.

Zebiak, S. E., & Cane, M. A. (1987). A model El Niño-Southern Oscillation. *Monthly Weather Review*, *115*, 2262–2278.

Zhang, S., Harrison, M. J., Rosati, A., & Wittenberg, A. (2007). System design and evaluation of coupled ensemble data assimilation for global oceanic climate studies. *Monthly Weather Review*, *135*, 3541–3564. https://doi.org/10.1175/MWR3466.1

Zhang, S., Harrison, M. J., Wittenberg, A. T., Rosati, A., Anderson, J. L., & Balaji, V. (2005). Initialization of an ENSO forecast system using a parallelized ensemble filter. *Monthly Weather Review*, *133*, 3176–3201. https://doi.org/10.1175/MWR3024.1

Zhang, Y., Rossow, W. B., Lacis, A. A., Oinas, V., & Mishchenko, M. I. (2004). Calculation of radiative fluxes from the surface to top of atmosphere based on ISCCP and other global data sets: Refinements of the radiative transfer model and the input data. *Journal of Geophysical Research*, *109*, D19105. https://doi.org/10.1029/2003JD004457

Zhang, W., Vecchi, G. A., Murakami, H., Delworth, T., Wittenberg, A. T., Rosati, A., et al. (2016). Improved simulation of tropical cyclone responses to ENSO in the western north Pacific in the high-resolution GFDL HiFLOR coupled climate model. *Journal of Climate*, *29*, 1391–1415. https://doi.org/10.1175/JCLI-D-15-0475.1

Zhao, M., Golaz, J.-C., Held, I. M., Guo, H., Balaji, V., Benson, R., et al. (2018a). The GFDL global atmosphere and land model AM4.0/LM4.0: 1. Simulation characteristics with prescribed SSTs. *Journal of Advances in Modeling Earth Systems*, *10*, 691–734. https://doi.org/10.1002/2017MS001208

Zhao, M., Golaz, J.-C., Held, I. M., Guo, H., Balaji, V., Benson, R., et al. (2018b). The GFDL global atmosphere and land model AM4.0/LM4.0: 2. Model description, sensitivity studies, and tuning strategies. *Journal of Advances in Modeling Earth Systems*, *10*, 735–769. https://doi.org/10.1002/2017MS001209

Zweng, M. M., Reagan, J. R., Antonov, J. I., Locarnini, R. A., Mishonov, A. V., Boyer, T. P., & Garcia, H. E. (2013). Salinity (Vol. 2). In S. Levitus (Ed.), *World Ocean Atlas 2013* (39 pp.). Washington, DC: NOAA Atlas NESDIS 74, U.S Government Printing Office.